



**PARAMETER INVESTIGATION FOR
SUBSURFACE TOMOGRAPHY WITH
REFRACTION SEISMIC DATA**

Master Thesis in Geophysics

STEFAN JANSEN

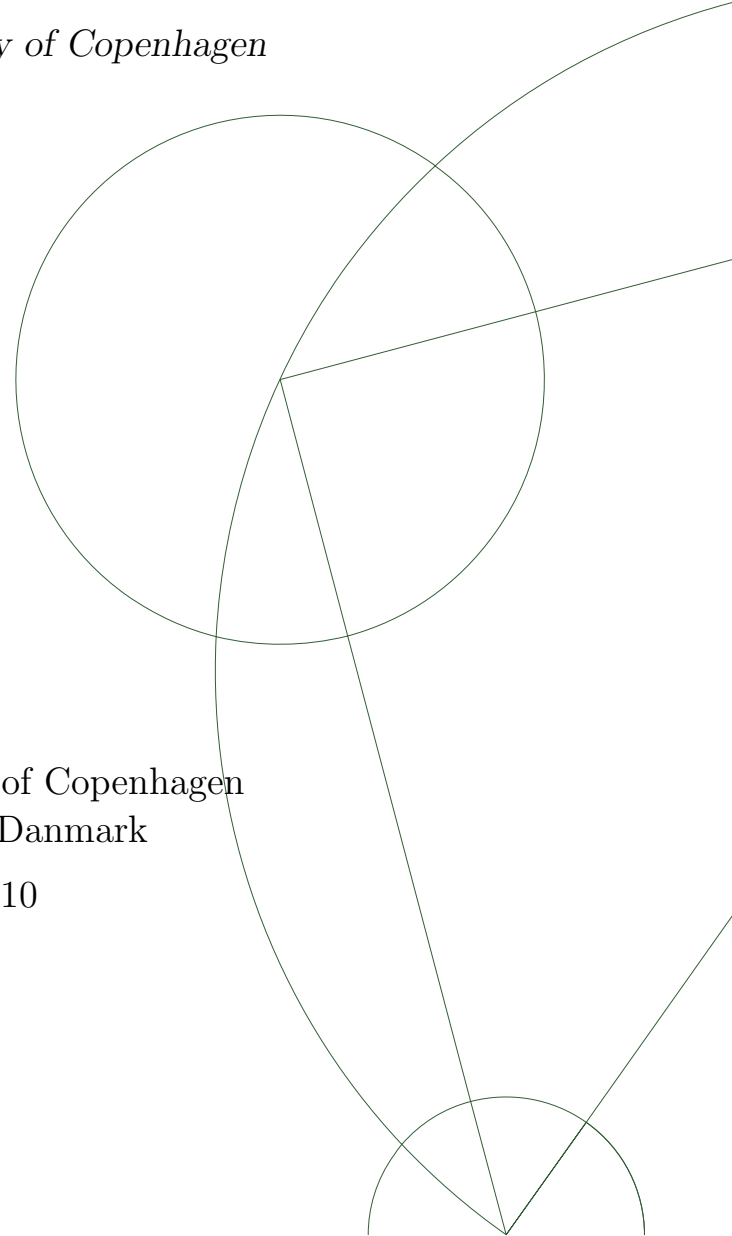
Niels Bohr Institute, University of Copenhagen

Supervisors:

Klaus Mosegaard, University of Copenhagen

Roger Wisén, Rambøll Danmark

2nd November 2010



Master Thesis in Geophysics

Title: Parameter Investigation for Subsurface Tomography with Refraction Seismic Data

Author: Stefan Jansen

CPR no.: 201170

E-mail: stefan.jansen@vip.cybercity.dk

ECTS points: 60

Supervisor: Klaus Mosegaard, University of Copenhagen

External Supervisor: Roger Wisén, Rambøll Danmark

Submitted: 2nd November 2010

Updated: 5th January 2011

Abstract

For planned highway and railway improvements in Norway tomographic images were modelled supplementary to results obtained from a layer based interpretation tool like for example the *Generalized Reciprocal Method* (GRM). In general good agreements between these methods were achieved, but some inconsistencies led to questions whether the tomographic inversions can be improved.

In this master thesis the tomographic inversion tool Rayfract has been examined thoroughly with the aim of determining settings and parameters leading to tomographic images with increased velocity contrast.

With the help of synthetic models containing various kinds of anomalies the sensitivity of the tool has been investigated. A thorough parameter investigation on one of these models led to the determination of six combinations of settings and parameters for obtaining an improved absolute RMS-error and model resemblance. Verification of these combinations with a model resembling one of the profiles from Norway showed unexpected responses. Finally these findings were applied to field data.

Over all this work shows that two parameters, Smoothing and wavepath width, are decisive for the quality of all conducted inversions. These parameters are both directly or indirectly linked to smoothing of the result. Even if a fixed recipe for the choice of parameters can not be given, as they are dependent on the topography and subsurface condition of each individual profile, this thesis clearly defines the parameters in focus and how to perform a quick and reliable parameter test for each new situation.

Contents

Contents	iii
1 Introduction	1
2 Refraction Seismology	5
2.1 CMP-Refraction Seismology	10
3 The Generalized Reciprocal Method (GRM)	13
4 Rayfract[®] Seismic Refraction & Borehole Tomography	17
4.1 Delta-t-V Inversion	18
4.1.1 Traveltime Field Computation	20
4.2 Smooth Inversion	23
4.3 WET Wavepath Eikonal Traveltime tomography	24
4.3.1 Fresnel volume - Fat Rays	27
5 Investigations	29
5.1 Sensitivity Investigation	29
5.1.1 Synthetic Models	32
5.1.2 Results of Sensitivity Investigation	33
5.2 Parameter Investigation	35
5.2.1 Smooth Inversion Settings	37
5.2.2 Delta-t-V Inversion Settings and Parameters	38
5.2.3 WET Tomography Inversion Settings and Parameters .	42
6 Results of the Parameter Investigations	45
6.1 Smooth Inversion	45
6.1.1 Smooth Inversion Settings	45
6.1.2 Delta-t-V Inversion	48
6.2 WET Tomo	50
6.2.1 General WET Tomo Settings	50

6.2.2	Interactive WET Tomo Parameters	51
6.3	Combined Settings	54
7	Case Ørbekk	59
8	Ørbekk Field Data Processing	65
8.1	Default Settings and Parameters	65
8.2	Combinations of Best Settings and Parameters	68
9	Sources of Uncertainties	71
10	Conclusion and Prospects	73
A	Eikonal solver by Vidale	77
B	Refractor-imaging principle	79
C	Sensitivity Investigation	81
C.1	Synthetic Models	81
C.1.1	Synthetic models with faults	92
D	Results of the Parameter Investigation	99
D.1	Tomogram of the Reference Model	99
D.2	Smooth Inversion	100
D.2.1	Smooth Inversion Settings	100
D.2.2	Delta-t-V Inversion Settings	101
D.2.3	Parameters for Interactive Delta-t-V Inversion	103
D.3	WET Tomography	104
D.3.1	WET Tomography Settings	104
D.3.2	Settings for Forward modelling	106
D.3.3	Interactive WET Tomomography Parameters	107
D.4	Combinations of Settings and Parameters	109
D.4.1	Tomograms after 50 iterations	111
D.4.2	Tomograms after 250 iterations	112
E	Case Ørbekk - Inversion Results	113
F	Additional Analysis	117
G	Further Improvements	119
	Bibliography	121

Chapter 1

Introduction

Seismic tomography, also known as Refraction tomography, has in recent years gained increasing interest in near-surface processing. This method is able to overcome the constraints faced by conventional methods (Sheehan et al., 2005). Therefore it has become an interesting method for geotechnical applications where the near subsurface is explored.

As many other geophysical methods, the refraction seismology has the aim of surveying the structure and physical properties of the subsurface from measurements taken on the surface. The refraction seismology is capable of determining the velocity of the layer beneath the weathering layer (top layer), called the refractor; this can not be achieved with reflection seismology. Refraction seismology is used for determining wave-velocities and layer thicknesses of the weathering layers, and for surveys for mapping larger areas and velocity determination of unknown areas as well as various other applications (Gebrande and Miller, 1985). Data processing is handled by the use of CMP (Common Mid-Point) refraction seismology, which simplifies the arrangement of sources and receivers as in reflection seismology.

Conventional processing tools/interpretation methods, as for example *delay-time* and *Plus-Minus-method* or GRM (*Generalized Reciprocal Method*) analysis, make simplifying assumptions about the velocity structure that conflict with frequently observed near-surface attributes such as heterogeneity, lateral discontinuities, and gradients (Sheehan et al., 2005). Refraction tomography is not subject to these constraints and is therefore able to resolve velocity gradients and lateral velocity changes and can be applied in geological conditions

where conventional refraction techniques fail, such as areas of compaction, karst, and fault zones (Zhang and Toksoz, 1998).

Tomographic imaging has been conducted by Rambøll Danmark with the tomographic code Rayfract[®] by Intelligent Resources Inc., which inversions are based on *Wavepath Eikonal Traveltime* (WET) (Schuster and Quintus-Bosz, 1993), and directly compared to the layer based interpretation method *Generalized Reciprocal Method* (GRM). As the results of these different methods did not correlate perfectly the questions

- Has the program been used correctly with respect to settings and chosen parameters?
- Is it possible to improve the quality/velocity contrast of the tomograms?

have been raised.

In this thesis the functions of the program Rayfract[®], which creates 2D tomograms from refraction seismic data, are investigated in order to find the optimal settings and parameters for obtaining tomographic images with the best possible velocity contrast.

Before the parameter investigation the code's ability to recognize different objects in the subsurface is examined. Synthetic models with vertical anticlines and synclines (holes in the refractor) of different widths, anomalies

- shaped as squares
- with the shape of rectangulars
- in different dimensions
- with different velocities
- in various locations

as well as faults

- with different sloping angles

- with different widths

are created for computing first arrival traveltimes. Also part of this investigation is the inspection of the difference between high and sparse shot and receiver coverage. From these models the best suited model for the subsequent parameter investigations is chosen as the reference model with default code settings.

The parameter investigation is carried out by changing only one parameter at a time in order to see the influence of each parameter and setting individually. As a comparison criterion the resulting absolute RMS-error and normalized RMS-error, computed as the RMS-error divided by maximum pick time of all traces modelled, are good choices.

After having studied the influence of all relevant settings and parameters, the ones giving the best results with respect to RMS-error are collected in different combinations. As a result of this study it is expected to find a combination, which yields a tomographic inversion with a better velocity contrast compared to the default settings and parameters.

The thus determined settings and parameters are then applied to traveltimes, which are computed from a model resembling an extract of a real profile; this includes the station and shot coordinates from the original measurements.

Finally with the combination, which yields the best result, a tomographic model from real measurement data is created. As the aim of this work is to improve the contrast of earlier obtained images the same field data are used. This way the direct comparison of the results reveals the dimension of the improvement.

In chapter 2 the theory of refraction and CMP-Refraction seismology is discussed. Then a short description of the layer based interpolation tool *Generalized Reciprocal Method* (GRM) in chapter 3 is followed by an elaboration of the inversion processes the Rayfract code is built on (chapter 4). The actual parameter investigation follows the description of the examined sensitivity models and their outcome in chapter 5. After the investigation with synthetic data is completed the gained knowledge is applied to real survey data as described in chapter 8. The report rounds up with the discussion of possible uncertainties in chapter 9 and the conclusions and prospects in chapter 10.

In the Appendix all synthetic models and their respective tomograms as well as all parameter investigation results and the combined solutions can be found.

For reading this report it is necessary to read it in parallel with the Appendix. A large number of investigations generated a tremendous amount of data and images and presenting them in the Appendix provides a more fluent read. However, tomographic images with the desired positive effect are integrated in the text and discussed there.

Chapter 2

Refraction Seismology

In order to determine the velocity structure of the subsurface the refraction seismology is a very important tool. This chapter provides a short review of the theory behind refraction seismology.

A seismic ray that strikes the boundary of two layers, which mark the change in seismic velocity, is partitioned into a reflected and refracted ray. The angles the reflected and refracted waves form with the vertical plane are described by the *law of reflection* and *law of refraction*. The latter one is also known as *Snell's law* (equation 2.0.1) with angles and velocities as illustrated in figure 2.1.

$$\frac{\sin(i)}{v_1} = \frac{\sin(\beta)}{v_2} = s \quad (2.0.1)$$

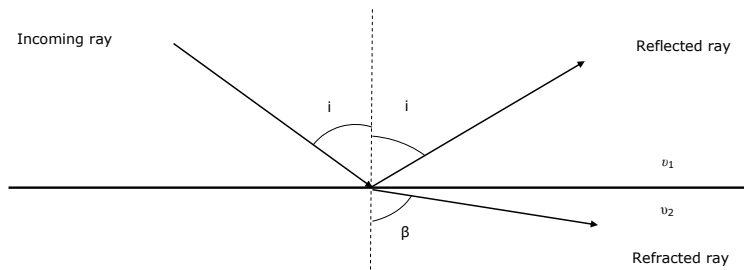


Figure 2.1: An incoming ray strikes the boundary of two media with different velocities ($v_2 > v_1$) and is partitioned into a reflected and refracted ray.

The quantity s is the *horizontal slowness*, also called the *raypath parameter*, and has the same value for incident, reflected and refracted waves.

The incoming and reflected ray experience the same layer properties, hence their angles to the vertical plane are equal. For velocity v_2 greater than v_1 the angle β becomes larger than angle i and vice versa. When β assumes the angle 90 degrees the refracted ray travels horizontally in the lower medium, parallel to the interface between the two media. This wave is also referred to as the headwave and it has the unique property that it continually transmits energy back into the upper layer as it travels along the interface (Lay and Wallace, 1995). The angle of incidence that causes this phenomenon is called the critical angle, i_c and is defined as:

$$i_c = \arcsin(v_1/v_2). \quad (2.0.2)$$

For the case where the angle i is greater than i_c it is impossible to satisfy Snell's law as $\sin(\beta)$ cannot reach unity (Telford et al., 2004). No refracted ray exist and all energy is reflected back into the upper layer (total reflection). If v_2 is smaller than v_1 no critical angle exists and the refracted ray is deflected toward vertical.

Traveltimes:

For the determination of the velocities of the subsurface layers the travel-time is a very important parameter. The travelttime as a function of distance provides a direct measure of velocity at depth. As mentioned above, the reflected and refracted waves are the resulting travel paths when the lower velocity, v_2 , is greater than the upper velocity, v_1 . Furthermore, there is the direct arrival, which travels in a straight line between the source (i.e. an explosion) and receiver (i.e. a geophone or hydrophone). In figure 2.2 the explosion is marked as an asterisk, the receiver as ∇ and the distance the direct wave travels between them as Δ .

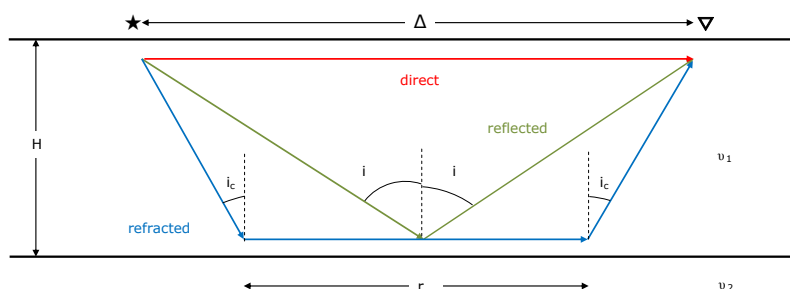


Figure 2.2: Three principle rays in a layer over a refractor. A headwave is equivalent to the distance marked 'r'.

For the paths shown in figure 2.2 the following three traveltimes for sources at the surface and the layer thickness H are found:

- Travelttime for direct arrival:

$$t_{dir} = \Delta/v_1 \quad (2.0.3)$$

- Travelttime for the reflected arrival:

$$t_{refl} = 2H/(\cos(i)v_1) \quad (2.0.4)$$

- Travelttime for the refracted arrival:

$$t_{refr} = r/v_2 + 2H/(\cos(i_c)v_1) \quad (2.0.5)$$

Here the parameter r is the distance the refracted wave travels in the refractor parallel to the intersection. As seen in figure 2.2, the refracted wave has travelled a certain horizontal distance in the upper medium before it is refracted and turns into a headwave. This implies that at a certain distance from the source there cannot be any refracted ray. This distance is also referred to as the *critical distance*, Δ_c , and is defined as:

$$\Delta_c = 2H \tan(i_c). \quad (2.0.6)$$

Substituting the expression for i_c in equation (2.0.2) and applying some basic trigonometric rules yields the following relation for the critical distance:

$$\Delta_c = 2H \tan(\arcsin(v_1/v_2)) = \frac{2H}{\sqrt{(v_2/v_1)^2 - 1}}. \quad (2.0.7)$$

For receivers with increasing distance from the source the term r/v_2 in equation (2.0.5) becomes more dominant; the wavefront travels along the surface with the apparent velocity v_2 . With $r = \Delta - 2H \tan(i_c)$ and $\sin(i_c) = v_1/v_2$ equation (2.0.5) becomes

$$t_{refr} = \frac{2H}{\cos(i_c)} \frac{1}{v_1} + \frac{1}{v_2} \left(\Delta - \frac{2Hv_1}{\cos(i_c)v_2} \right) = \frac{2H}{\cos(i_c)} \left(\frac{1}{v_1} + \frac{v_1}{v_2^2} \right) + \frac{\Delta}{v_2} \quad (2.0.8)$$

This is a very useful equation because it separates the travelpath into a horizontal and a vertical term (Lay and Wallace, 1995).

Figure 2.3 shows the traveltime curves for the three primary waves. At short distances only the direct (red) and reflected (green) arrivals exist. The reflected-arrival traveltime is described by a hyperbola. The intercept time τ^1 at $\Delta=0$ has a traveltime of $2H/v_1$. At large distance the reflection traveltime becomes asymptotic to the direct arrival. The headwave appears as a reflection at the critical distance, Δ_c (Lay and Wallace, 1995).

¹Intercept time is the traveltime at zero off-set. The time distance curve of the refracted line is back-projected to the zero off-set point, where the intercept-time is found. It is not a physical meaningful value as no refraction traveltimes exist for offsets less than Δ_c , but it is a very useful method for computing the layer thickness. See Telford et al. (2004) for details.

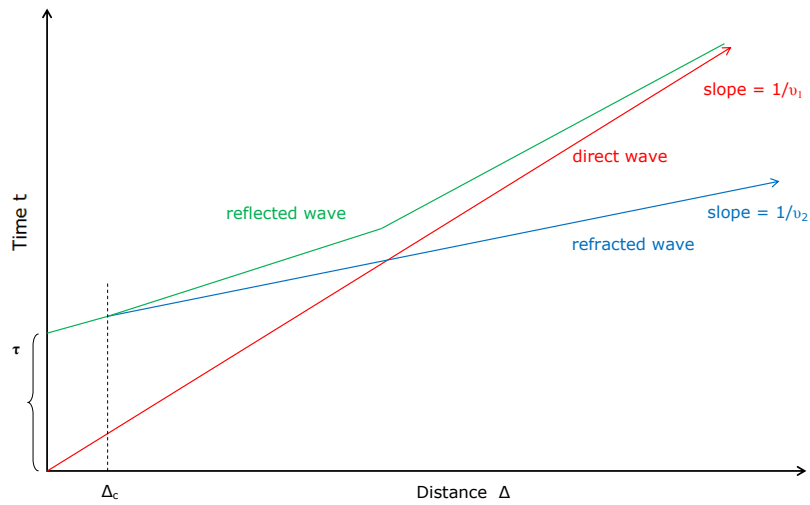


Figure 2.3: Time-distance curve of the direct, reflected and refracted arrivals.

Figure 2.4 gives an example of a seismic profile recording of an area in the USA. Traveltimes for the direct arrivals, reflected arrivals and refracted arrivals are clearly visible and indicated in conformance with the lines in figure 2.3.

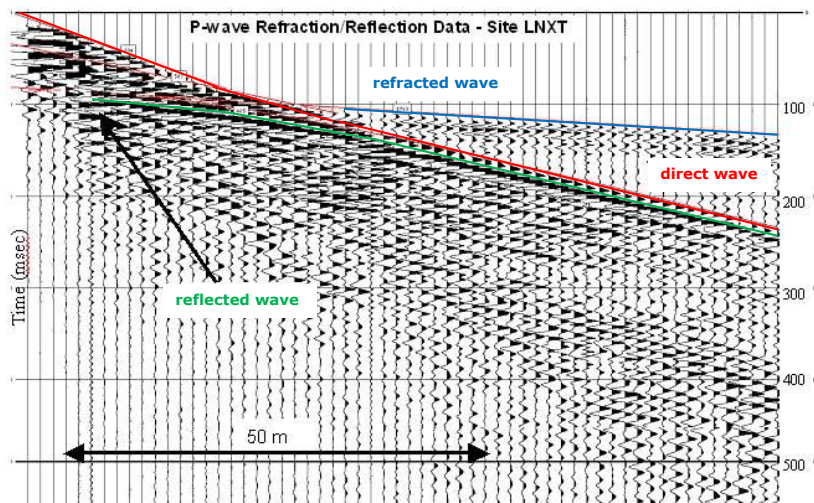


Figure 2.4: Seismic profile recording from Lenox, Tennessee, USA illustrating the three primary arrivals at the receivers. Source is a 4 kg sledgehammer, receiver-spacing 1.5 m. Coloured lines correspond to lines in figure 2.3. The traveltimes for the refracted wave appear earlier than can be seen in this seismogram. Source: <http://pubs.usgs.gov/of/2003/ofr-03-218/ofr-03-218.html>

2.1 CMP-Refraction Seismology

The common-midpoint-technique (CMP-technique) is originally known from reflection-seismology where it contributed a lot to its progress. Today it is almost exclusively used.

A mid-point is defined as the mid-point between source and receiver position and traces are gathered with a common midpoint position. By this all reflections, measured at different offsets, are gathered in the same CMPs, which contain information of the same subsurface points below the midpoint positions. One important reason for this technique is its usage for the subsequent stacking where the generally poor signal-to-noise ratio is improved. For details about the CMP technique with reflection-seismology refer to Telford et al. (2004) or Drijkoningen and Verschuur (2003).

Gebrande (1986) assumes that the advantages of this technique within reflection-seismology can lead to the same simplifications in refraction seismology. He derives formulas for the N-layer as well as 2-layer problem. In this thesis only the 2-layer-case shall be treated because this case often occurs in reality and forms the basis of the several layers problem.

Figure 2.5 shows a CMP in refraction seismology, where it is defined as the midpoint X between the two shotpoints F (forward shot with receiver R) and R (reverse shot with receiver F).

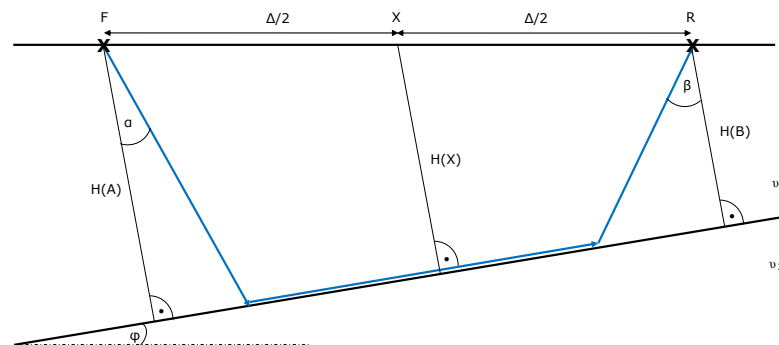


Figure 2.5: Principle of the CMP Refraction Traveltimes.

For two layers the CMP-model is described by the layer thickness, $H(X)$, measured perpendicular to the layer boundary beneath the CMP X , the dipping angle φ and the layer velocities v_1 and v_2 .

Gebrande derives the following equation for the traveltime:

$$t(X, \Delta) = \frac{2H(X)}{v_1} \sqrt{1 - \left(\frac{v_1}{v_2}\right)^2} + \frac{\Delta \cos(\varphi)}{v_2}. \quad (2.1.1)$$

With this equation the CMP-traveltime can be seen as a function of two independent variables, the CMP-coordinates X and the offsets Δ . Partial differentiation with Δ for constant X delivers the *reciproke CMP-apparent velocity*:

$$\left(\frac{\partial t(X, \Delta)}{\partial \Delta}\right)_X = \frac{\cos(\varphi)}{v_2} = \frac{1}{V_{CMP}}. \quad (2.1.2)$$

Partial differentiation with X for constant offset Δ leads to the *dipping function*:

$$\left(\frac{\partial t(X, \Delta)}{\partial X}\right)_\Delta = -\frac{2 \sin(\varphi)}{v_1} \sqrt{1 - \left(\frac{v_1}{v_2}\right)^2}. \quad (2.1.3)$$

When the velocity of the uppermost layer, v_1 , is known, then the dipping angle, φ , and refractor velocity, v_2 , or critical angle, $i_c = \arcsin(v_1/v_2)$, respectively, and with the CMP-intercept time, τ , which is the first term of equation (2.1.1), the local layer-thickness, $H(X)$, can be determined.

$$H(X) = \frac{\tau v_1}{2} \sqrt{1 - \left(\frac{v_1}{v_2}\right)^2}^{-1} = \frac{\tau v_1}{2 \cos(i_c)}. \quad (2.1.4)$$

In principle this technique is similar to a forward and reverse-shot analysis with the advantage that extrapolations to the shotpoints are not necessary, but local, at CMP valid layer thicknesses, are found. The refractor is obtained as an envelope of circles with radius $H(X)$ around the CMPs at the surface (Gebrande, 1986).

Chapter 3

The Generalized Reciprocal Method (GRM)

Earlier made tomographic inversions have been compared to interpretations of the refraction seismic processing algorithm *Generalized Reciprocal Method* (GRM).

The advantage of the GRM inversion algorithms, compared to conventional methods, is their emphasis of the lateral resolution of individual layers (Palmer, 2009). Two inversion algorithms are employed: the *refractor velocity analysis function* t_V and the *time model algorithm* t_X . From the refractor velocity analysis function (equation (3.0.1)) the refractor velocity is obtained, and the time model algorithm (equation (3.0.2)), also called the *generalized time-depth*, is a measure of the depth of the refractor. Figure 3.1 illustrates both algorithms.

$$t_V = \frac{1}{2}(t_{\Delta F} - t_{\Delta R} + t_{FR}) \quad (3.0.1)$$

$$t_X = \frac{1}{2} \left(t_{\Delta F} + t_{\Delta R} - \left(t_{FR} + \frac{\Delta_F \Delta_R}{V_n} \right) \right). \quad (3.0.2)$$

Here $t_{\Delta F}$ is the travelttime at receiver Δ_F from forward shot point F , $t_{\Delta R}$ is the travelttime at receiver Δ_R from reverse shot point R and t_{FR} is the reciprocal time between the two shot points. V_n is the apparent velocity and

its value is determined from the velocity analysis as explained below.

Figure 3.1 clearly illustrates the parts of the traveltimes adding up in these equations as solid lines and the parts cancelling out as dashed lines. Figure 3.1a sketches the reduction in equation (3.0.1) to the approximate traveltime from shot point F to a point in the refractor below the CMP X .

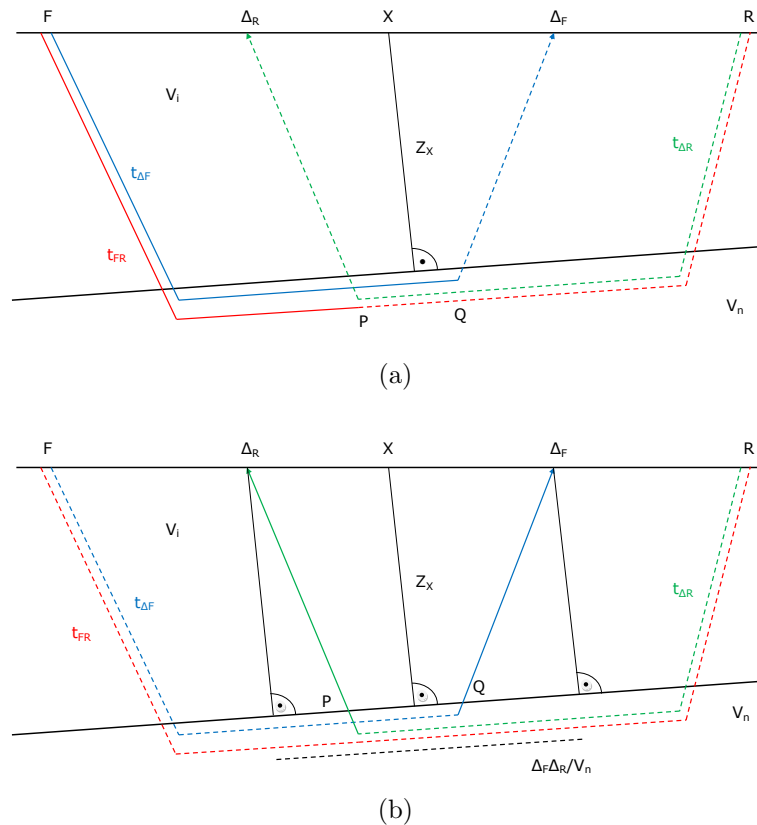


Figure 3.1: GRM inversion algorithms (a) GRM refractor velocity analysis algorithm (equation (3.0.1)) and (b) GRM time model algorithm (generalized time-depth, equation (3.0.2)).

The most important aspect of the GRM method is the determination of the optimum values for the distance $\Delta_F \Delta_R$. Optimum $\Delta_F \Delta_R$ values are found where forward and reverse rays emerge from nearly the same point on the refractor. Two approaches for the determination of $\Delta_F \Delta_R$ values are *Direction calculation of $\Delta_F \Delta_R$ values* and *Observation of $\Delta_F \Delta_R$ values*, but Palmer (1981) does not quote these methods as reliable as the inspection of the velocity analysis and time-depth functions, which use a range of $\Delta_F \Delta_R$ values.

Applying *refractor velocity analysis* finds the optimum $\Delta_F\Delta_R$ value by evaluating equation (3.0.1) for a range of $\Delta_F\Delta_R$ -separations between points F and R with reference point X midway between F and R . Here the paths $X\Delta_R$ and $X\Delta_F$ are equal. Plotting t_V against distance for several $\Delta_F\Delta_R$ values and fit the obtained t_V values for each $\Delta_F\Delta_R$ value leads to the optimum $\Delta_F\Delta_R$ value, where the calculated points have the smallest deviations from the fitted line. Deviations can be both positive and negative which corresponds to the fact that the optimum $\Delta_F\Delta_R$ represents an average value (Palmer, 1981). The $\Delta_F\Delta_R$ value *zero* corresponds to the *conventional reciprocal method* and is similar to the *plus term* in the *Plus-Minus method* by Hagedoorn (1959), which is shortly described in Appendix B.

The fitted line for the optimum $\Delta_F\Delta_R$ has a slope defining the inverse of an apparent refractor velocity, $V_{refractor}$:

$$\frac{dt_V}{d\Delta} = \frac{1}{V_{refractor}} = \frac{1}{V_n}. \quad (3.0.3)$$

In case of major structures in the subsurface, which can be seen by larger deviations from the fitted line, Palmer (1981) developed the following approach for determining the optimum $\Delta_F\Delta_R$ value(s) on either side of the structure. A value for major deviation is defined and from the fitted line the first and last major deviations are found. Positive and negative deviations are connected respectively and their resulting lines intersect on the optimum $\Delta_F\Delta_R$ value. The found value is most likely not the same as the one found at first. This results in several optimum $\Delta_F\Delta_R$ values, one found in the first stage and at least one in the second stage. Each value has its unique advantage with respect to the subsequent processing and interpretation.

The *time model algorithm* t_X (eq. (3.0.2)) provides a measure of the depth to the refracting interface in units of time (Palmer, 2009). Figure 3.1b illustrates the respective ray-paths where the dashed lines cancel each other out and the solid lines remain. The term $\Delta_F\Delta_R/V_n$ represents the additional traveltime in the refractor between the stations Δ_R and Δ_F . It can be seen that the GRM time model is the average of the reverse delay time at Δ_R and the forward delay time at Δ_F . Values of optimum $\Delta_F\Delta_R$ are found by calculating time-depths for a range of $\Delta_F\Delta_R$ values and plot them against distance. For example, for a refractor with two different levels, which are connected by a slope, the calculated t_X values reproduce both the different

levels and slopes with different angles. Where the sloping part is steepest the optimum $\Delta_F\Delta_R$ value is found.

The time model is related to the thickness, Z_i , and the seismic velocity, V_i , of each layer in the weathering layer (Palmer, 2009):

$$t_X = \sum_{i=1}^{n-1} Z_i \frac{\sqrt{V_n^2 - V_i^2}}{V_n V_i}. \quad (3.0.4)$$

Due to large station spacing in most cases it is not possible to define all layers within the weathering layer. In this case the multiplicity of layers in equation (3.0.4) can be replaced with a single layer of total thickness Z_X and an average seismic velocity \bar{V} which leads to the following equations:

$$Z_X = t_X \frac{V_n \bar{V}}{\sqrt{V_n^2 - \bar{V}^2}} \quad (3.0.5)$$

$$\bar{V} = \sqrt{\frac{\Delta_F \Delta_{Roptimum} V_n^2}{(\Delta_F \Delta_{Roptimum} + 2t_X V_n)}}. \quad (3.0.6)$$

This is a unique feature of the GRM. An average vertical seismic velocity in the weathering layer can be computed where an optimum $\Delta_F\Delta_R$ value can be recovered from the refractor velocity analysis function. $\Delta_F\Delta_{Roptimum}$ is selected where the seismic velocity model is the simplest, and this is where the deviations to the straight line are smallest. The depth conversion factor, which is defined as equation (3.0.5) divided by t_X , is relative insensitive to dips up to about 20 degrees as both forward and reverse data are used (Palmer, 1980). This insensitivity makes the GRM an extremely convenient method for dealing with irregular refractors, including those overlain by a layer within which the velocity varies continually with depth (Palmer, 1980).

A $\Delta_F\Delta_R$ -value of zero leads to a considerably smoothed subsurface model and can cause fictitious refractor velocity changes as well as gross smoothing of irregular refractor topography (Palmer, 1981). Best agreement with real conditions is obtained for the optimum $\Delta_F\Delta_R$ value.

Chapter 4

Rayfract[®] Seismic Refraction & Borehole Tomography

For the tomographic inversions the seismic refraction tomography software Rayfract[®] by Intelligent Resources Inc., which is based on Wavepath Eikonal Traveltime (WET) inversion method, is used. The WET inversion is founded upon a back-projection formula for inverting velocities from travel times computed by a finite-difference solution to the Eikonal equation (Qin et al., 1992). Before initiating the WET inversion an initial model needs to be generated. For generating the initial model two methods are available.

One method is the *Delta-t-V method*, which has been developed by Gebrande and Miller (1985). This method creates a Pseudo-2D Delta-t-V initial model and shows the relative velocity distribution in the subsurface. Both systematic velocity increases and strong velocity anomalies such as low velocity zones, faults etc. are visible in many situations (Rohdewald, 1999). The code-developer states that the obtained absolute velocity values may have an error of up to 15 to 20 percent or more. The disadvantage of using its output for the initial model is that there may be artefacts in case of strong lateral velocity variation in the near-surface overburden, which are not removed completely by the subsequent tomography algorithm.

The other method for creating an initial model is the *Smooth Inversion* algorithm, which automatically creates a one-dimensional model based on the Delta-t-V result. Artefacts, which can be produced by the Delta-t-V solutions, are eliminated by the *Smooth Inversion* algorithm, because it starts

with simple models. The artefacts are virtually eliminated and a more reliable solution for the absolute velocity estimates is obtained. The *Smooth Inversion* automatically starts the *WET tomography* processing for subsequent refinement.

Once an initial model has been created it can be refined with the *WET Wavepath Eikonal Traveltime* tomography. Wave propagation is modelled with wavepaths, i.e. Fresnel volumes, also known as *fat rays*, based on an advanced first-order Eikonal solver (forward modelling algorithm for modelling of first breaks).

This chapter discusses the algorithms used in the inversions. First the *Delta-t-V* algorithm by Gebrande and Miller is explained followed by a short description of how the *Smooth Inversion* uses this algorithm, and then the *WET Wavepath Eikonal Traveltime* algorithm is discussed.

4.1 Delta-t-V Inversion

Applying Delta-t-V Inversion results in obtaining the relative velocity distribution of the subsurface. Traveltimes do not have to be mapped to the refractor; all that is needed is to import seismic data and complement with geometry information and traveltime picks (Rohdewald, 1999).

This inversion method has been developed by Gebrande and Miller with the aim of using as much information of the traveltime curve as possible. As the name states, the horizontal offset, Δ , the travel time, t , and apparent velocity, V , are directly considered in this inversion method. One possibility to use these units is by applying the following equations:

$$\Delta(V) = \frac{2}{a} \sqrt{V^2 - v_1^2}, \quad t(V) = \frac{2}{a} \text{Arcosh}(V/v_1) \quad (4.1.1)$$

where a is the velocity gradient, defined as dv/dz , and v_1 is the velocity in the uppermost layer. With the first parameter-triplet Δ_1 , t_1 and V_1 , the velocity v_1 and velocity gradient a_1 can be determined numerically. These values lead also to the depth, z_1 , the ray has reached with the apparent velocity V_1 .

$$z(V) = \frac{\Delta}{2} \sqrt{\frac{V - v_1}{V + v_1}} \quad (4.1.2)$$

Traveltimes and distances of all rays with larger apparent velocity are corrected to z_1 . With the next parameter-triplet the values of the next gradient layer (or layer with constant velocity) are determined and this is continued until the end of the traveltime curve is reached. Zones with lower velocities are discovered and it is secured that the original traveltime curve is obtained again when calculating backwards.

A major drawback of this inversion method is the modelling of artefacts in case of strong lateral velocity variation in near surface overburden. This problem has been overcome by the implementation of *Smooth inversion* which virtually eliminates these artefacts in the initial model and obtains more reliable absolute velocity estimates (see section 4.2).

From the *Delta-t-V* output most weight should be put on the near-surface imaging. Deeper structures are more uncertain wrt. depth and velocity as modelling errors in the overburden are accumulated to the next lower levels. These errors cause deeper traveltimes to be reduced with unrealistic delay times and being under-/over corrected (Rohdewald, 1999). The accumulation of these errors may result in unrealistic high/low velocities beyond certain depths or too shallow/deep interpretations. The reason for this is the specification of uncalibrated values for some Delta-t-V parameters.

Too shallow/deep interpretations can also be caused by a too wide receiver or source spacing. This error can be revealed by applying *forward modelling of first breaks*, which compares modelled traveltimes with measured and picked times. Matching picked and modelled traveltimes proves a reasonable choice of parameters for obtaining the *Delta-t-V* initial model output. In the following section this algorithm is reviewed.

4.1.1 Traveltime Field Computation

Traveltime field computation serves as quality control of depth-velocity models as obtained with Delta-t-V method by forward modelling of wave propagation through these models. Figure 4.1 shows the shot break windows within Rayfract illustrating the differences between modelled and measured traveltimes after 10 and 50 iterations. Modelled traveltimes are coloured blue while measured lines are black. Here the measured traveltimes are synthetically created traveltimes.

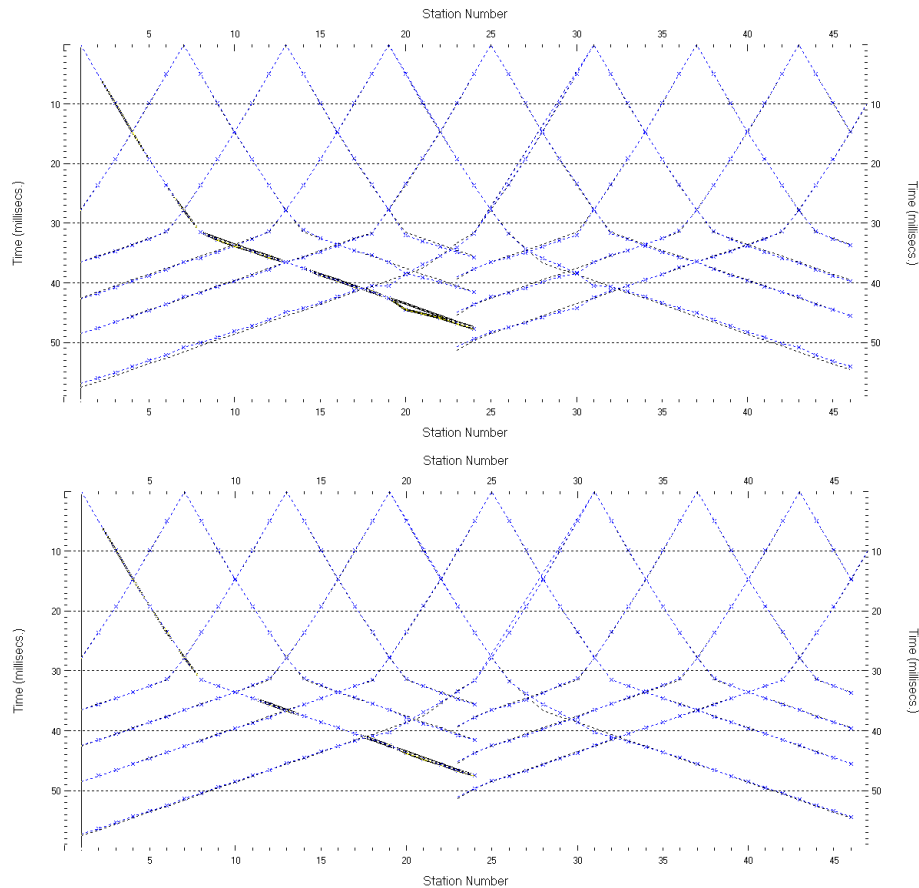


Figure 4.1: Shot break windows illustrating the differences between modelled (blue) and measured (black) traveltimes after 10 (top) and 50 (bottom) iterations. It can easily be seen, that several iterations yield better agreement of the curves.

The forward modelling algorithm is the first-order Eikonal solver, which calculates traveltimes of the fastest wave at any point of a regular grid, including

head waves (Podvin and Lecomte, 1991).

Refraction seismology is mostly based on traveltimes interpretation and this algorithm is capable of finding both, traveltimes and raypaths (Lecomte et al., 2000). Ray tracing can be used to obtain an estimate of the arrival time, but in classical approaches a layer must have a vertical velocity-gradient in order to simulate critically refracted rays back-propagating to the surface. Vidale (1988) proposed a very efficient method to calculate traveltimes on a regular velocity grid by solving the Eikonal equation using finite differences. This type of solution is called an Eikonal solver (Lecomte et al., 2000).

The potential of the Eikonal solver in refraction seismic, both for modelling of traveltimes and inversion, has been shown by Aldridge and Oldenburg (1992), who used a modified version of Vidale's (1988). They demonstrated how to apply the refractor-imaging principle of Hagedoorn (1959)(disussed in Appendix B), which requires back-propagation of the wavefronts associated with head waves. Their major problem was the restriction to a plane topography of the recording surface. This limitation has been overcome by Podvin and Lecomte (1991) by using a more flexible Eikonal solver algorithm based on Vidale (1988).

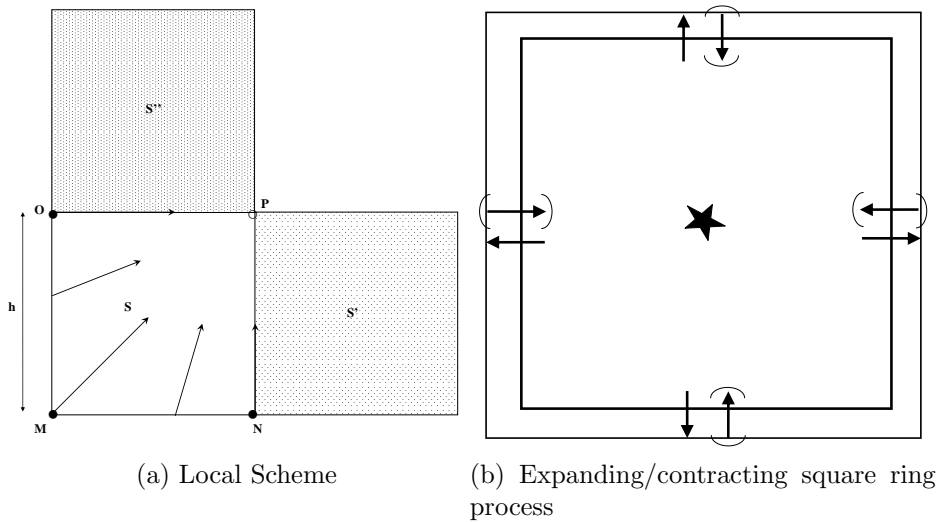


Figure 4.2: (a) Local Scheme with three known traveltimes (t_M , t_N , t_O) for finding the fourth (t_P). Segments [MN], [MO] are plane wave estimators. A diffraction generated from **M** and two surface waves are calculated from the traveltimes at **O** and **N**. (b) The expanding/contracting square ring process with point source in centre. When surface waves are generated along a side of the ring, potential back-propagating head waves are examined by contracting the ring from the respective side. (Lecomte et al., 2000)

Vidale (1988) obtained the Eikonal equation from the elastic-wave equations by searching for plane harmonic solutions and applying the high-frequency approximation of ray theory. In two dimensions this is:

$$\left(\frac{\partial T}{\partial x}\right)^2 + \left(\frac{\partial T}{\partial z}\right)^2 = s^2, \quad (4.1.3)$$

where T is i.e. the travelttime of the wave with slowness s .

Vidale solved equation (4.1.3) by using finite differences to estimate the partial derivatives. Considering the lower left square of figure 4.2a traveltimes are calculated within regular grids where the traveltimes at three out of the four corners are known (t_M , t_N and t_O) and the fourth (t_P) is found by applying the equation he derived (see section A in the Appendix). This equation (see eq: (A.0.1)) has some limitations and a major problem of this algorithm is that the local scheme is applied without considering the surrounding slowness structure.

Podvin and Lecomte (1991) chose an approach where they used the regular grid slowness representation as a physical representation, i.e. the actual slowness model is approximated by a model with square cells of constant slowness. Using the local scheme in figure 4.2a with a wavefront passing point \mathbf{M} first, they found five estimators for the travelttime from which the smallest is kept.

$$t_P = t_N \pm \sqrt{(hs)^2 - (t_N - t_M)^2} \quad \text{for } 0 \leq t_N - t_M \leq \frac{hs}{\sqrt{2}} \quad (4.1.4)$$

$$t_P = t_O \pm \sqrt{(hs)^2 - (t_O - t_M)^2} \quad \text{for } 0 \leq t_O - t_M \leq \frac{hs}{\sqrt{2}} \quad (4.1.5)$$

$$t_P = t_M + \sqrt{2}hs \quad (4.1.6)$$

$$t_P = t_N + h\min(s, s') \quad (4.1.7)$$

$$t_P = t_O + h \min(s, s''). \quad (4.1.8)$$

Here all sides of the cell have the same length, h , and the limits in equations (4.1.4) and (4.1.5) take the angle of the incoming wavefront into account; that is a rather steep wavefront passing first point **M**, then point **O** followed by the centre of the cell leads to the use of equation (4.1.5) while equation (4.1.4) does not fulfill the limit criteria.

In spite of these five estimators, it still makes sense to use Vidale's equation instead of equations (4.1.4), (4.1.5) and (4.1.6) as long as the argument of the square root of equation A.0.1 in Appendix A is not negative.

Head waves propagating along the outer part of one of the cell sides are represented by traveltimes estimators (4.1.7) and (4.1.8). As the head waves initiate wavefronts which may return to previous calculated zones Podvin and Lecomte (1991) introduced an expanding/contracting square ring process (figure 4.2b). From the source point, in the centre of the square, traveltimes are determined along successive square rings using traveltimes from the previous ring. When the two mentioned estimators are used along a side of the current ring, potential head waves are examined by contracting the ring from the respective side until no more traveltimes are updated (decreased).

Systematic application of the estimators, which only use traveltimes on the previous ring, reveals the smallest traveltimes. Then estimators, which use only one point on the previous ring and one on the current ring, are applied in one direction followed by the other direction. A recursive process will follow, if the interface wave estimator has minimized a traveltimes.

Other methods have been developed as well, but they are not as efficient as the described square ring process and shall not be elaborated here. For further reading refer to Lecomte et al. (2000).

4.2 Smooth Inversion

Smooth Inversion uses, as mentioned above, the result of the *Delta-t-V Inversion* method and generates a 1D-gradient initial model. The *Pseudo-2D Delta-t-V initial model*, obtained with *Delta-t-V Inversion*, results in an indi-

vidual velocity vs. depth profile below each profile station. *Smooth inversion* averages the obtained velocities over all profile stations at common depths resulting in an average velocity vs. depth profile. This average velocity vs. depth profile is then extended laterally along the whole profile. A 1D gradient velocity grid is generated based on these average velocities (Rohdewald, 1999). *Smooth inversion* automatically starts the subsequent *WET Wavepath Eikonal Traveltime Inversion* with the default parameters and settings.

4.3 WET Wavepath Eikonal Traveltime tomography

The limitation conventional ray tracing tomography faces, modelling of just one ray per first break, has been overcome by Rayfract by using *WET Wavepath Eikonal Traveltime* tomography, in the following just called WET. WET models multiple signal propagation paths contributing to one first break. Wavepaths are based on *Fresnel volumes*, also known as *fat rays* (treated in section 4.3.1), which take the band-limited effects of the source wavelet and the diffraction effects into account.

The used WET code has been developed by Schuster and Quintus-Bosz (1993) and is based on a finite-difference solution to the Eikonal equation (Schuster, 1991). When scattering effects are dominant or the characteristic scale of the medium is about the same as or smaller than the dominant source wavelength, this principle is invalid.

The starting-point is the general formula for the back projection of traveltime or phase residuals:

$$\gamma(x) = \frac{2s(x)A_{rs}\Delta t}{A_{xr}A_{xs}} \int_{-inf}^{inf} \omega^3 \tilde{R}_{rs}(\omega) \times \sin(\omega[t_{xs} + t_{xr} - t_{rs}]) d\omega \quad (4.3.1)$$

with t_{xs} and t_{xr} the first-arrival traveltime solution to the Eikonal equation for a receiver at x_r and source at x_s , in a slowness distribution $s(x)$; A_{xs} is the associated geometrical spreading term of the first arrival, whose reciprocal satisfies the transport equation; \tilde{R}_{rs} is an arbitrary weighting function, which main effect it is to smooth the gradient (or reconstruct the slowness

field) in a way that is consistent with the source spectrum and the path propagation. Scattering effects in the data are ignored as the phase is linearized with respect to frequency. Equation (4.3.1) is derived from the phase misfit function

$$\epsilon = \frac{1}{2} \sum_s \sum_r \sum_\omega \tilde{R}_{rs}(\omega) \Delta\phi(x_r, x_s, \omega)^2, \quad (4.3.2)$$

with the summation over the receivers r and sources s and over the discrete source frequencies ω . $\Delta\phi(x_r, x_s, \omega)$ is the phase residual, which is determined as the difference between the calculated and observed phases of the first arrivals at a single frequency.

The gradient of ϵ with respect to the slowness yields the gradient of the phase misfit. With this the slowness can be reconstructed. Implementing several definitions, substitutions and linearization of phase with respect to the first-arrival traveltimes finally yields equation (4.3.1).

Applying this equation by substituting certain expressions for the weighting function, \tilde{R}_{rs} , leads to different tomography methods including the WET equation, which will be shown in the following.

Considering the case of an inhomogeneous medium, a narrow-band source with a center frequency ω_c and a bandwidth $2\omega_0$, setting $\tilde{R}_{rs}(\omega)$ to $1/2$, and replacing the integration by

$$\int_{-\omega_c-\omega_0}^{-\omega_c+\omega_0} d\omega + \int_{\omega_c-\omega_0}^{\omega_c+\omega_0} d\omega, \quad (4.3.3)$$

and assuming an ω -value close to zero yields:

$$\gamma(x) = \frac{4\omega_0 s(x) A_{rs} \Delta t}{A_{xr} A_{xs}} \times \text{sinc}''' \left(\frac{\omega_0}{\pi} (t_{xs} + t_{xr} - t_{rs}) \right). \quad (4.3.4)$$

The triple prime indicates the triple differentiation with respect to the argument. Traveltime residuals are back-projected into the medium along 'sinc-paths' (rather than raypaths) and weighted along surfaces of constant phase

or traveltimes (Schuster and Quintus-Bosz, 1993).

Replacing $\tilde{R}_{rs}(\omega)$ in equation (4.3.1) by the magnitude spectrum of i.e. a Ricker wavelet¹ replaces the triple derivative sinc-function by the time domain Ricker wavelet $W'''(t_{xs} + t_{xr} - t_{rs})/2\omega_0$. The asymptotic gradient for the WET inversion is then (Schuster, 1991, Quintus-Bosz, 1992):

$$\gamma(x) = \frac{2s(x)A_{rs}\Delta t}{A_{xr}A_{xs}}W'''(t_{xs} + t_{xr} - t_{rs}). \quad (4.3.5)$$

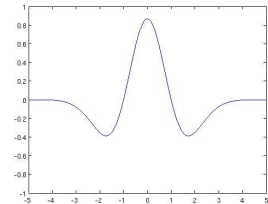
With this equation the wavpath is shaped by the magnitude spectrum of the source wavelet, which is physically consistent with the actual path of wave propagation for a shifted zero phase wavelet.

After the first-arrival traveltimes, t_{rs}^{obs} , have been picked from seismograms the numerical algorithm for WET inversion is:

- to propose an initial slowness model and solve the Eikonal equation by a finite difference method (Qin et al., 1992) to get t_{xs} and t_{xr} . The traveltime residual $\Delta t = t_{rs} - t_{rs}^{obs}$ is computed. t_{rs} are the finite-difference traveltimes.
- to evaluate source weighting function in equation (4.3.5) at all points in the medium yielding $\gamma(x)$. In practice, summation over source and receiver positions are included in order to take multiple sources and receivers into account.
- to update the slowness model and repeat the steps iteratively until convergence. This scheme has been successfully tested for its effectiveness by Quintus-Bosz (1992).

¹Ricker wavelet is the negative normalized second derivative of at Gaussian function. It is defined by the input parameters “wavelet reference (center) time”, t_0 , and “maximum amplitude frequency”, f_m , with the respective units seconds and Hz. In analytical form they are used in $W(t) = \left(1 - \frac{(2\pi f_m(t-t_0))^2}{2}\right) \exp\left(-\frac{(2\pi f_m(t-t_0))^2}{4}\right)$ with the spectrum $S(\omega) = \frac{4\sqrt{\pi}\omega^2}{(2\pi f_m)^3} \exp\left(-\left(\frac{\omega}{2\pi f_m}\right)^2\right) \exp(i\omega t_0)$.

It is also known as the “Mexican hat wavelet” which becomes clear when looking at its curve as illustrated in the figure on the right.



4.3.1 Fresnel volume - Fat Rays

Geometric ray theory is commonly used in seismic imaging. It is an asymptotic solution of the wave equation in the high-frequency limit. It includes the assumption that waves propagate along infinite narrow lines, rays, joining the source and receiver (Spetzler and Snieder, 2004). Infinite narrow lines correspond to infinite frequencies, which is not the case for waves recorded in reality as their frequency content is finite. Limiting the frequency band of waves implies that their propagation is extended to a finite volume around the geometrical ray path. This volume is called the Fresnel volume.

Husen and Kissling (2001) define the Fresnel volume of a seismic wave as the innermost spatial region where constructive interference of seismic energy takes place. Hence, scattering from each point within the Fresnel volume contributes constructively to the signal observed at a receiver.

Solving the Eikonal equations directly guarantees that the global minimum traveltime is found (Husen and Kissling, 2001).

Summation of both travel time fields, the forward and the backward propagating waves, yields the fat ray (Fig. 4.3) representing the wave path from the source to the receiver.

The traveltime fields of both the forward and backward waves are calculated using the finite-difference algorithm as described in chapter 4.1.1. The width of the Fresnel volume is defined by Cerveny and Soares (1992) in terms of travel times t_{sx} , t_{rx} between the source and the receiver respectively, and a point x within the Fresnel volume as

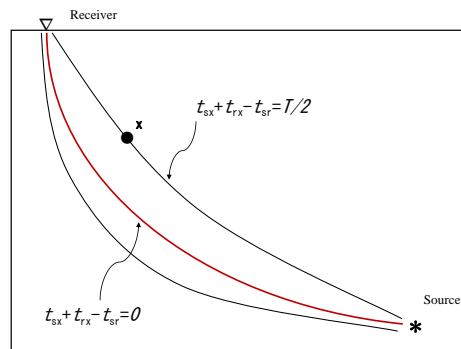


Figure 4.3: Diagram of the fat ray concept. Source and Receiver travel time are computed using finite-difference modelling. Their summation is used to define a fat ray, given those points with a summed travel time less than $t_{sr} + T/2$.

$$|t_{sx} + t_{rx} - t_{sr}| \leq T/2 \quad (4.3.6)$$

where T is the dominant period of the seismic wave and t_{sr} the shortest traveltime between source and receiver. The width of the fat ray should be defined by the points resulting from the equality of equation (4.3.6) in order

to correctly represent the first Fresnel volume. For example, for a dominant frequency of 50 Hz the ideal fat ray width should correspond to points having a 0.01 s travelttime difference. With a refractor of uniform velocity v_2 equal to 5000 m/s and an overburden velocity v_1 of 500 ms the corresponding *minimum fat ray width* of 100 m within the refractor, and 10 m in the overburden, is obtained. In areas of higher velocities the fat ray tends to broaden, which is an expected behaviour of Fresnel zones.

A more theoretical approach is described by Spetzler and Snieder (2004).

Chapter 5

Investigations

For the following investigations the version 3.16 of the tomographic inversion tool Rayfract is used.

In order to understand the capabilities the Rayfract code has to recognize anomalies of different dimensions, locations and properties, a rather thorough sensitivity investigation is necessary to start this work.

A description of how synthetic traveltimes are created is followed by an overview of the models designed for computing the first arrival traveltimes. Then the outcome of the sensitivity investigation is shortly described. The result of this investigation decides the choice of the model for the subsequent parameter investigation. In this chapter all for the inversion relevant settings and parameter options are stated. The results, which have the desired positive impact on the inversions, are discussed in chapter 6, where different combinations of the findings are presented as well.

5.1 Sensitivity Investigation

Synthetic traveltimes are computed by the program using its built in Eikonal solver.

The procedure is to import a set of random traveltimes in form of an ASCII-file, which contains shot positions, receiver positions and first arrival travel-

times. The number of receivers and shots should correspond to the desired set-up. A *Delta-t-V Inversion* is run, which creates a set of files including the grid-file *DELTATV.GRD*, which dictates the frame for the synthetic model; amongst others it states the borders, number of grid-points and spacing between points to be used for the model. The synthetic models have been created with Golden Software Surfer¹. When conducting the *forward modelling traveltimes*, which is an option within the menu-item *WET Tomo*², the created model is imported for the computations. Modelled traveltimes are then exported to an ASCII-file, which contains the first arrival traveltimes of the synthetic model.

Here two sets of data densities are created for nearly all synthetic models. One set of traveltimes is with 48 receivers and 25 shots, with a shot at every second receiver; the other set corresponds to a field setup and consists of two spreads, each with 24 receivers, and the source at every sixth receiver (figure 5.1). This comparison reveals the quality of inversions with a sparse data set compared to a dense data set.

It shall be mentioned that all inversions are run with 50 iterations instead of the default 10 iterations³. As stated by the software developer and verified in pre-studies increases the image contrast with an increased number of iterations.

Fifty iterations is rated as a reasonable choice with respect to inversion time and image quality.

Figure 5.2 illustrates the development of the absolute RMS-error and maximum absolute error versus numbers of iterations for the inversion set-up *PARRES 1* as discussed in section 6.3. Maximum absolute error is the error for a certain trace and shot number.

¹Any other software, which is capable of creating a grid-file (grd.-file), can be used as well.

²In version 3.18 this function is located in the menu point "Model" and the generation of synthetic traveltimes is simplified as the Delta-t-V Inversion is no longer needed.

³For narrow shot spacing (here the set-up with 48 geophones and 25 shots) the default is 20 iterations and for wide shot spacing (here the set-up with 2×24 geophones and 2×6 shots) the default is 10 iterations.

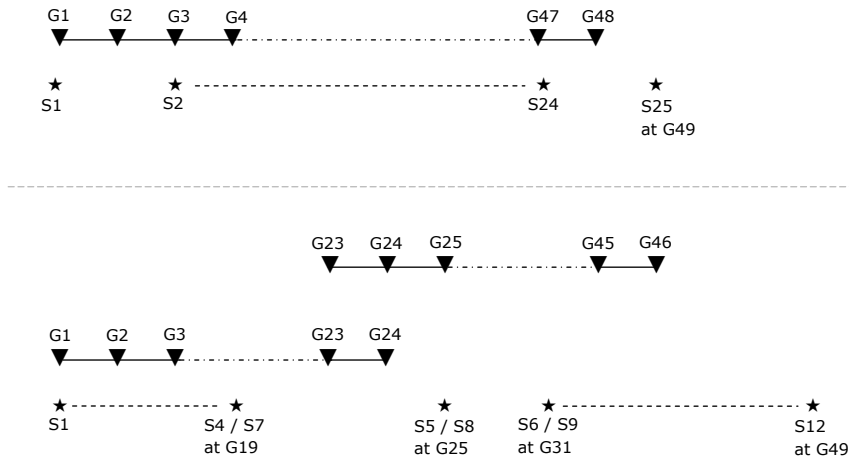


Figure 5.1: Illustration of the used source-receiver set-ups for the sensitivity investigation. The upper part shows the set-up for a spread with 48 geophones and 25 shots, one at every other geophone position. The lower sketch shows a set-up with two spreads, each with 24 geophones, and six shots per spread. The two spreads overlap with two geophone positions and three shot positions. First two geophones of the second spread are numbered 23 and 24 as their position is equal to the last two geophones of the first spread. This way of numbering is important for the processing.

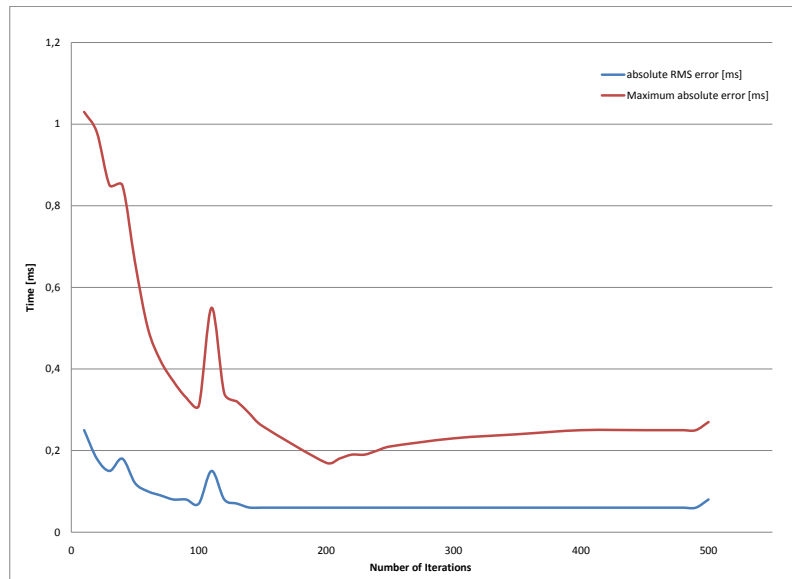


Figure 5.2: Development of the absolute RMS and maximum error in steps of 10 for up to 500 iterations. A minimum of the absolute RMS-error is reached after 140 iterations whereupon it stays constant. The maximum absolute error reaches its minimum after 200 iterations and increases slowly before it jumps in parallel with the absolute RMS-error in the last iteration. This behaviour is explained in the text.

A minimum of the absolute RMS-error is reached after 140 iterations whereupon this value stays constant. The maximum absolute error reaches its minimum after 200 iterations, thereafter its value increases slowly.

The explanation for this is, that the maximum absolute error originates from a certain shot and trace number and varies or can vary for each iteration. Starting with iteration 200, the same trace causes the largest absolute error up to iteration 499. An increase of the error means that the inversion output becomes less dependent on this trace (Rohdewald, 2010). At the last iteration the increase of 0.02 *m/s* originates from a different shot and trace number. With this increase a simultaneous increase of the absolute RMS-error follows as the maximum absolute error is part of its computation.

It shall be noted that this example deals with synthetically modelled travel-times and errors are marginal, therefore it is not necessary to run such a high number of iterations. However, when working with data from field measurements an examination of these errors can help to obtain a more reliable result.

5.1.1 Synthetic Models

For each subsurface structure a synthetic model was designed. All together 27 models were created. The build up of these models is:

- velocity gradient: 1000 *m/s* at top, increasing with 50 *m/s* per metre, and anomalies
 - of $5 \times 5 \text{ m}^2$ and $2 \times 2 \text{ m}^2$ with a constant velocity of 5000 *m/s*,
 - in different locations within the layer: centre, lower centre, upper centre, middle left, upper left and lower left.
 - of $5 \times 5 \text{ m}^2$ with constant velocity of 3000, 2000 and 1500 *m/s*.
- overburden with above velocity gradient and a constant refractor velocity of 5000 *m/s* and
 - $10 \times 10 \text{ m}^2$ and $5 \times 10 \text{ m}^2$ anticlines in the lower centre, lower left.
 - 10 *m* wide synclines penetrating into the refractor.

- overburden with above velocity gradient and a constant refractor velocity of 1000 m/s and
 - $10 \times 10\text{ m}^2$ anticline in the lower centre
- vertically divided area, left side above velocity gradient and
 - right side with a higher velocity gradient
 - right side with a constant velocity of 5000 m/s
- overburden with above velocity gradient, an opening of 100 m in the refractor and
 - a constant refractor velocity of 2000 m/s
 - a constant refractor velocity of 5000 m/s
- Overburden of 5 m thickness and above velocity gradient, constant refractor velocity of 5000 m/s and
 - rift with 10 m opening at interface and 15 degree dipping angle
 - rift with 10 m opening at interface and 75 degree dipping angle
 - rift with 38 m opening at interface and 15 degree dipping angle
 - rift with 38 m opening at interface and 75 degree dipping angle
- Overburden of 5 m thickness and above velocity gradient, refractor velocity gradient with 4000 m/s at interface, increase of 40 m/s per metre and
 - rift with 10 m opening at interface and 15 degree dipping angle
 - rift with 10 m opening at interface and 75 degree dipping angle

Illustrations of all synthetic models can be found in Appendix C.

5.1.2 Results of Sensitivity Investigation

In this section a resumé of the outcome of the sensitivity investigation is given.

For anomalies with larger velocities than the surroundings the code has no

problem in modelling them, neither the $5 \times 5 \text{ m}^2$ nor $2 \times 2 \text{ m}^2$ anomalies. Different locations in the subsurface are recognized as well. But the same box-shaped anomalies are not recognized by the inversion when their velocities are equal to or smaller than their surroundings (see figure C.19). However, an anomaly of larger dimension and in connection with the low velocity refractor is discovered by the code (see figure C.12).

These results show clearly that the set-up used in field surveys (sparse shot and receiver coverage as shown in figure 5.1) is sufficient for being used for the parameter investigation (see figures in Appendix C).

Dipping faults with an opening of 10 m at the interface compose some difficulties. Neither the 15 nor the 75 degrees rift is modelled by the inversion; both are modelled as vertical structures. However, with a larger opening (here 38 m) the code is capable of modelling an angle, though not the original 15 degrees, which is the only model tested with this opening.

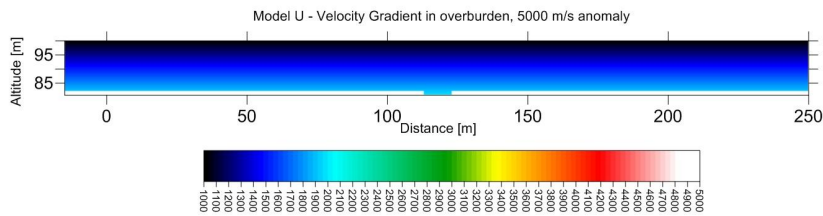
In order to see, if there are traveltimes differences for different dipping angles, an examination of their first arrival traveltimes is carried out. Times for a plane structure (0 degree) and dipping angles of 15 , 75 and 90 degrees are directly compared by subtracting them from each other.

Figure C.28 illustrates the obtained time differences in % with the CMP in station-numbers as x-axis and the offset in station-numbers as y-axis. Differences of first arrival traveltimes between various dipping angles can be observed. With larger differences between the dipping angles the time differences increases as well. This could be caused by the fact that for rifts with larger angles the wavepaths travel a longer distance in the low velocity zone of the rift.

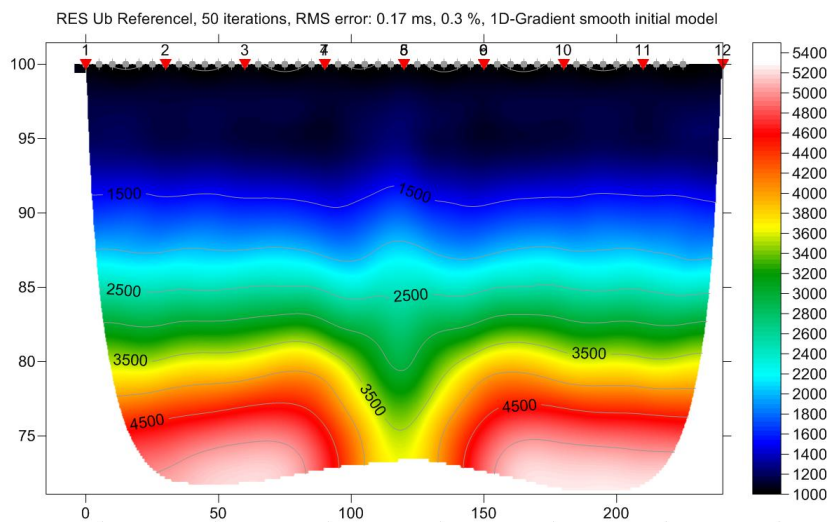
But, are the respective angles of the models disclosed by these plots, too? In the first three sub-figures, where the traveltimes for the plane structure is subtracted from traveltimes for the dipping structures, the time differences are very symmetric, which means that the differences in dipping angles are not revealed. The same symmetry is the case in the fourth sub-figure (figure C.28d). The time difference for the last case does not show this symmetry, which proves, that rifts with different dipping angles and an opening of only 10 m at the same offset are modelled by the code, and not only the opening. Here, time differences of more than 10% are modelled.

5.2 Parameter Investigation

As a consequence of the sensitivity investigation one model was chosen for the following parameter investigation. Criterion for the chosen model was that it, as much as possible, should conform with realistic subsurface geologies. As the most suited model for the investigation model Ub, as shown in Figure 5.3a, was selected. Figure 5.3b illustrates the tomogram obtained for default settings and parameters. Grey dots mark the receiver stations and red triangles the shot positions.



(a) Model U



(b) Tomogram for model U

Figure 5.3: (a) Model for the parameter investigations. The velocity gradient of the overburden starts with 1000 m/s at the surface and increases with 50 m/s per metre; it continues into the anomaly through the hole of 10 m width. The anomaly has a constant velocity of 5000 m/s . (b) Tomogram for model U with two spreads of 24 geophones (grey dots) and six shots (red triangles) per spread. Two receiver positions and three shot positions overlap. Default settings and parameters are used. The resulting absolute and normalized RMS-errors are 0.17 ms and 0.3% respectively. The x-axis states the offset and the y-axis the altitude, both in metres.

Its associated RMS-error is 0.17 ms , which corresponds to 0.3% for the normalized RMS-error. Figure 5.4 illustrates the wavepath coverage belonging to this tomogram.

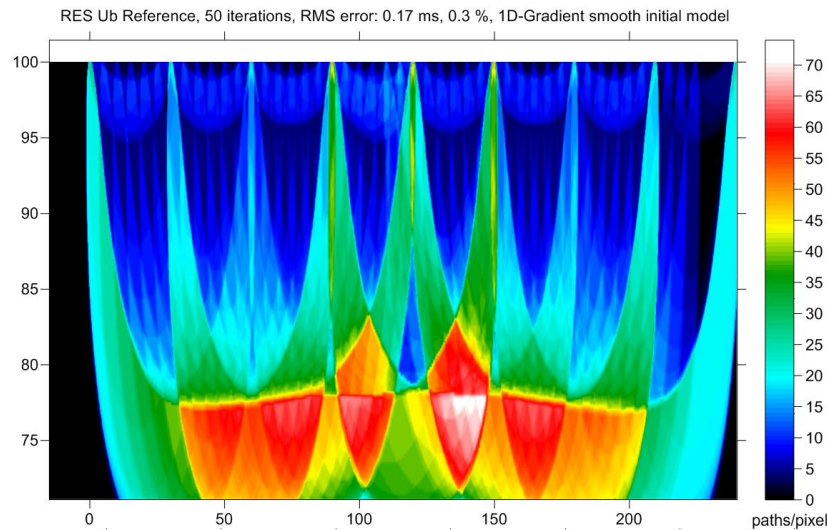


Figure 5.4: Wavepath coverage to the tomogram in figure 5.3b in number of wavepaths per pixel.

Only the case, which corresponds to a field measurement set-up, 2×24 geophones with 2×6 shots, was used for the investigations as the sensitivity investigation showed this to be sufficient, and with future applications in mind.

In order to see the influence of each setting and parameter individually only one at a time was changed compared to default. After all possibilities were tested, the ones, which deliver improved RMS-errors compared to the reference, are combined in the same inversion. This led to several combination possibilities, which gave reasonable improved results.

As mentioned above there are two options for generating initial gradient models for the WET tomography. One is the *Delta-t-V Inversion* which, according to the SW-provider, leads to artefacts in synclines and anticlines. The other is *Smooth Inversion*, which creates a quasi-horizontal subsurface layering based on the *Delta-t-V Inversion*. According to the SW-provider it guarantees a realistic interpretation and velocity artefacts from *Delta-t-V Inversion* are virtually eliminated. Figure 5.5 illustrates initial models generated with both options. The difference between these model is obvious.

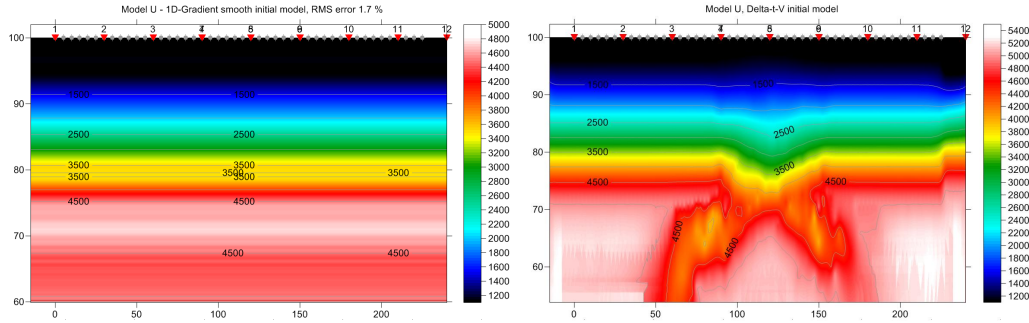


Figure 5.5: Example of the difference between an initial model generated from Smooth Inversion (left) and Delta-t-V Inversion (right).

In this investigation all initial models were created with the *Smooth Inversion*. As the *Delta-t-V Inversion* is the basis for the *Smooth Inversion*, its parameters do have an impact on it, therefore they are tested as well. As the last step the *WET Tomography Inversion* refines the initial model and creates a tomogram of the subsurface. As for the sensitivity investigation all inversions were run with 50 iterations.

The following sections treat each part, *Smooth Inversion*, *Delta-t-V Inversion* and *WET Tomography*, separately describing the applied options and parameters. The inversion results are discussed in chapter 6. For evaluating the quality of the inversions, which is challenging when comparing tomograms, the absolute and normalized RMS-error, as directly calculated by the SW, were used. Nonetheless, an examination of the modelled velocities is conducted, too.

5.2.1 Smooth Inversion Settings

As this inversion is based on the *Delta-t-V Inversion*, there are not many possibilities to influence its settings. No parameters can be set, but there are some options to check and un-check. These options are:

- Lower velocity of 1D-gradient layers:
Should be activated when obtained velocities seem too high. Disabled per default.

- Interpolate velocity for 1D-gradient initial model:
Self explanatory. Checked per default.
- Output inversion results in feet:
Self explanatory and not actual here.
- Strict shot position checking:
Self explanatory. Disabled per default.

Options not active/accessible are not mentioned. *Output inversion results in feet* is not tested as only metric units are considered.

5.2.2 Delta-t-V Inversion Settings and Parameters

As mentioned before, the *Delta-t-V inversion* was not used for the creation of the initial model. But as the *Smooth Inversion* applies its parameters and settings they are tested as well. The *General Delta-t-V Settings* are:

- Output Measured CMP velocities:
When activated inverted velocities and depths are combined with measured velocities at corresponding source-receiver offsets. When not active velocities are only based on inverted velocities. Default is not active.
- Output Horizontal offset of CMP pos. in meters:
Checked per default. Non-active option results in the unit feet.
- Output Delta-t-V results in Feet:
Self explanatory and not actual here. Un-checked per default.
- CMP is zero time trace:
Adds a first break data point with time 0 at offset 0 of the CMP travel-time curve. Checked per default.
- Reduced offset 0.0 is valid trace with time 0.0:
Enabled ensures the fullest use of information in near-offset part of CMP sorted and stacked travelttime curves. Active by default; should be de-activated when output too noisy.

- Enforce Monotonically increasing layer bottom velocity:
Self-explanatory. Not active per default.
- Suppress velocity artefacts:
When active the generation of unrealistic velocity variations is suppressed. Best for medium and high coverage profiles. Per default not enabled.
- Process every CMP offset:
When active a better vertical resolution is obtained, but an increased amount of artefacts might be obtained. Default is disabled.
- Prefer Average over minimum interface velocity:
When enabled the capability of high velocity anomaly imaging in the near surface region is enhanced. Disabled it enhances the low velocity imaging capability of the Delta-t-V inversion. Recommended to leave enabled in case of strong lateral velocity variation. Default is enabled.
- Taper velocity steps at layer interface:
Enabled it may result in an enhanced vertical resolution of subsurface layer interfaces, in case of subhorizontal layering and for high coverage surveys (e.g. 15 or more shots per profile). The resulting model will be slightly too deep i.e. too slow, in most situations. Recommended to leave this option disabled in case of strong lateral velocity variation. Not active per default.
- Smooth CMP traveltimes curves:
To be used for high coverage profiles only. May help to filter out bad picks from CMP sorted and stacked traveltimes curves. For low coverage profiles, enabling this option may result in the destruction of valuable vertical gradient information. Not active per default.
- Weigh picks in CMP curves:
Picked traveltimes curves are weighted. Checked per default.

In *Interactive Delta-t-V* several options and parameters can be chosen. This area is subdivided into group-windows. The main window, *Parameters for Delta-t-V method*, contains the following parameters:

- CMP curve stack width [CMPs]:
Specifies the number of CMP positions for constructing the CMP traveltimes curve. Ranges from 10 to 25 CMPs.

- Regression over offset stations:
Specifies the length of the offset interval for local piecewise linearization of CMP traveltimes curves. A smoothed local apparent CMP velocity is obtained. Small values deliver shallower velocity-depths model, therefore for low coverage surveys values close to the minimum should be chosen. Ranges from 5 to 20 and the linear regression method is chosen in the option below.
- Linear regression method:
 - least squares: *Local apparent CMP traveltimes curve velocities are determined with an offset interval of length 'Regression over offset stations' and centered at the offset currently evaluated. Active per default*
 - least deviations: *This method recognizes outliers and less relevant data points and weighs them less when modelling.*
- Weathering sub-layer count:
For controlling weathering velocity in situations of strong possibly non-linear vertical velocity gradients right below topography. Values range from 0 to 1000 and default is 3. High values yield lower traveltimes. When synthetic traveltimes are too fast this value should be increased.
- Maximum valid velocity:
Limits the maximum velocity of the model to the specified value.
- Process all CMP curves:
 - process all CMP
 - skip every 2nd

Two push buttons, named *Static Corrections* and *Export Options*, open new windows. Window *Static Corrections* contains the following possibilities:

- What static correction
 - No static corrections applied:
In situations of flat topography or topography approximating a dipping plane. First breaks are still corrected for shot position offsets and shot hole depth. These corrections need near-surface weathering velocity, which is determined with the parameter "Weathering crossover" (see below).

- Surface consistent corrections:
Static first break corrections relative to a floating datum obtained by applying a running average smoothing filter. Filter width is specified in field “Topography filter” (see below).
- CMP Gather datum specific:
First break static correction relative to a dipping datum plane specific to the CMP gather. The datum plane is obtained by linear regression of all sources and receivers connected to the actual CMP.
- Determination of weathering velocity
 - Copy v0 from Station editor:
Reuses weathering velocities specified in Station editor. Not actual here.
 - Automatically estimate v0:
Force estimation of a general laterally varying near-surface velocity based on the laterally constant crossover distance “Weathering crossover”. This option is active per default.
- Station number intervals [station nrs.]
 - Weathering crossover:
Specifies the laterally constant estimated average crossover distance separating direct wave-arrivals from refracted arrivals.
 - Topography filter:
Specifies the filter width for the running average filter applied to topography to obtain a smoothed floating datum.
- Trace weighting in CMP stack [1/stat.nrs.]
 - Inverse CMP offset power:
Weighs individual traces in one CMP stack based on the actual CMP offset from the central CMP. Default value is 0.5 and decrease of it gives more weight to large CMP offsets. This option is active by default and the default value is kept for all investigations.

Options and parameters within the window *Export Options* are not tested and therefore not mentioned here. Only the option *Maximum velocity exported* influences the generation of the initial model; the default value of this parameter is kept.

5.2.3 WET Tomography Inversion Settings and Parameters

General Settings which can be checked/un-checked are listed below. Most functions are clear from their name and do not need further explanation; where necessary the purpose of the function is explained.

- Write grids for every iteration:
No effect on the inversion itself. After each iteration a grid-file is generated.
- Update imaged grid depth: *checked per default*
- Adjust wavepath width:
Enabled WET determines the wavepath width for each trace individually. Improved overburden resolution and more smoothing/less artefacts in the basement are ensured. When disabled the constant wavepath width (see "Interactive WET tomography") is used. For profiles with 72 or more receiver stations this option is enabled per default.
- Scale WET filter height:
Scales smoothing filter height with depth below topography. Ensures better vertical resolution of weathering layer and fewer artefacts at the bottom of WET tomograms. For profiles with 72 or more receiver stations this option is enabled per default.
- Blank low coverage after each iteration
- Blank low coverage after last iteration
- Blank below envelope after each iteration
- Blank below envelope after last iteration: *checked per default*
- Interpolate missing coverage after last iteration
- Disable wavepath adjustment for wide shot spacing: *checked per default*
- Reset WET tomography setting to default

Interactive WET tomography has the following options:

- Number of WET tomography iterations:
Specifies the number of WET tomography iterations. Default is 10 iterations (see footnote 3 on page 30). All investigations are performed with 50 iterations.
- Central Ricker wavelet frequency:
Central frequency of the Ricker wavelet used to modulate the wavepath misfit gradient amplitude. Default value is 50 Hz which is kept during the investigations.
- Degree of differentiation of Ricker wavelet:
This number specifies how many times the Ricker wavelet should be differentiated. Recommended to keep the default value of 0 resulting in a more robust tomographic inversion and fewer artefacts.
- Wavepath width [percent of one period]:
Specifies the wavepath width in percent of one period of the Ricker wavelet central frequency. Ranges up to 10 % (and 100 % in version 3.18). Increased value corresponds to wider wavepaths and smoother velocity models.
- Envelope wavepath width [percent of period]:
Specifies the width of the wavepaths used to construct the envelope at the bottom of the tomogram. Recommended value is 0, its maximum possible value is 0.1 % smaller than “Wavepath width”.
- Maximum valid velocity [m/sec]:
Specifies the maximum valid velocity when processing CMP curves and overrides the specified value of Interactive Delta-t-V maximum valid velocity. Velocities exceeding this threshold are reset to the specified value.

Furthermore there are the push buttons named *Edit velocity smoothing* and *Edit grid file generation*. Options within *Edit velocity smoothing* are:

- Full smoothing after each tomography iteration:
Results in smoother tomograms. Recommended for the first (i.e. first ten) WET iterations. This option is chosen per default.
- Minimal smoothing after each tomography iteration:
Results in tomograms with more details. Recommended for the last few (i.e. last ten) WET iterations.
- Manual specification of smoothing filter. These specifications are the Smoothing filter dimensions
 - Half smoothing filter width:
Number of columns scanned on each side of the current cell.
 - Half smoothing filter height:
Number of rows scanned above and below the current cell.
- Filter shallow dipping wavepath artefacts from model
 - Automatically adapt shape of rectangular filter matrix:
Suppresses artefacts. Recommended to leave checked.
- Maximum relative velocity update after each iteration
 - Maximum velocity update:
Specifies the maximum allowed relative update of each velocity model cell after each iteration. Updates will be limited by this threshold. Per default this value is set to 15 % and it ranges from 5 % to 35 %.

Options within the push button *Edit grid file generation* do only have impact on the files generated after each iteration and not on the tomographic inversions. Therefore no inversions for examining them are carried out and they are not elaborated any further.

Chapter 6

Results of the Parameter Investigations

In this chapter the settings and parameters, which have a positive impact on the inversion results for the synthetic traveltimes computed from model Ub, are discussed. This means, only inversions with reduced absolute/normalized RMS errors are discussed. An overview of the remaining tomograms and their respective RMS-errors can be found in Appendix D.

6.1 Smooth Inversion

6.1.1 Smooth Inversion Settings

From all possible settings within *Smooth Inversion* the options *Lower velocity of 1D-gradient layers* activated, and *Interpolate velocity for 1D-gradient initial model* deactivated, yield lower RMS-errors compared to the reference. In the first case an absolute RMS-error of 0.16 *ms* and in the second case of 0.15 *ms*, which corresponds to an improvement of 0.01 *ms* (6 %) and 0.02 *ms* (12 %) respectively, is obtained. Table 6.1 gives an overview of all results and figure 6.1 shows their tomograms.

In table 6.1 an overview of the obtained inversion results is shown.

Smooth Inversion Setting	option	RMS-error
Default Settings		0.17 <i>ms</i>
Lower velocity of 1D-gradient layers	activated	0.16 <i>ms</i>
Interplate velocity for 1D-gradient initial model	de-activated	0.15 <i>ms</i>
Strict shot position checking	activated	0.17 <i>ms</i>

Table 6.1: Smooth Inversion settings with respective absolute RMS-error after 50 WET iterations.

The difference in absolute RMS-error seems small and at first glance their tomograms are almost identical with the reference.

Taking a closer look at the contour-lines reveals a difference in altitude compared to the reference model. In the upper tomogram the contour line for 1500 *m/s* is located at about the 90 *m* mark while it is above this mark in the reference model. This agrees very well with the synthetic model which has exactly the same velocity at this altitude. Reaching the anomaly, at about 81 *m*, does not show any difference, but beneath a slight uplift of the 4500 *m/s* line is observed. Both the 1500 and 4500-line are indications of causing the decrease of absolute RMS-error.

In the lower tomogram the 1500-line is moved further below the 90 *m* mark. This is worse compared to the synthetic model. Looking at the area below the intersection, a further increase of the velocity is revealed in the lower half-space. The 4500-line is lifted up to about 77 *m*.

Activating the option *Strict shot position checking* yields exactly the same inversion result as the default settings. Since the task of this option is to check whether the traveltimes are picked correctly in relation to the shot position this result is as expected.

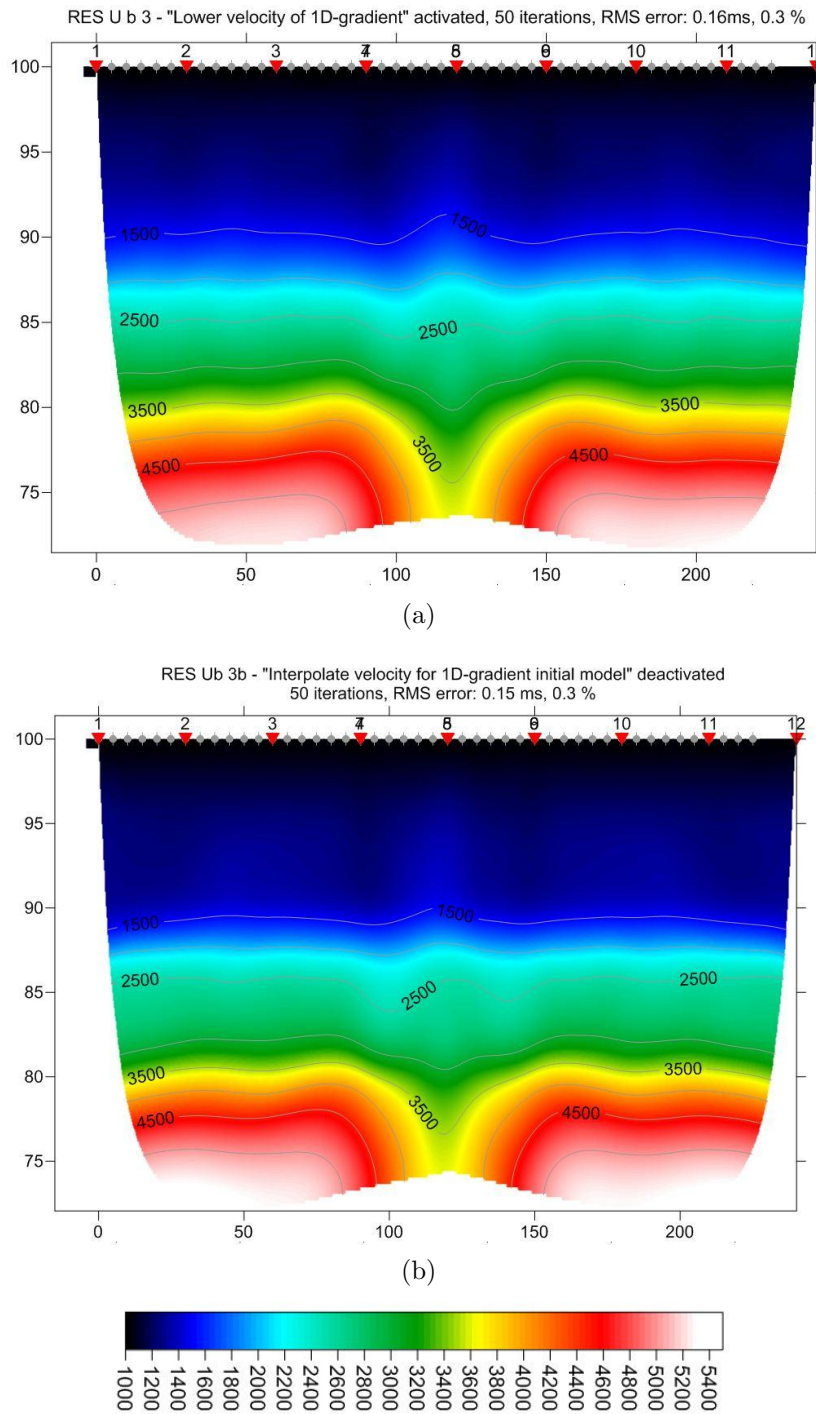


Figure 6.1: Tomograms for model U with (a) "Lower velocity of 1D-gradient layers" activated, (b) "Interpolate velocity for 1D-gradient initial model" deactivated. The improvement in figure (a) is 0.01 *ms* and 0.02 *ms* in figure (b). The normalized RMS-error is not changed.

6.1.2 Delta-t-V Inversion

General Options:

An overview of the obtained inversion results is given in table 6.2.

Delta-t-V Setting	option	RMS-error
Default Settings		0.17 <i>ms</i>
Output measured CMP velocities	activated	0.17 <i>ms</i>
CMP is zero time trace	de-activated	0.17 <i>ms</i>
Reduced offset 0.0 is valid trace with time 0.0	de-activated	0.17 <i>ms</i>
Enforce Monotonically layer increasing bottom velocity	activated	0.18 <i>ms</i>
Suppress velocity artefacts	activated	0.17 <i>ms</i>
Process every CMP offset	activated	0.15 <i>ms</i>
Prefer Average over minimum interface velocity	de-activated	0.17 <i>ms</i>
Taper velocity steps at layer interfaces	activated	0.17 <i>ms</i>
Smooth CMP traveltimes curves	activated	0.27 <i>ms</i>
Weigh picks in CMP curves	de-activated	0.17 <i>ms</i>

Table 6.2: Absolute RMS-error after 50 iterations and the respective Delta-t-V settings applied different from default. Initial gradient models have been created with Smooth Inversion, Delta-t-V has not been run.

From all possible settings, only the option *Process every CMP offset* shows an improvement in the inversions. After 50 iterations the obtained absolute RMS-error of 0.15 *ms* improves the default by 0.02 *ms* or 12 %. Figure 6.2 shows the tomogram while the remaining tomograms are illustrated in figure D.3 in Appendix D.2.2.

Activation of *Process every CMP offset* moves the 1500 *m/s*-line down to the 90 *m*-mark, where its velocity is in conformance with the synthetic model. For the 3000 *m/s*-line a less deep minimum is observed in the centre, where the 'hole' is located. The horizontal area of the 3500-line is moved slightly up compared to the default setting while its minimum has not changed. An increase of the velocity below the 3500-line is a positive response as the synthetic model has a velocity of 5000 *m/s* below this line.

For the remaining inversions either the same or worse RMS-errors as for the reference model are obtained. Their tomograms are almost equal to the reference, some cases show the before observed less distinct minimum of the 3000-line, which is an unwanted effect.

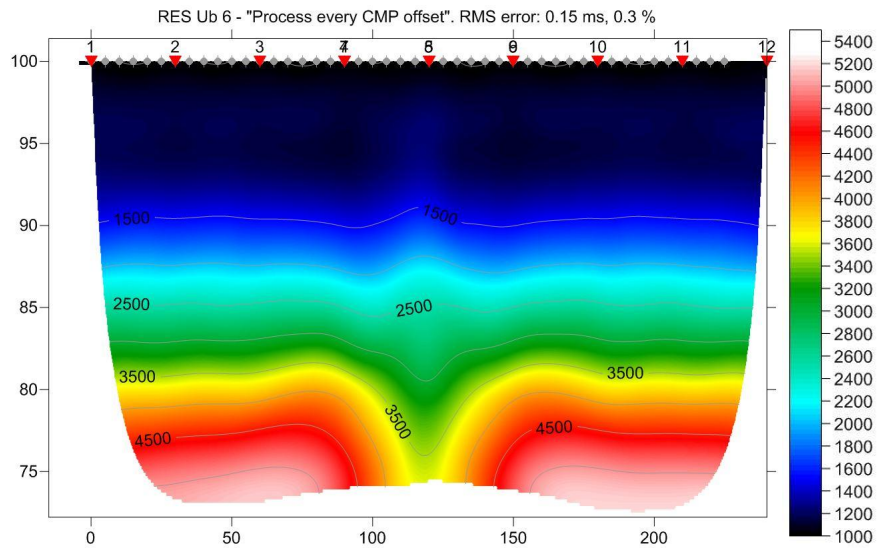


Figure 6.2: Tomogram with Delta-t-V option "Process every CMP offset" activated. An absolute RMS-error of 0.15 ms , which is an improvement of 0.02 ms , is obtained.

Interactive Delta-t-V:

All investigated parameters within the *Interactive Delta-t-V* dialogue-boxes result in exactly the same RMS-error as for the default settings. Table D.1 in Appendix D.2.3 gives an overview over all conducted inversions and the respective RMS-error results. As both, RMS-errors and tomograms equal the reference model their tomograms are not shown.

6.2 WET Tomo

6.2.1 General WET Tomo Settings

As seen in table 6.3 only deactivating the option *Blank below envelope after last iteration* shows an absolute RMS-error improvement of 0.01 *ms*, 6 %. Comparing this tomogram (figure 6.3) with the reference model reveals that the only difference is in the bottom area. The reference tomogram is computed to about 70 *m* altitude while this tomogram reveals velocities down to about 65 *m* altitude.

When enabled, the blanking is active after the last WET iteration, but before forward modelling over the final tomogram for the determination of the RMS error after the last iteration. Disabling this option results in wavepaths (rays), which are modelled deeper into the subsurface. This may result in smaller RMS-errors (Rohdewald, 2010).

The remaining inversions result in either the same or worse RMS-values and their tomograms do not show any improvement towards the synthetic model. An overview of all obtained tomograms is depicted in figure D.4 in Appendix D.3.

WET TomoSetting	option	RMS-error
Write grids for every iteration	checked	0.17 <i>ms</i>
Update imaged grid depth	un-checked	0.18 <i>ms</i>
Adjust wavepath width	un-checked	0.18 <i>ms</i>
Scale WET filter height	un-checked	0.18 <i>ms</i>
Blank low coverage after each iteration	checked	0.17 <i>ms</i>
Blank low coverage after last iteration	checked	0.17 <i>ms</i>
Blank below envelope after each iteration	checked	0.27 <i>ms</i>
Blank below envelope after last iteration	un-checked	0.16 <i>ms</i>
Interpolate missing coverage after last iteration	checked	0.88 <i>ms</i>
Disable wavepath adjustment for short profile	un-checked	0.17 <i>ms</i>

Table 6.3: RMS-error results for the respective general WET Tomography setting after 50 WET iterations for each inversion. Initial gradient model created with Smooth Inversion.

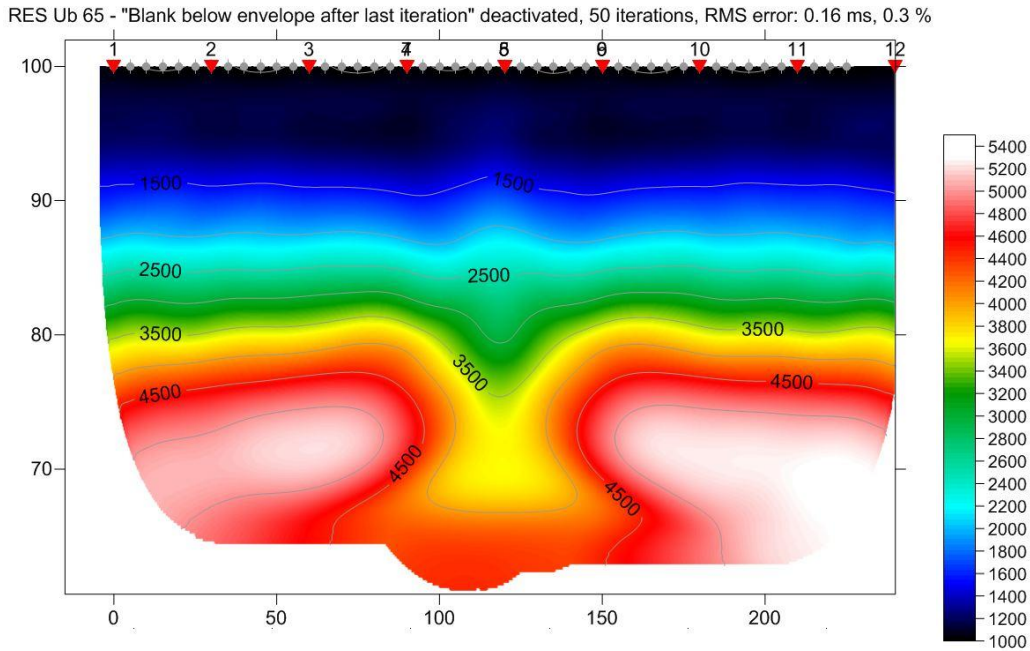


Figure 6.3: Tomogram with WET-Tomo option “Blank below envelope after last iteration” deactivated. An absolute RMS-error of 0.16 *ms*, which corresponds to an improvement of 0.01 *ms*, or 6 %, is obtained.

6.2.2 Interactive WET Tomo Parameters

As mentioned before all parameter investigations are carried out with 50 iterations and changing the *Central Ricker frequency* does not show any systematic behaviour; therefore, these parameters are not changed in this investigation.

Field data, obtained with an explosive source, filtered for the first arrivals from P-waves, and Fourier transformed, result in central frequencies between 50 and 80 *Hz*. As the frequency is different for each shot, perfect fitting frequency can never be found for a whole line as several shots are conducted.

Table 6.4 shows that lower values for the option *Wavepath width* decrease the absolute RMS-error by up to 0.03 *ms*, 18 %. A wavepath width of 10 % (of the Central Ricker wavelet) yields an absolute RMS-error of 0.28 *ms* while 1 and 2 % yield 0.14 *ms*. For the latter cases the tomograms emphasize the ‘hole’ in the anomaly stronger, and the velocities are lower as seen from the 3000-line, which reaches down to about 77 *m* (figure 6.4a with 2 %). Also

at offset 120 *m* (just beneath shot number eight) an area of lower velocity is spotted around the inlet of the 'hole'. This area is a bit more clear in the 1 %-case.

Interactive WET-Tomo Parameter	value/option	RMS-error
Number of WET iterations	50	0.17 <i>ms</i>
Central Ricker frequency	50	0.17 <i>ms</i>
Degree of differentiation of Ricker wavelet	1	0.16 <i>ms</i>
Wavepath width	1 %	0.14 <i>ms</i>
Wavepath width	2 %	0.14 <i>ms</i>
Wavepath width	2.5 %	0.15 <i>ms</i>
Wavepath width	5 %	0.19 <i>ms</i>
Wavepath width	10 %	0.28 <i>ms</i>
Envelope wavepath width	3.4 %	0.16 <i>ms</i>
Envelope wavepath width	3.0 %	0.16 <i>ms</i>
Envelope wavepath width	2.0 %	0.16 <i>ms</i>
Minimal Smoothing	checked	0.15 <i>ms</i>
Manual Smoothing	16 / 2	0.17 <i>ms</i>
Manual Smoothing	20 / 4	0.20 <i>ms</i>
Manual Smoothing	10 / 1	0.16 <i>ms</i>
Filter shallow dipping wavepath artefacts from model	un-checked	0.16 <i>ms</i>
Maximum relative velocity update after each iteration	5 %	0.17 <i>ms</i>
Maximum relative velocity update after each iteration	20 %	0.17 <i>ms</i>
Maximum relative velocity update after each iteration	30 %	0.17 <i>ms</i>

Table 6.4: Overview of WET Tomography results for the respective Interactive WET Tomography parameters after 50 iterations. The first two parameters are fixed during the whole investigation as pre-investigations prove them to be a reasonable choice for the parameter investigation.

The option *Envelope wavepath width* can maximum be set to 0.1 % below the chosen wavepath width value. When setting this value to the maximum possible (in relation to default of 3.5 %) a slight improvement of 0.01 *ms*, compared to reference, is observed. Exactly the same result is obtained for the values 3.0 and 2.0 %. This parameter specifies the width of the wavepaths used to construct the envelope at the bottom of the tomogram. It yields a

somewhat deeper image with the trade off of a more uncertain tomographic image. From the tomogram (figure 6.4b) with this parameter applied no improvement of the upper area can be observed.

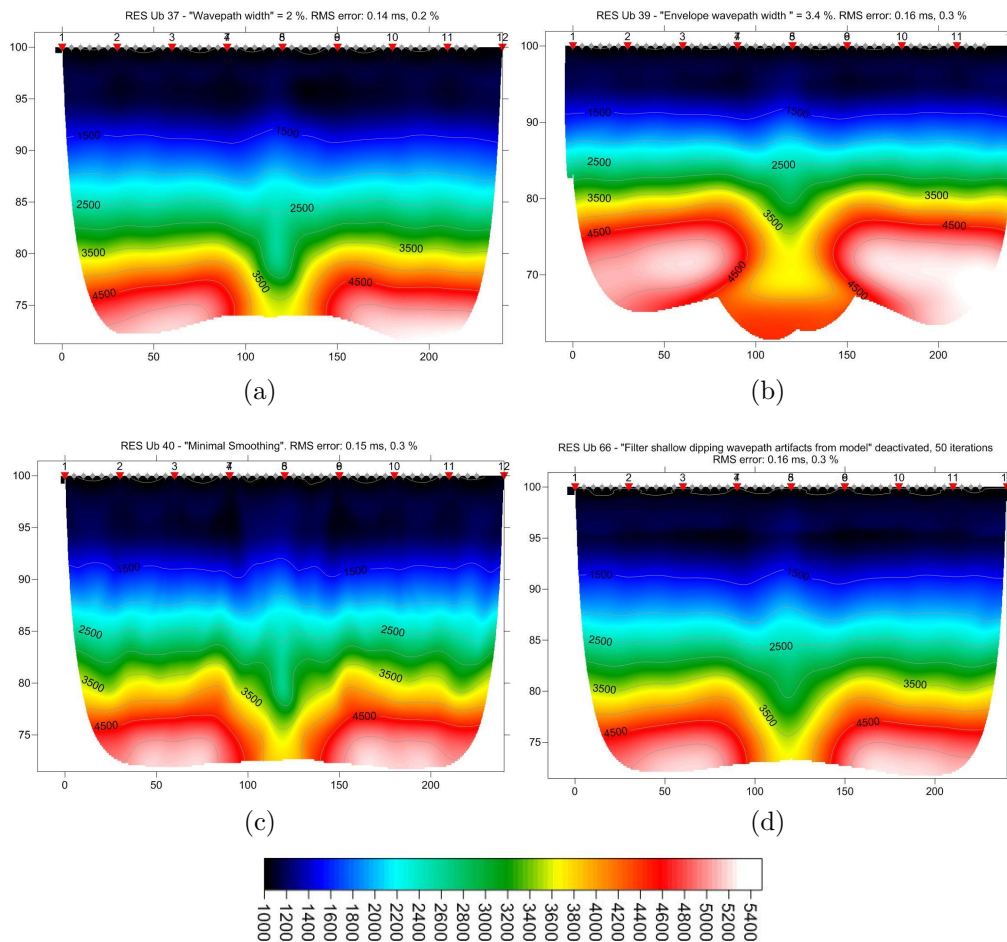


Figure 6.4: Tomograms with improved RMS-error for applied parameters in Interactive WET Tomography. Figure (a) for Wavepath width of 2 %, figure (b) for Envelope wavepath width of 3.4 % (maximum 0.1 % below wavepath width value), (c) for option Minimal Smoothing activated and (d) for option Filter shallow dipping wavepath deactivated.

Minimal Smoothing after each tomography iteration results in a 0.02 ms lower RMS-value. It can clearly be seen in the tomogram (figure 6.4c) that the contour lines are at about the same position as the reference, but more rippled. On the other hand the syncline is emphasized more clearly by a sharper 3200-contour line. This option is recommended for use when more iterations are run, but the ripples can distort the interpretation of the subsurface. This is

clearly illustrated by, for example, the yellow line in figure 6.4c, which marks a velocity of 3700 *m/s*. Here the area from 75 to 80 *m* is modelled much wider than the reference.

De-selecting the option *Filter shallow dipping wavepath artefacts from model* yields a slightly better RMS-value than the reference. This option is recommended by the SW-supplier to be activated (see Rohdewald (1999)). Comparing this tomogram (figure 6.4d) to the reference does not show any differences observable by the naked eye.

6.3 Combined Settings

Settings and parameters leading to a lower absolute RMS-error have now been gathered. Improved results in relation to default settings were obtained for following settings and parameters:

- Smooth Invert Settings
 - *Lower velocity of 1D-gradient* activated
 - *Interpolate velocity for 1D-gradient initial model* de-activated
- Delta-t-V Settings
 - *Process every CMP offset* activated
- Interactive WET Tomo parameter
 - *Wavepath width* set to 2.0 or 1.0 %
 - *Filter shallow dipping wavepath artefacts from model* deactivated
 - *Determination of smoothing filter dimensions* set to *Minimal smoothing after each tomography iteration*

Applying these settings in different combinations, but not all of them applied at the same time, lead to two combinations, which give the lowest absolute RMS-error. Table 6.5 lists these combinations and their respective RMS-errors after 50 and 250 iterations and figure 6.5 illustrates the respective tomograms.

Here inversions have been run with 250 iterations as well in order to see the

maximum possible improvement of the RMS-error and image contrast. Note that deactivating the option *Blank below envelope after last iteration* contributes to an improvement as well.

After 50 iterations a reduction of the absolute RMS-error of 30 % is achieved. For 250 iterations (see figure D.1 on page 99) the reduction is in the order of 54 %.

Parameter/Setting	value/option	RMS-error		Fig.
		50 it.	250 it.	
PARRES 4				
Lower velocity of 1D-gradient layer	activated	0.12 <i>ms</i>	0.06 <i>ms</i>	6.5a/
Process every CMP offset	activated			6.5c
Blank below envelope after last iteration	de-activated			
Wavepath width	2 %			
Smoothing	Minimal			
PARRES 6				
Lower velocity of 1D-gradient layer	activated	0.12 <i>ms</i>	0.06 <i>ms</i>	6.5b/
Process every CMP offset	activated			6.5d
Blank below envelope after last iteration	de-activated			
Filter shallow dipping wave-path artefacts from model	un-checked			
Wavepath width	2 %			
Smoothing	Minimal			

Table 6.5: Combinations of options and parameters yielding the lowest absolute RMS-error. Each combination was run with 50 and 250 iterations. The column on the right states the respective sub-figure in figure 6.5.

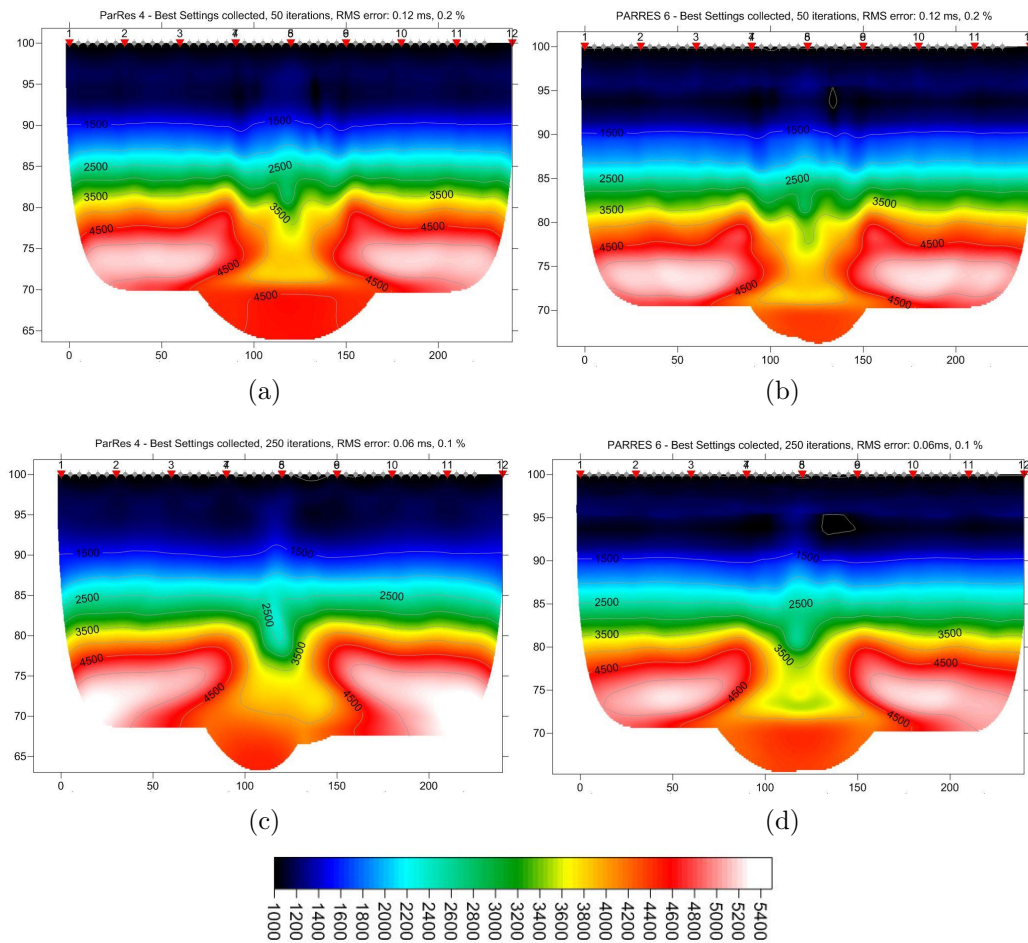


Figure 6.5: Best obtained tomograms with different combinations of parameters and settings found in the parameter investigation. The respective combinations are stated in table 6.5. On the left the first case is shown with 50 iterations (a) and 250 iterations (c). The right column shows the second case for 50 and 250 iterations in (b) and (d) respectively.

All combinations and their respective absolute RMS-errors are shown in the Appendix, table D.2, and the respective tomograms in figures D.6 and D.7.

Choosing a random distance in the tomogram and average the velocity over a range of 10 m horizontal distance illuminates the increase of velocity-contrast as illustrated in figure 6.6 for all six combinations and the reference model after 250 iterations.

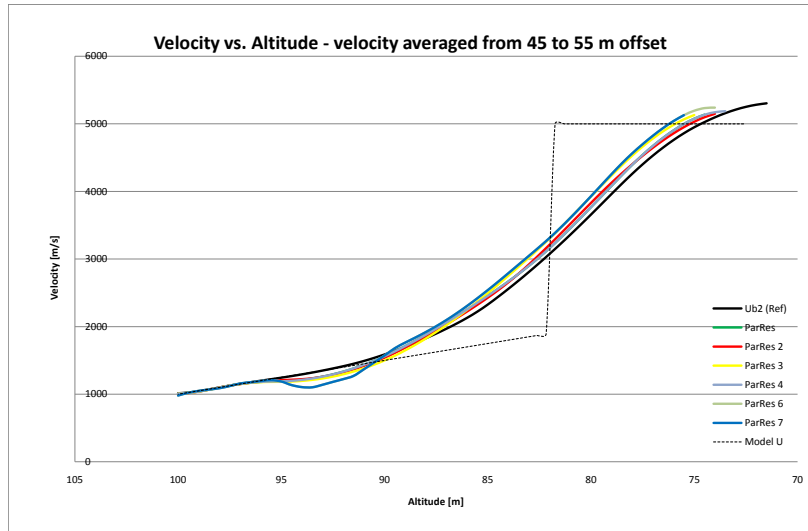


Figure 6.6: Development of the velocity versus altitude for the six combinations in table D.2 and the reference model after 250 iterations. The velocities are averaged between 45 and 55m. The dashed line illustrates the synthetic model. Lines are according to the table and tomograms: ParRes = (a), ParRes2 = (b), ParRes3 = (c), ParRes4 = (d), ParRes6 = (e) and ParRes7 = (f).

The lines following the dashed line as close as possible, or with the steepest slope between 80 and 85 m altitude, reflect the largest velocity contrast. None of these lines are close to the dashed line and the sloping angle is identical for all. Closest to the dashed line is Ub2(Ref), the reference model, but only between the surface and refractor. The second best choice would be the parameter combination *PARRES 4*. Below the intersection, this is below 82 m altitude, the curves obtained with combinations *PARRES 6* and *PARRES 7*, which are equal, approximate the dashed line best; they are followed by the curve for the combination *PARRES 3*.

In summary, none of the combinations increase the velocity contrast noticeably. Their slopes at the intersection between overburden and refractor are equal to the reference model and the velocities are not much closer to the the 'real' one.

Even so this completes this investigation; the absolute RMS-error has been reduced significantly and this knowledge will be verified in the following chapter.

Chapter 7

Case Ørbekk

Ørbekk is a town about 80 *km* north of Oslo in the Akershus community, close to Norway's largest lake Mjøsa.

Because of planned improvements to the highway E6 and the railway in that area, Ørbekk is one of three areas where seismic measurements have been conducted in 2008 by Rambøll Danmark for *Statens Vegvesen*¹ and *Jernbaneverket*². Further surveys have been made in Korslund and Morskogen, both located north of Ørbekk. Data have been processed with the layer based interpretation tool GRM and the tomographic inversion tool Rayfract.

For enhancing their understanding of these methods, NGU (*Norges geologiske undersøkelse*³) performed further surveys by means of resistivity and IP (Induced Polarity) measurements, and re-processed the refraction seismic data with a different tomographic inversion tool. All results are interpreted, compared, and documented in Rønning et al. (2009).

The conclusion for this particular area is that tomographic inversion with Rayfract agrees to some degree well with the GRM method except for some details. Nevertheless, there are some discrepancies and as the tomographic inversion of the Ørbekk-data then was made with Rayfract's default settings and parameters, an attempt to improve the contrast of the obtained tomographic image is made.

¹Norwegian Public Roads Administration

²Norwegian National Rail Administration

³The Geological Survey of Norway

For this a synthetic model, corresponding to a certain section of the real profile, is created. The topography of this area resembles a small valley and the subsurface contains a rather wide low velocity area with an offset from the centre of the valley. Information about the topography, receiver positions and shot positions are extracted from the field data.

Figure 7.1 illustrates the synthetic model and figure 7.2 the tomogram with default settings after 50 iterations. Figure E.1 in Appendix E illustrates the initial model for the subsequent WET inversions.

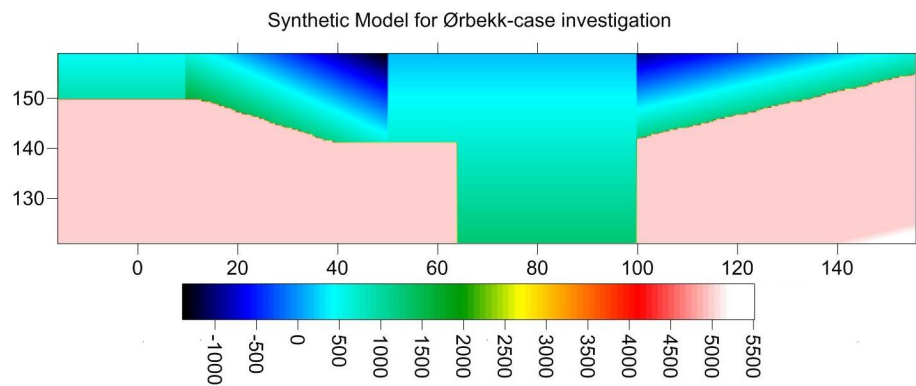


Figure 7.1: The synthetic model for Ørbekk case study resembles an extract of the original profile as interpreted from the measured traveltimes. The negative velocity area in the top of the model is not considered in the inversions as receiver stations and shot positions are located about the 500 m/s level. The velocity gradient of weathering layer runs parallel to the slopes.

Default settings yield an absolute RMS-error of 3.21 ms corresponding to a normalized RMS-error of 2.6 %. The slopes are modelled nicely, especially on the left side, and the low velocity zone between 62 and 100 m offset is modelled correctly.

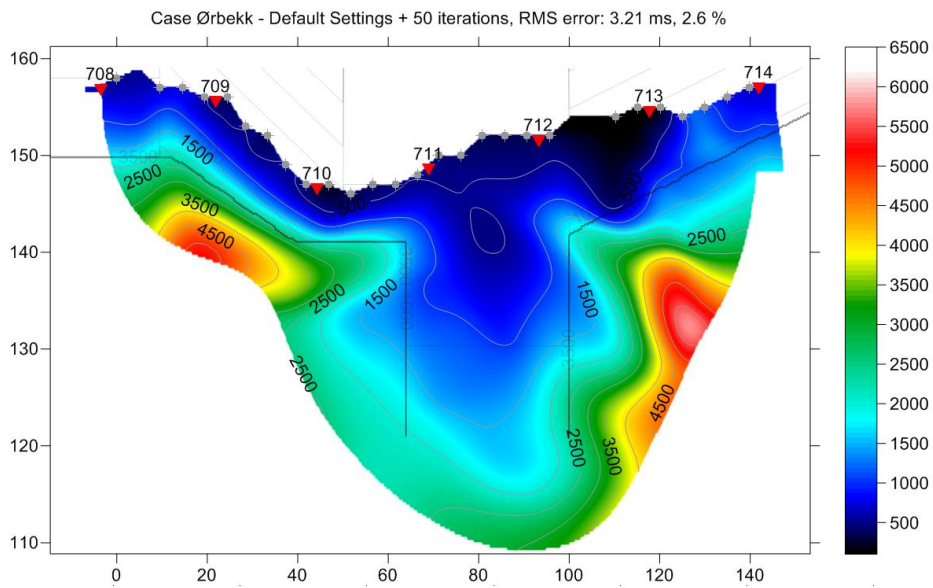


Figure 7.2: Inversion result for traveltimes computed with model in figure 7.1 and shot- and station-coordinates from field measurements. Default settings and 50 iterations. Grey contour lines mark the synthetic model.

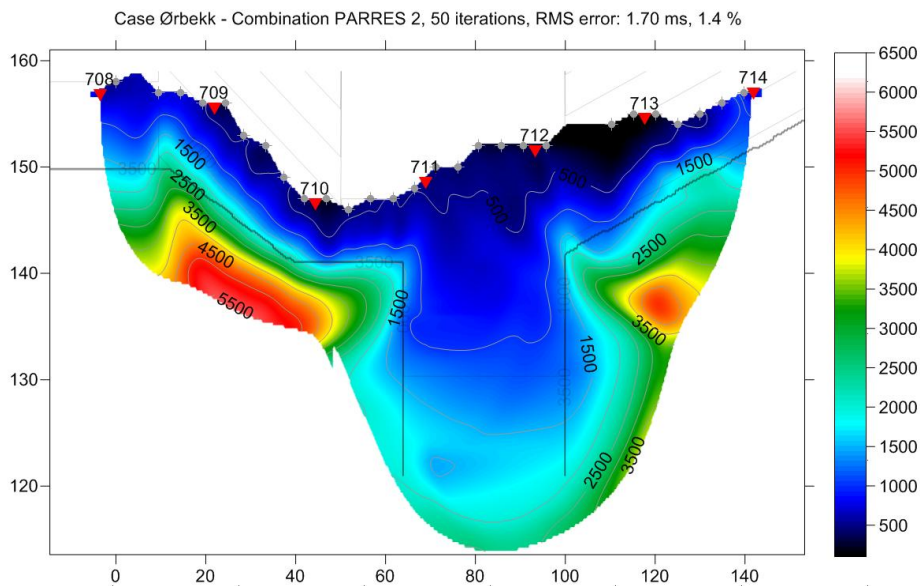


Figure 7.3: Tomogram for the inversion with parameter combination PARRES 2 applied to synthetically created traveltimes for the Ørbekk case.

Applying the findings from the previous chapter (see table 6.5) yields absolute RMS-errors as shown in table 7.1. Due to the fact that the combinations *PARRES 4* and *PARRES 6* do not give the expected results, which is an improvement of the absolute RMS-error in the order of about 30 %, inversions with the other combinations are run as well.

Comparing these results to the one obtained with default parameters shows that combinations *PARRES 1*, *PARRES 3* and *PARRES 4* increase the absolute RMS-error by 30 %, 70 % and 32 %, respectively. An improvement of 47 % for the absolute RMS-error is obtained with combination *PARRES 2*, while combinations *PARRES 6* and *PARRES 7* only give insignificant improvements of less than 1 %.

The inspection of the settings in combination *PARRES 2* shows, that they are equal to combination *PARRES 1*, except for the *Wavepath width*, which is set to 3.5 % instead of 2 %. This difference of 1.5 % results in a 59 % lower RMS-error (compared to *PARRES 1*).

These combinations are the result of an investigation on a profile with no topography and a simple syncline with a narrow opening; and applying them to a profile with topography and a different subsurface structure delivers a large discrepancy. At this point it is not possible to state whether this deviation is caused by the difference of topography or the structure of the subsurface.

For the inversion result with combination *PARRES 2* the tomogram is shown in figure 7.3. Tomograms of all inversions as well as images of their respective wavepath-coverages can be found in Appendix E.

In the following chapter, the influence of combination *PARRES 2* is tested on field data from the Ørbekk-survey.

Parameters/Settings	value/option	RMS-error
PARRES 1		
Lower velocity of 1D-gradient layer	activated	4.17 ms
Process every CMP offset	activated	
Wavepath width	2 %	
Smoothing	Minimal	
PARRES 2		
Lower velocity of 1D-gradient layer	activated	1.70 ms
Process every CMP offset	activated	
Wavepath width	3.5 %	
Smoothing	Minimal	
PARRES 3		
Lower velocity of 1D-gradient layer	activated	5.43 ms
Process every CMP offset	activated	
Interpolate velocity for 1D-gradient initial model	de-activated	
Wavepath width	2 %	
Smoothing	Minimal	
PARRES 4		
Lower velocity of 1D-gradient layer	activated	4.24 ms
Process every CMP offset	activated	
Blank below envelope after last iteration	de-activated	
Wavepath width	2 %	
Smoothing	Minimal	
PARRES 6		
Lower velocity of 1D-gradient layer	activated	3.20 ms
Process every CMP offset	activated	
Blank below envelope after last iteration	de-activated	
Filter shallow dipping wavepath artefacts from model	un-checked	
Wavepath width	2 %	
Smoothing	Minimal	
PARRES 7		
Lower velocity of 1D-gradient layer	activated	3.19 ms
Process every CMP offset	activated	
Filter shallow dipping wavepath artefacts from model	un-checked	
Wavepath width	2 %	
Smoothing	Minimal	

Table 7.1: RMS-error for combinations of options and parameters which give the best results in the parameter investigation applied to traveltimes computed from the synthetic Ørbekk-model as shown in figure 7.1. Each combination was run with 50 iterations.

Chapter 8

Ørbekk Field Data Processing

After the parameter combinations, which were found in the parameter investigation, have been verified with the synthetic data computed from a section of the Ørbekk profile, the one leading to the best result is now applied to data from the Ørbekk field survey. In the ensuing section the default tomographic image is presented. This is followed by the tomographic inversion with the derived parameter combination utilized yielding a reduction of the absolute RMS-error.

8.1 Default Settings and Parameters

Figure 8.1 displays the tomogram of the Ørbekk profile for default settings and parameters after 50 iterations. The absolute RMS-error comes to a value of 1.72 *ms* and the normalized error to 2.5 %.

The tomographic image exhibits layers and low velocity zones, as for example the one between offset 125 and 200 *m*, well. Referring to the analysis of Rønning et al. (2009), it should be mentioned that interpretations from resistivity and IP data reveal further low resistivity zones, which are only vaguely indicated in this tomogram. For example do both methods suggest a thin steep fault beneath shot point 705 extending more than 60 *m* and dipping towards north.

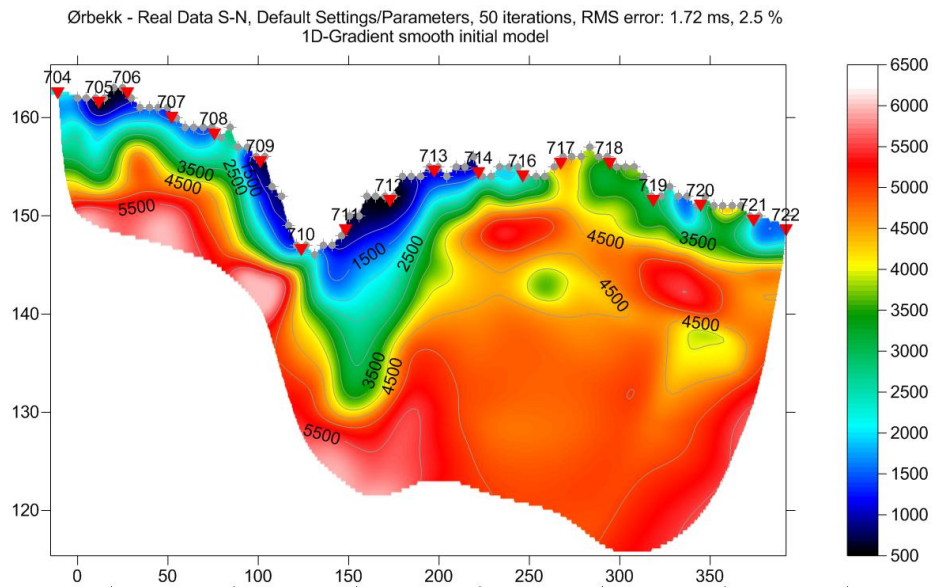


Figure 8.1: Tomogram of Ørbekk profile with data from field measurements. Default settings and parameters and 50 iterations are applied. The X-axis states the horizontal offset and the Y-axis the altitude, both in *m*.

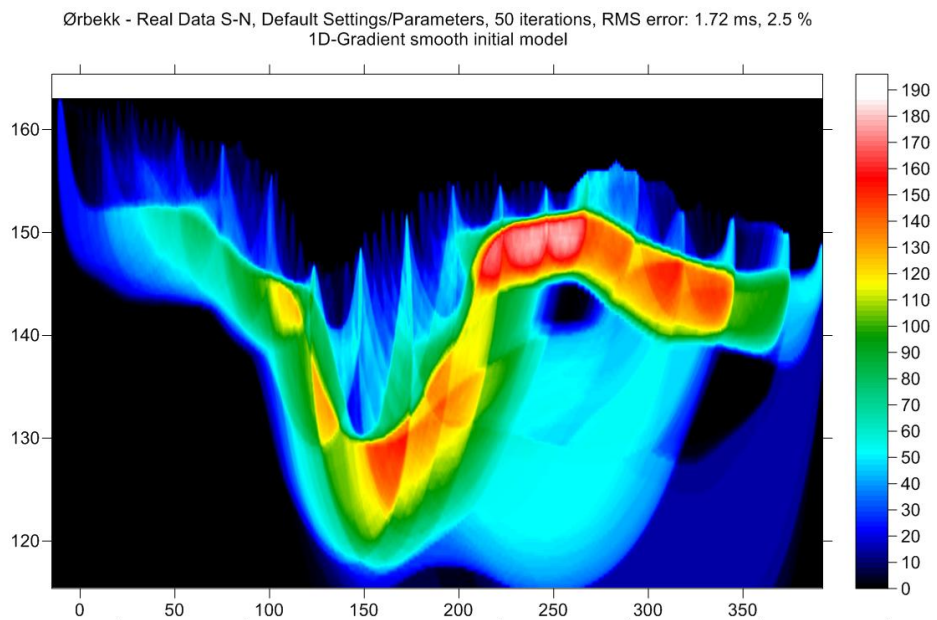


Figure 8.2: Wavepath coverage for tomogram in figure 8.1. Axes as above, the scale is in paths/pixels.

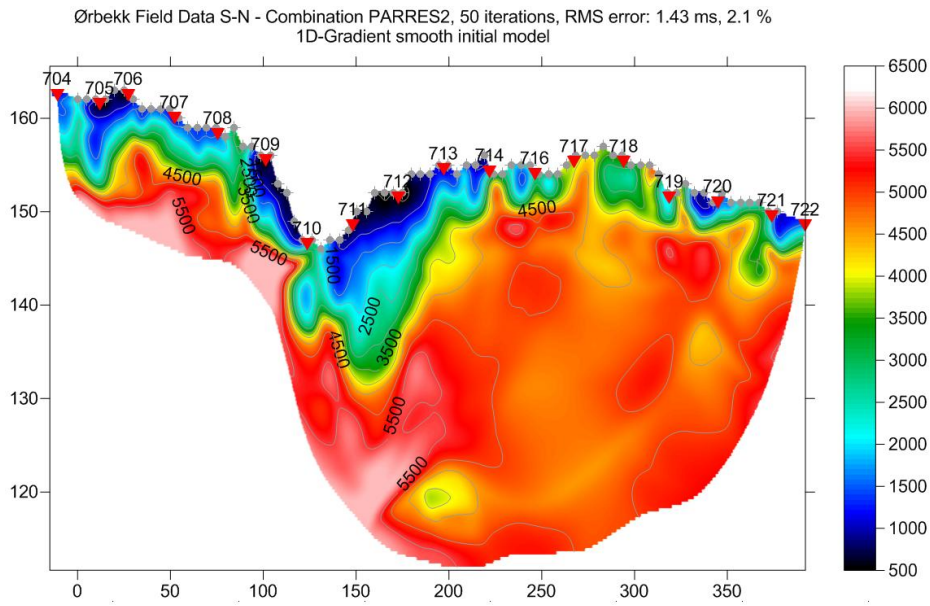


Figure 8.3: Tomogram of Ørbekk profile with field data for combination PARRES 2 and 50 WET iterations. The X-axis states the horizontal offset and the Y-axis the altitude, both in *m*.

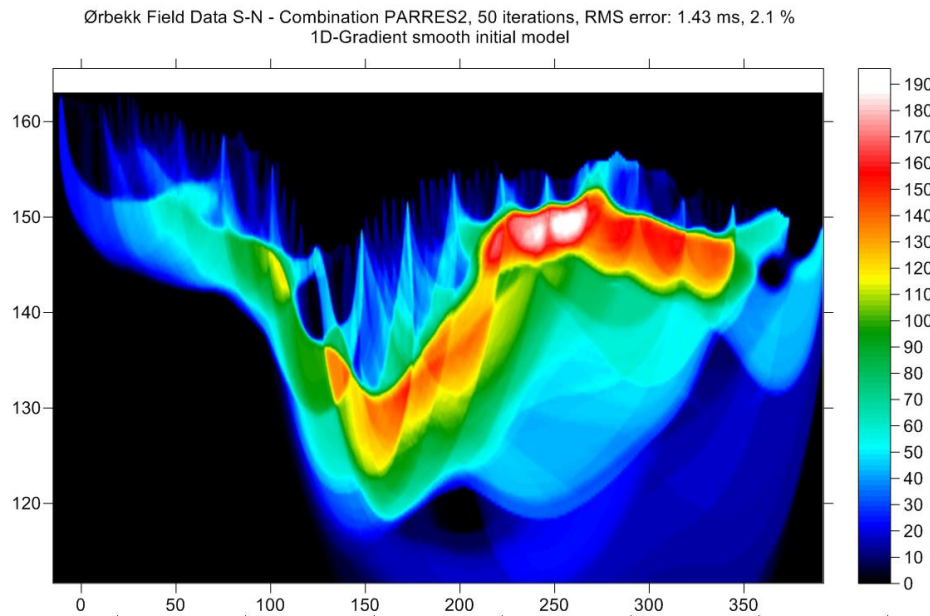


Figure 8.4: Wavepath coverage for tomogram in figure 8.3. Axes as above, the scale is in paths/pixels.

Another thin fault seems to start between shot 706 and 707 dipping towards south an intersecting with the fault beneath shot 705 about 40 *m* beneath the surface. Both are suspected to be filled with water, which is why these methods easily detect them. For the rift beneath shot 705 an indication can be observed in the tomogram, though only extended by 10 *m* below the surface.

For the interpretation of tomograms the wavepath coverages are very helpful. Areas with high coverage ensure more reliable interpretations and areas with low wavepath coverage should be treated more carefully. As seen in the wavepath coverage image in figure 8.4 are the outermost areas of the profile covered rather poorly by the wavepaths. This makes the interpretation of the low velocities below shot numbers 705, 706 and 707 more uncertain. Comparing the absolute RMS-error of 1.72 *ms* to the actual first arrival travel times shows that it corresponds to 1/12 and 1/40 of the respective average and maximum measured time.

8.2 Combinations of Best Settings and Parameters

Tomographic inversion containing the above found combination generates the tomogram depicted in figure 8.3. The absolute RMS-error of 1.43 *ms*, 2.1 % for the normalized error, reduces the default by 0.29 *ms*, corresponding to 17 %; the normalized error is lowered by 0.4 %.

More details are revealed in this tomogram. For example beneath shot point 705 and 706 is a low velocity zone much more pronounced than in figure 8.1, but also here its extension stops 10 *m* below the surface. As before, the wavepath coverage is very low and therefore, this interpretation is very uncertain.

The broad velocity zone between offset 130 and 200 *m* is modelled similarly to figure 8.1; a detail on the left side of it, at 140 *m* altitude is added. This might be caused by low wavepath coverage in this area.

Between offset 200 and 390 *m* more details are revealed as well, as for example a low velocity zone beneath shot number 721. This zone is not interpreted by

the resistivity data (see Rønning et al. (2009)), but also here low wavepath coverage might cause this modelling.

Wavepath coverages in figures 8.3 and 8.4 differ from each other. Some areas are covered better with *PARRES 2*-parameters applied (i.e. at offset 250 *m* and 145 *m* altitude as well as between offset 300 and 350 *m* and 130 to 140 *m* altitude) and others worse (i.e at offset 110 *m* with altitude 140 *m* and the area beyond 340 *m* offset).

Whether the tomographic image obtained with combination *PARRES 2* or with default settings is best suited for interpretation can not be determined here. RMS-errors as low as possible and an increased amount of details have been achieved, but in order to decide whether these features contribute to more reliable interpretations a better knowledge of the real subsurface condition is required.

As the wavepath coverage changes with different settings and parameters several tomograms, obtained with different sets of parameters, would supplement each other. By this both better wavepath coverages and more details open up for more certain interpretations.

Chapter 9

Sources of Uncertainties

First arrival traveltimes are assumed by the algorithm to be perfectly accurate measurements. Therefore no uncertainty of traveltimes is included in the computations.

For the synthetically created traveltimes the forward algorithm (section 4.1.1), which computes these times, is the only source of uncertainties, but these uncertainties are negligible and can be ignored.

The largest uncertainties are therefore generated by the inversion code. For example, the code can obtain a good agreement between modelled and measured traveltimes, but still, the modelled wavepaths can be very different from the actual ones. Another factor for modelling uncertainties is the non-uniqueness of the solution.

When working with field data, the uncertainty of the inversion algorithm is accumulated by real factors. Factors contributing to timing errors, and not taken into account by the algorithm, are i.e. (Olaya and Romero, 2009):

- Seismic noise: *The first arrival might be drowned in noise and therefore it is not possible to pick the moment of the signal arrival. Errorneously the arrival of the second maximum can be chosen.*
- Picking first arrivals is a matter of the operator's experience and preferences.

- The size of the source: *This is related to the first item. A stronger source results into a better signal-to-noise ratio. Seismic noise becomes less of a problem.*
- Instrument errors
- Topographic errors like station offsets, source-receiver distances.

Furthermore human errors could contribute to uncertainties. For the processing of traveltimes and the interpretation of seismic tomograms the possible impact of these uncertainties should be considered.

One possibility for decreasing modelling uncertainties is the increase of data density, which is obtained by closer shot and receiver spacings.

Chapter 10

Conclusion and Prospects

Conclusion

In this thesis the tomographic inversion tool Rayfract has been examined with the aim of determining settings and parameters for obtaining an increased velocity contrast compared to tomograms created earlier.

Synthetic models form the basis for this investigation. First arrival travel-times are created from these models and used as input data for the tomographic inversions. By using synthetic data, the outcome, the inversion is supposed to model, is known and can directly be compared to the model.

Initially the program's ability to recognize anomalies of different shapes, dimensions, velocities, and locations in the subsurface has been examined. High shot and receiver coverage as well as a sparse coverage, according to a field set-up, have been tested.

From these investigations it can be concluded that the code is able to recognize most of them. For locations in the range of the rays and dimensions of only $2 \times 2 \text{ m}^2$, the code has no problems to model them, neither with high nor for sparse data coverage. Anomalies with a contrast of 1 to the surroundings are modelled with high coverage data, but not with the low coverage data. Anomalies with lower velocity than their surroundings are discovered as well, but their velocities are modelled to be larger than the

surroundings.

From these models one model, which corresponds to real geological conditions, was chosen for the parameter investigation.

All relevant settings and parameters have been explored one by one. The ones, which led to a reduced absolute RMS-error, have been used in different combination set-ups leading to the set-up with the lowest error. Here two combinations (*PARRES 4* and *PARRES 6*) led to equally low RMS-errors improving the reference inversion by about 30 % after 50 iterations and 54 % after 250 iterations.

Applying these combinations to a model resembling a condition from a real profile resulted in unexpected RMS-errors. While combination *PARRES 6* gave an improvement of less than 1 %, worsened combination *PARRES 4* it by 32 %.

Inversions with the combinations *PARRES 1* and *PARRES 3* increased the absolute RMS-error by 30 % and 70 %, respectively. Applying the combination *PARRES 7* and *PARRES 2* improved the RMS-error by less than 1 % and by 47 %, respectively.

Verifying this combination (*PARRES 2*) with field data led to an error improvement of about 17 %.

Main conclusions for this work are:

- Parameter investigation were carried out with the initial model created with *Smooth Inversion* only. Inversions performed with initial models created with *Delta-t-V Inversion* (in pre-studies) showed very unstable behaviour. This agrees well with the code supplier statement that this inversion method can cause artefacts. RMS-error improving parameters and settings led to two combinations, which both yield an improvement of about 30 % after 50 iterations and about 54 % after 250 iterations.
- The settings and parameters, which perform well for one profile do not necessarily have the same effect on another profile. As shown in this work did the parameter combinations *PARRES 4* and *PARRES 6* not have the same positive affect on the synthetic model for Ørbekk as for the reference model Ub. On the other hand gave the combination *PARRES 2* a much better result than expected.

- The code models velocity gradients, also for heterogeneous anomalies. This might result in too high modelled velocities for the overburden and too low for the refractor at the layer boundary.
- The two *Interactive WET Tomography* parameters *Wavepath width* with a value of 2 % and *Minimal Smoothing* appear in all combinations for the lowest RMS-error. These parameters bear the largest part of lowering the RMS-error and will most likely work for inversions of all kind of data. Activation or deactivation of certain settings can generate further improvements depending on surface and subsurface conditions.
- A lower or minimized RMS-error is not synonymous with a better tomographic image. An enhancement of details, which not necessarily are true, can make it difficult to interpret the outcome.
- Furthermore does a lower RMS-error not lead to an increased velocity contrast as shown in figure 6.6. Nevertheless can the tomographic images be improved by means of better visibility of anomalies in the subsurface. For example can an increase of iterations improve the WET Tomography output while the (normalized) RMS-error is not changed (Rohdewald, 2010).
- The use of wavepath coverage images together with the tomographic images strengthens the quality of the interpretations. Several tomographic images, obtained with different parameters and settings, complement each other with respect to wavepath coverage and the amount of details. This contributes to a more certain interpretation of the subsurface.

Summarizing these findings, it can be stated that, except for the two WET parameters *Smoothing* and *Wavepath width*, a general set-up valid for all kinds of profiles can not be given. Basically, the default settings deliver an acceptable tomographic image, and by applying the above mentioned parameters, the RMS-error decreases and more details are revealed, but it can be discussed whether these details are more realistic.

Prospects

The used code has been examined thoroughly with respect to its sensitivity and with respect to the best parameters and settings for the synthetic model Ub. A significant improvement of the RMS-error has been achieved. Obviously do the settings and parameters not have the same impact on different profile conditions, both surface and subsurface conditions.

For future work the following points could be of interest:

- For profiles with no topography some options and parameters do have a positive impact on the RMS-error as shown in chapter 6. A parameter investigation for subsurfaces, which often occur in reality, could lead to set-ups yielding lower inversion errors.
- Profiles with topography respond differently to certain parameters than profiles without topography. A parameter investigation for profiles with topographies, which occur frequently in reality, could be conducted as well.
- From experience a large knowledge of the most occurring subsurface structures exist. For these structures a model catalogue as guide for how to interpret the modelled images could be composed. Of course, this catalogue should take the code's weaknesses, too high overburden velocity and too low refractor velocity at the layer intersection, into account and guide the interpreter to an interpretation closer to the real conditions. For improving the subsurface interpretation the seismic measurements could be supplemented with crosshole and/or VSP (Vertical Seismic Profile) surveys.
- Tomographic inversions with Rayfract could be compared to inversion results of other tomography-tools. Sheehan et al. (2005) have carried out such a work with Rayfract, GeoCT (GeoTomo, LLC) and SeisImager/2D (OYO). Nevertheless, as this investigation has been conducted 5 years ago and with Rayfract's version 2.51, it would be worth the effort to make a new evaluation with a newer version of Rayfract (as i.e. today's version 3.18).

Appendix A

Eikonal solver by Vidale

In section 4.1.1 the by the code used forward modelling algorithm, which calculates the traveltimes of the fastest wave at any point of a regular grid, developed by Podvin and Lecomte (1991) has been discussed. The basis for their work is the proposed method by Vidale (1988) where the Eikonal equation is solved by using finite differences. Here his method is shortly presented.

Traveltimes are calculated within regular grids where the traveltimes at three out of four corners are known and the fourth (see figure A.1a) is found by using the following equation:

$$t_P = t_M \pm \sqrt{2(hs)^2 - (t_N - t_O)^2} \quad (\text{A.0.1})$$

with h the length of the sides of the square cell. This equation is only exact, if the traveltimes t_M , t_N and t_O are associated with a locally plane wavefront. The sign of the square root is undetermined because the Eikonal equation gives only the modulus of the slowness vector and not its direction. In order for the sign to be determined an expanding square ring (figure A.1b) is introduced with the shotpoint in its centre. Traveltimes on the current ring are calculated by using traveltimes from the previous ring, following a minimum-to-maximum traveltime progression. In case of being in front of a minimum another finite-difference estimation of the Eikonal equation is applied:

$$t_P = t_M + \sqrt{(h\tilde{s})^2 - 0.25(t_N - t_O)^2}, \quad (\text{A.0.2})$$

where \tilde{s} is the mean of the slownesses of the two neighbouring cells (figure A.1c). Gridpoints on the current ring in front of a maximum will be assigned to traveltimes, where the minimum time is chosen, which is characteristic for Eikonal solvers (provide only the fastest arrival). The estimated traveltime calculated at the fourth point may be associated with supercritical incidence with respect to the slownesses of the two adjacent cells. The traveltimes for the adjacent cells will give a negative argument under the square root and hence an imaginary term. Vidale (1988) chose to ignore the imaginary term and set the traveltime at the fourth point, t_P , equal to t_M in order to avoid holes in the traveltime grid. This causes incorrect traveltimes.

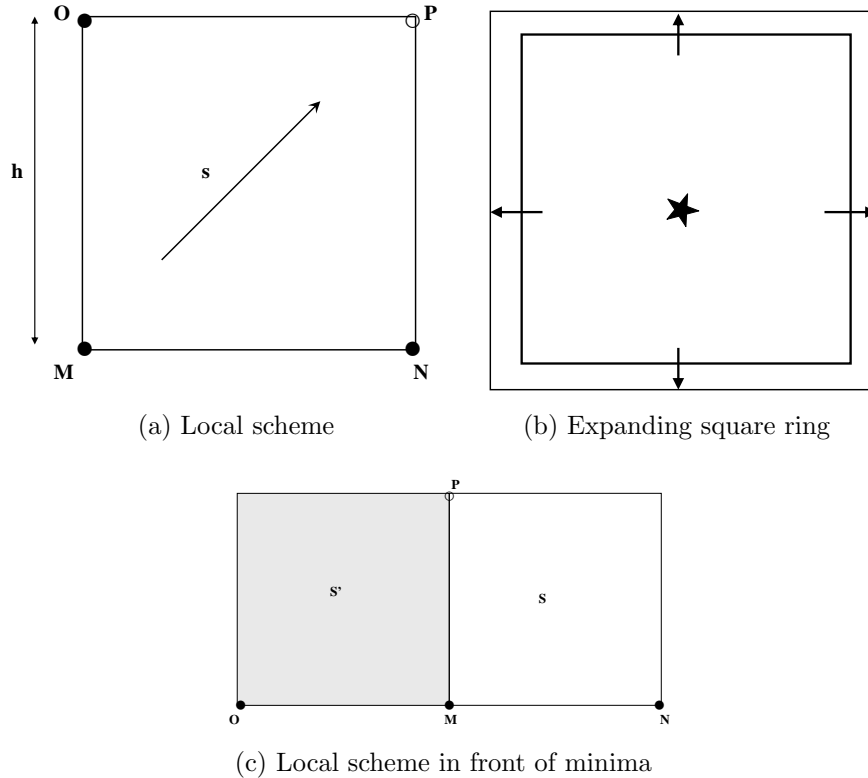


Figure A.1: The original method of Vidale (1988). (a) The local scheme: the traveltime at three corners (**M**, **N**, **O**) of a cell are used to estimate the traveltime at the fourth corner (**P**). (b) The expanding square ring process: the initial stage is the emission time at a source point on a regular grid (star). Thereafter, traveltimes are determined along successive square rings centred at the source, using traveltimes on the previous ring. (c) Local scheme in front of traveltime minima. From (Lecomte et al., 2000)

Appendix B

Refractor-imaging principle

A refractor imaging principle, also called *Plus-Minus method*, developed by Hagedoorn (1959), is shortly discussed in this section. Figure B.1 illustrates this principle. For this method it is a requirement that the shot points F (shot) and R (re-shot) have a distance such that the refracted wavefronts are first arrivals at the surface. Its limitation lies in the fact, that boundaries (refractors) have to be flat and the velocities of the layers constant. Having these requirements fulfilled leads to the possibility of simple geometric solutions. Wavefronts from shot and re-shot intersecting at time intervals, δ ms, form a quite regular pattern. This pattern consists of diamond-shaped figures as illustrated in figure B.1.

The horizontal and vertical diagonals of the the diamonds are equal to $v_2\delta$ and $v_1\delta/\cos\theta_c$, respectively. Adding shot and re-shot traveltimes at each intersection and subtracting the traveltime between the two shot-points (equal for both directions) results in a *plus* value which equals 0 on the refractor, $+2\delta$ on the horizontal line through the first set of intersections vertically above the refractor, $+4\delta$ on the next line, and so on. As the distance between each pair of adjacent lines is $v_1\delta/\cos\theta_c$, any plus line can be used to plot the refractor.

Subtracting the two traveltimes at an intersection gives the *minus* value. This value is constant along vertical lines passing through the intersections of wavefronts. Successive minus lines have at distance of $v_2\delta$ which enables a continuous check on v_2 .

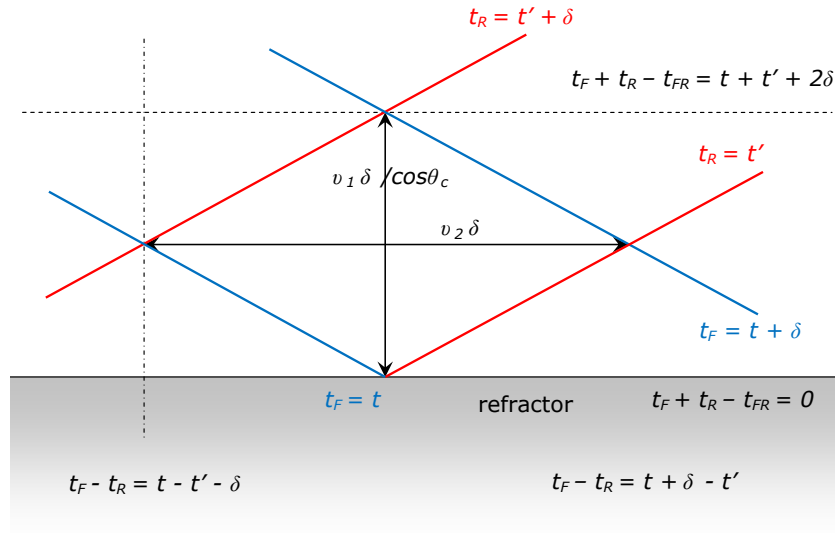


Figure B.1: Illustration of the Plus-Minus method by Hagedoorn (1959). Blue lines are wavefronts from forward shot, F , and red lines from reverse shot, R , δ is the time interval for forward and reverse shot intersection, θ_c the critical angle, v_1 and v_2 the velocity of the overburden and refractor respectively.

As mentioned above, this procedure is only valid for horizontal refractors, but for moderate dips only small changes are found and it is assumed that the *plus lines* are still parallel to the refractor and the *minus lines* do not converge or diverge (Telford et al., 2004).

Appendix C

Sensitivity Investigation

C.1 Synthetic Models

In this chapter all synthetic models and their tomographic images for the sensitivity investigation are illustrated. All investigations were conducted with high receiver and shot density (a-figures) and one low density (b-figures). Station spacing for all set-ups is 5 *m*. Unless otherwise stated, the velocity gradient of the upper layer is 1000 *m/s* at the surface and increasing with 50 *m/s* per *m*, and the anomaly has a constant velocity of 5000 *m/s*. All tomographic inversion were run with 50 iterations. The X-axis depicts the distance (offset) and the Y-axis the elevation, both in metres. Grey dots mark the receiver stations and red triangles the shot points.

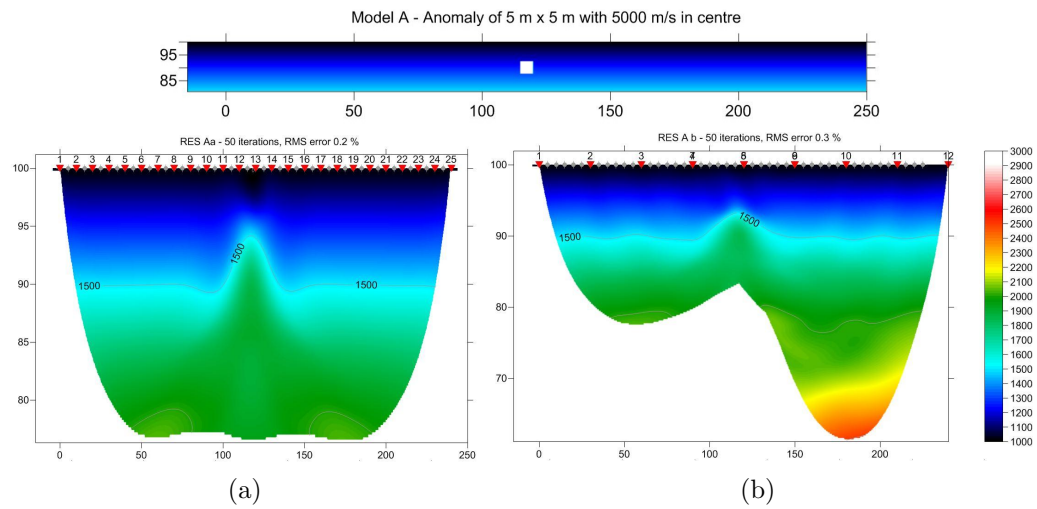


Figure C.1: Model A: The anomaly of the dimension $5\text{ m} \times 5\text{ m}$ is located in the centre of the area of interest. Figure (a): high density data with 48 geophones and 25 shots. Figure (b): low density with 2×24 geophones and 2×6 shots. Both cases recognize the anomaly, but not its much higher velocity. Furthermore it is extended upwards and downwards in both cases.

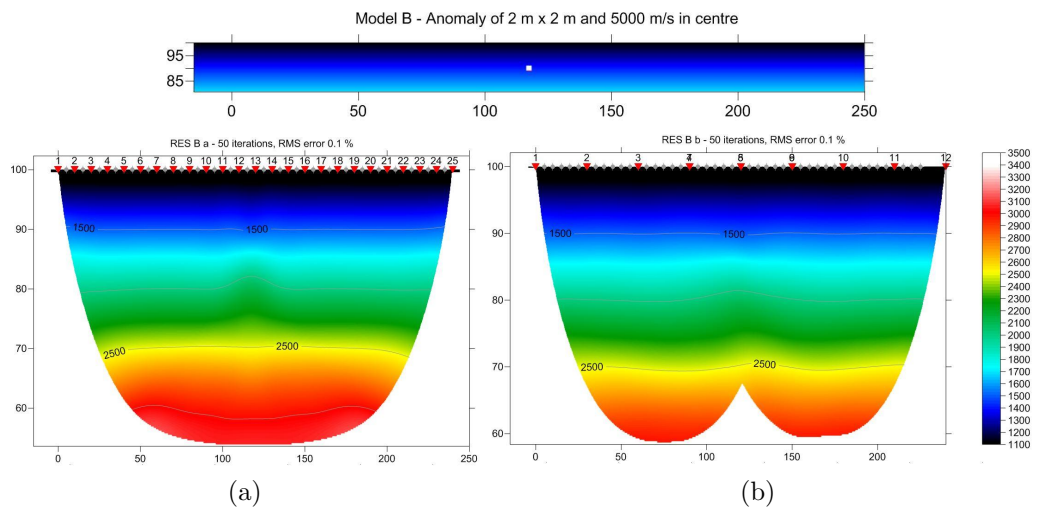


Figure C.2: Model B: The anomaly of dimension $2\text{ m} \times 2\text{ m}$ is located in the centre of the area of interest. Figure (a): high density data with 48 geophones and 25 shots. Figure (b): low density with 2×24 geophones and 2×6 shots. Both cases recognize the anomaly, though a bit vague for the low density case. As above the modelled velocity is lower, but the extension is only directed downwards.

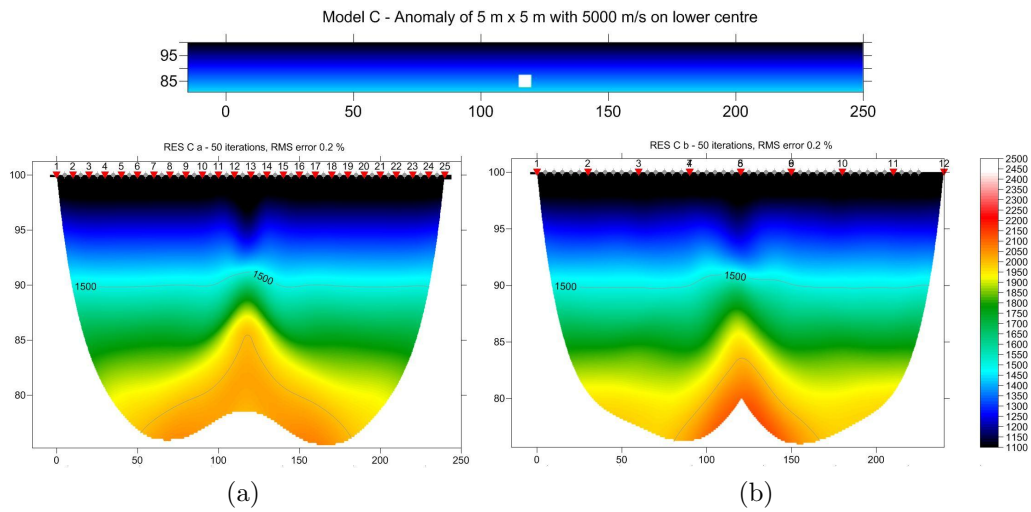


Figure C.3: Model C: The anomaly of dimension $5\text{ m} \times 5\text{ m}$ is located in the lower centre of the area of interest. Figure (a): high density data with 48 geophones and 25 shots. Figure (b): low density with 2×24 geophones and 2×6 shots. Both cases recognize the anomaly clearly; in the case with lower density it is even located a little bit deeper and therefore closer to its true location. Also here both cases extend the anomaly downwards.

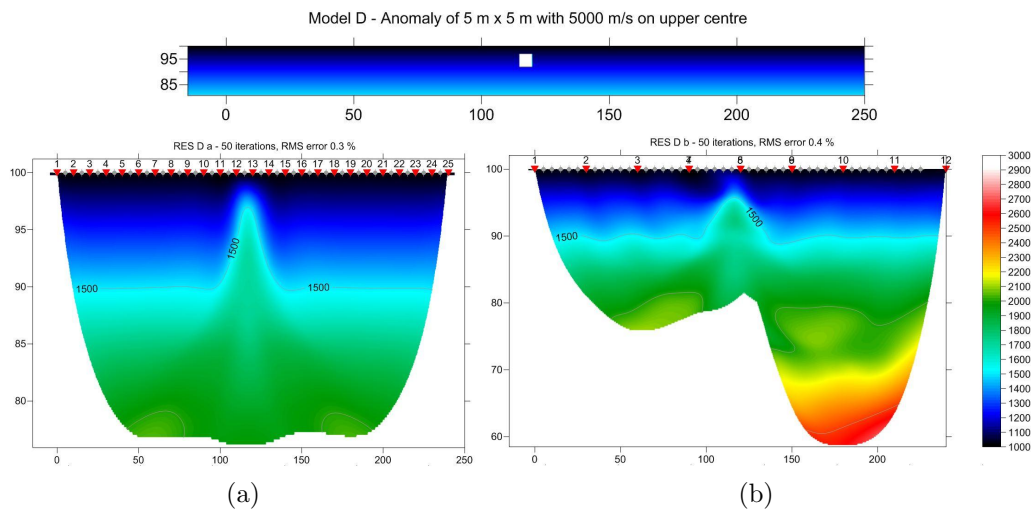


Figure C.4: Model D: The anomaly of the dimension $5\text{ m} \times 5\text{ m}$ is located in the upper centre of the area of interest. Figure (a): high density data with 48 geophones and 25 shots. Figure (b): low density with 2×24 geophones and 2×6 shots. Both cases recognize the anomaly clearly at its true position and extend it towards the bottom. The low density case models an anomaly of larger dimensions.

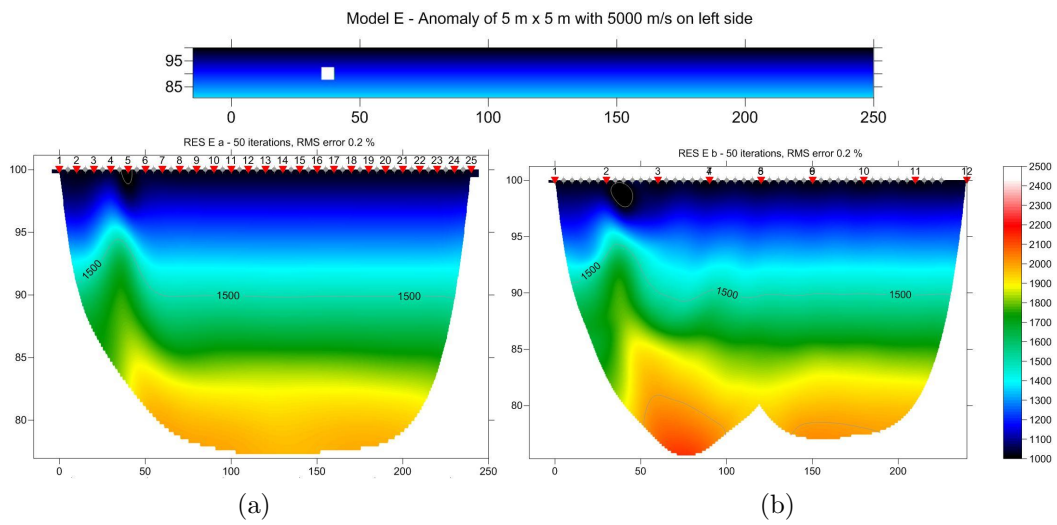


Figure C.5: Model E: The anomaly of the dimension $5\text{ m} \times 5\text{ m}$ is located on the left side of the middle of the area of interest. Figure (a): high density data with 48 geophones and 25 shots. Figure (b): low density with 2×24 geophones and 2×6 shots. Both cases recognize the anomaly clearly and extend it downwards.

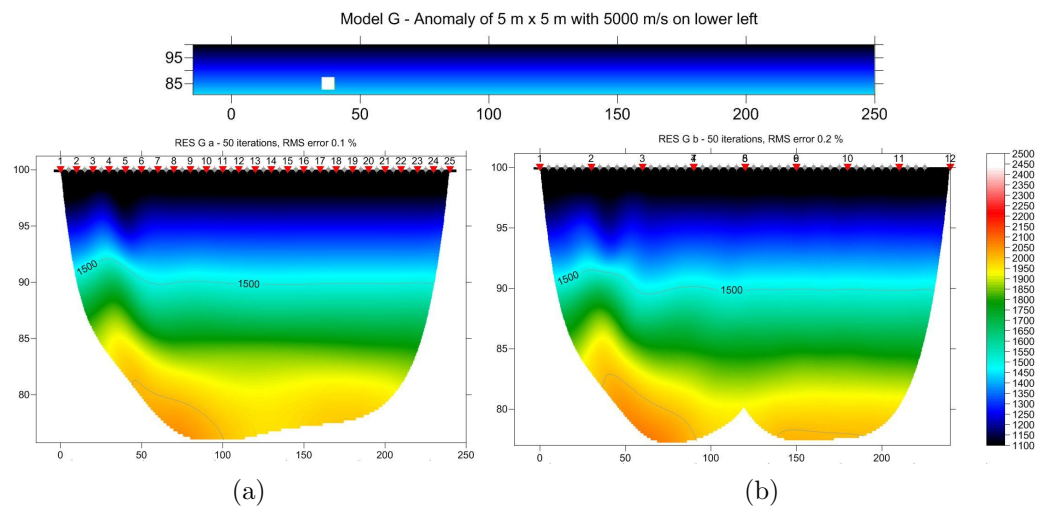


Figure C.6: Model G: The anomaly of the dimension $5\text{ m} \times 5\text{ m}$ is located on the lower left side of the area of interest. Figure (a): high density data with 48 geophones and 25 shots. Figure (b): low density with 2×24 geophones and 2×6 shots. Both cases recognize the anomaly clearly at its true position and extend it towards the bottom.

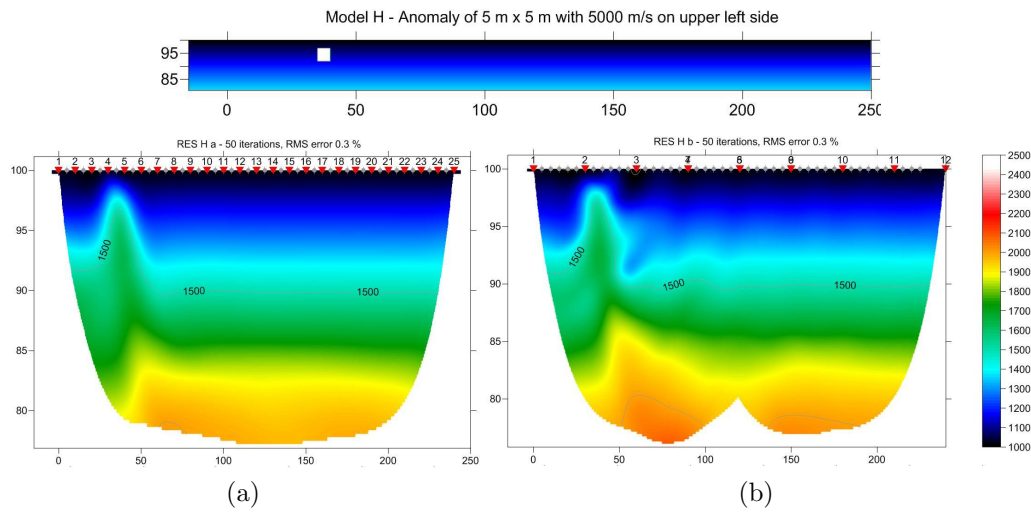


Figure C.7: Model H: The anomaly of the dimension $5\text{ m} \times 5\text{ m}$ is located in the upper left side of the area of interest. Figure (a): high density data with 48 geophones and 25 shots. Figure (b): low density with 2×24 geophones and 2×6 shots. Both cases recognize the anomaly clearly at its true position and extend it towards the bottom. The low coverage case adds a low velocity zone to the right of the anomaly.

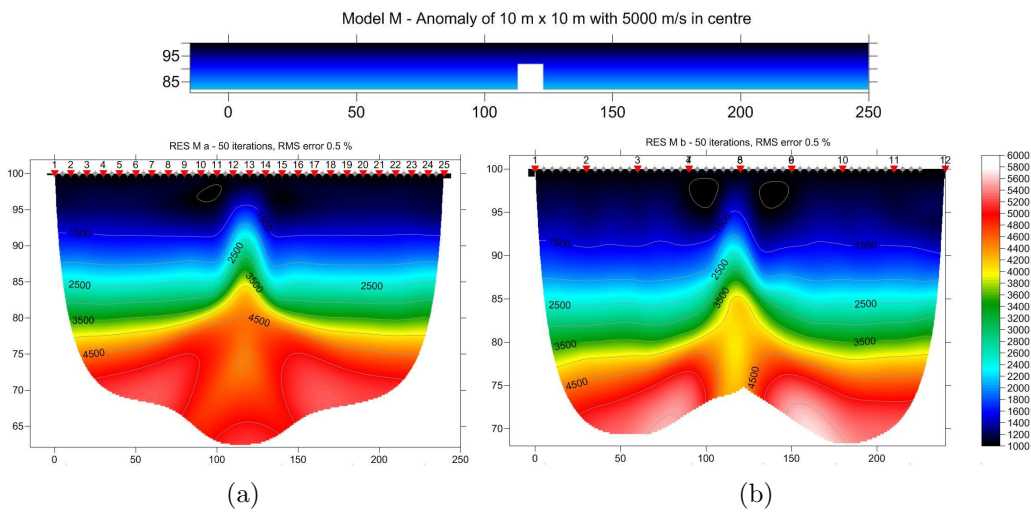


Figure C.8: Model M: The anomaly corresponds to a very steep anticline of $10\text{ m} \times 10\text{ m}$ in the lower centre extending from the refractor. Figure (a): high density data with 48 geophones and 25 shots. Figure (b): low density with 2×24 geophones and 2×6 shots. Both cases recognize the anomaly clearly at the real position; the low coverage case models a velocity zone of 4000 m/s continuing towards the bottom of the image.

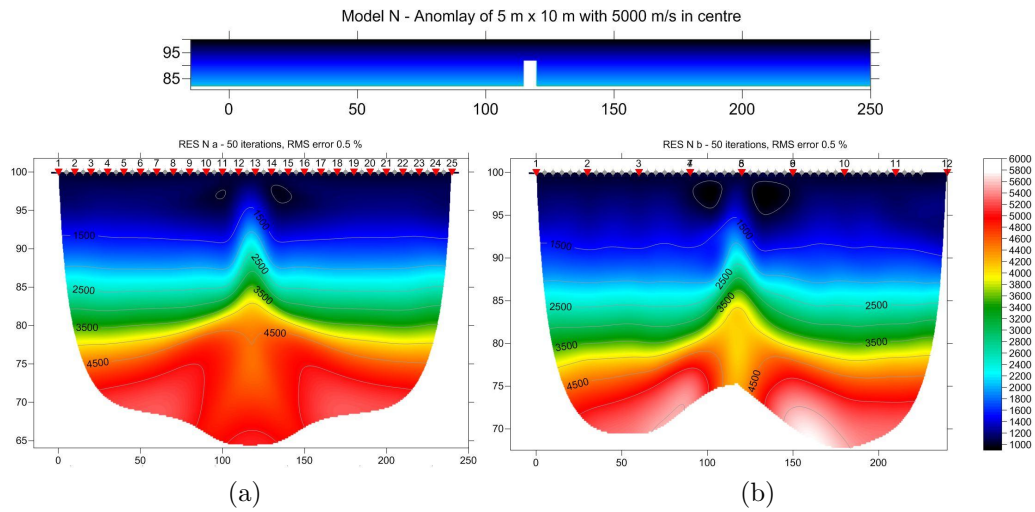


Figure C.9: Model N: The anomaly corresponds to a very steep anticline of 5 m width and 10 m in height in the lower center connected to the refractor. Figure (a): high density data with 48 geophones and 25 shots. Figure (b): low density with 2×24 geophones and 2×6 shots. Both cases recognize the anomaly clearly at its real position; also here models the low coverage case a continuing lower velocity towards the bottom.

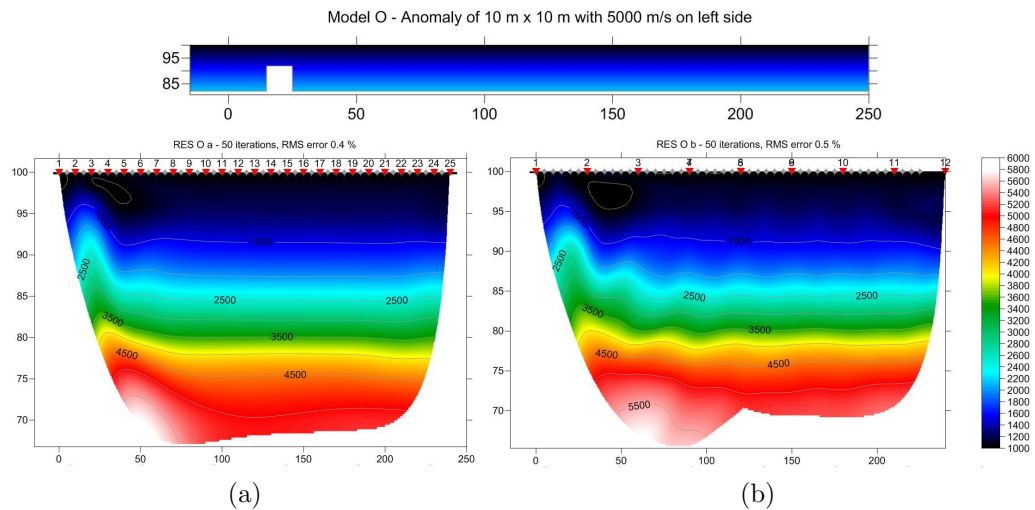


Figure C.10: Model O: The anomaly corresponds to a very steep anticline of 10 m x 10 m in the lower left connected to the refractor. Figure (a): high density data with 48 geophones and 25 shots. Figure (b): low density with 2×24 geophones and 2×6 shots. Both cases recognize the anomaly clearly at its true position.

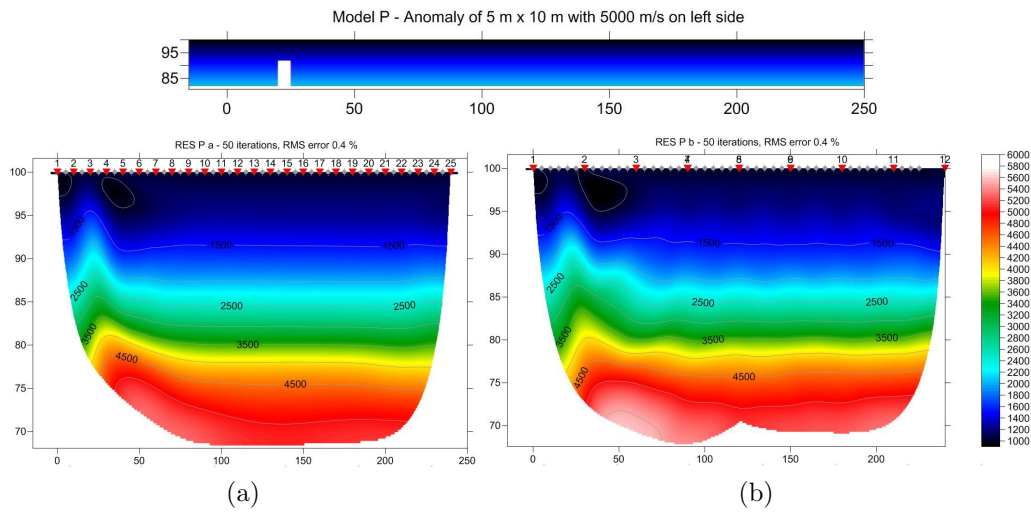


Figure C.11: Model P: The anomaly corresponds to a very steep anticline of 5 m width and 10 m in height in the lower left and is connected to the refractor. Figure (a): high density data with 48 geophones and 25 shots. Figure (b): low density with 2×24 geophones and 2×6 shots. Both cases recognize the anomaly clearly at its true position.

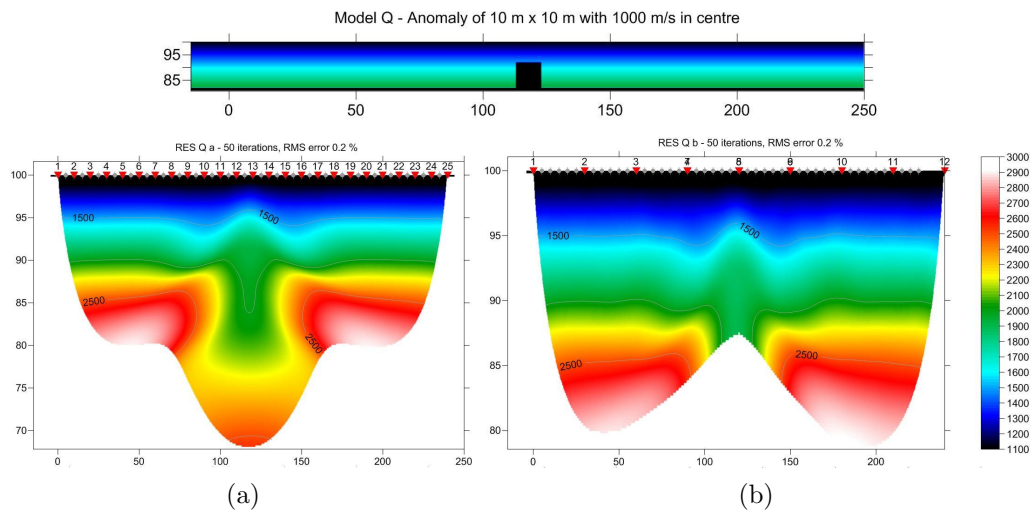


Figure C.12: Model Q: The anomaly with a velocity of 1000 m/s corresponds to a very steep anticline of 10 m x 10 m in the lower centre and is connected to the refractor with the same velocity. Figure (a): high density data with 48 geophones and 25 shots. Figure (b): low density with 2×24 geophones and 2×6 shots. Both cases recognize the anomaly but not the lower velocity. The lower velocity is modelled towards the bottom though this does not exist.

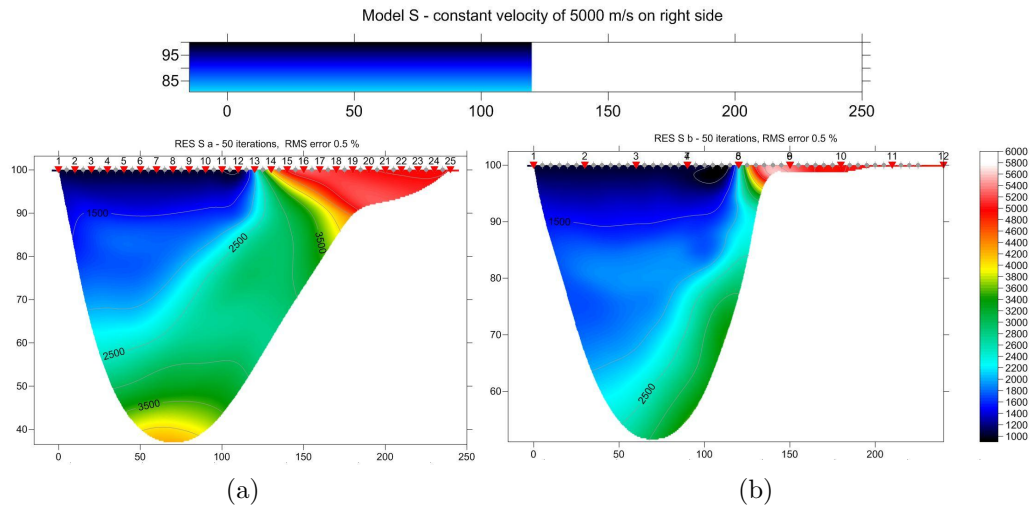


Figure C.13: Model S: Area is divided into two parts with a velocity gradient (as stated in the text above) on the left and a constant anomaly of 5000 m/s on the right. Figure (a): high density data with 48 geophones and 25 shots. Figure (b): low density with 2×24 geophones and 2×6 shots. Both inversions model this set-up though with a tilting partition wall, which is steeper for the low coverage case.

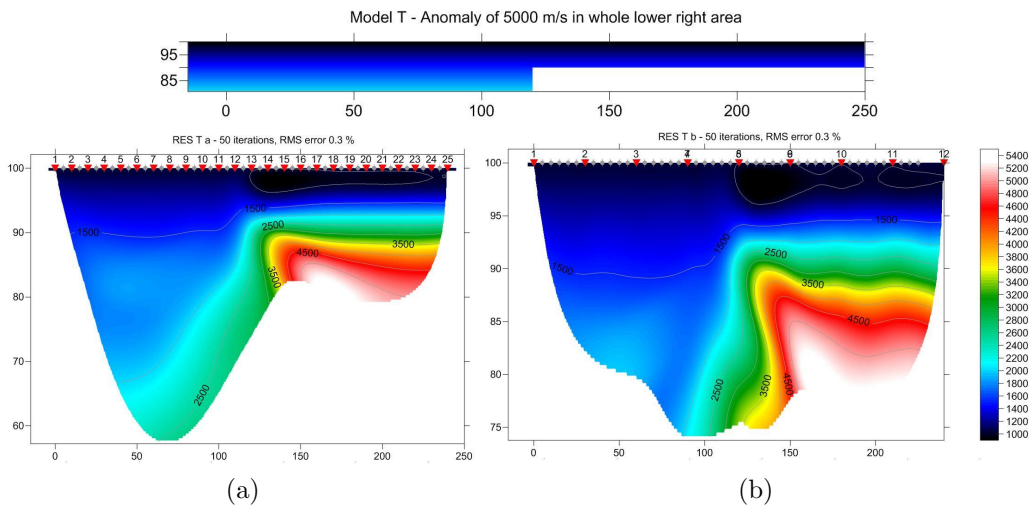


Figure C.14: Model T: The anomaly occupies the whole lower right area within the area of interest. Figure (a): high density data with 48 geophones and 25 shots. Figure (b): low density with 2×24 geophones and 2×6 shots. Both inversions are able to model this set-up quite precisely.

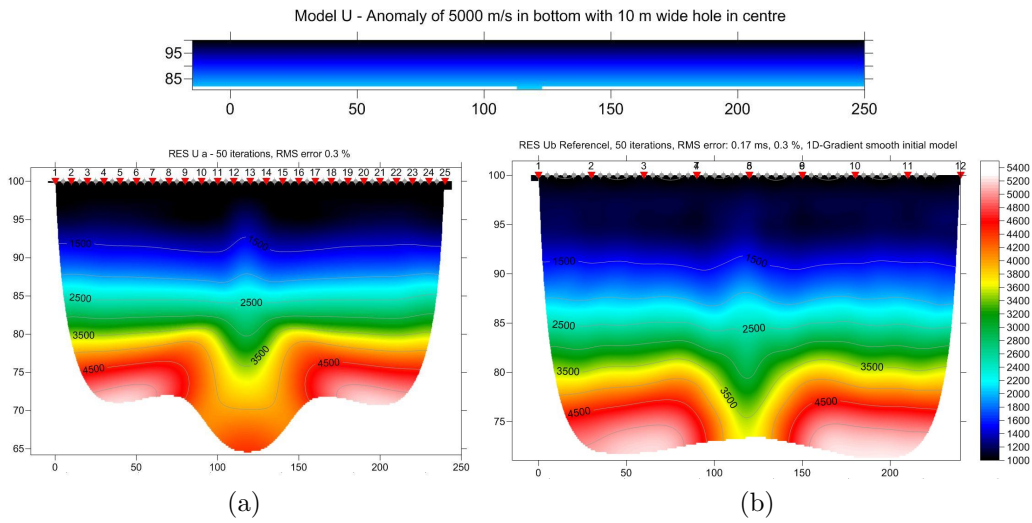


Figure C.15: Model U: The anomaly-layer below the upper layer is interrupted by a 10 m wide steep syncline with the upper velocity gradient penetrating into the refractor. Figure (a): high density data with 48 geophones and 25 shots. Figure (b): low density with 2×24 geophones and 2×6 shots. Both inversions model this set-up and add a small bump right above the syncline with slightly higher velocity than the overburden.

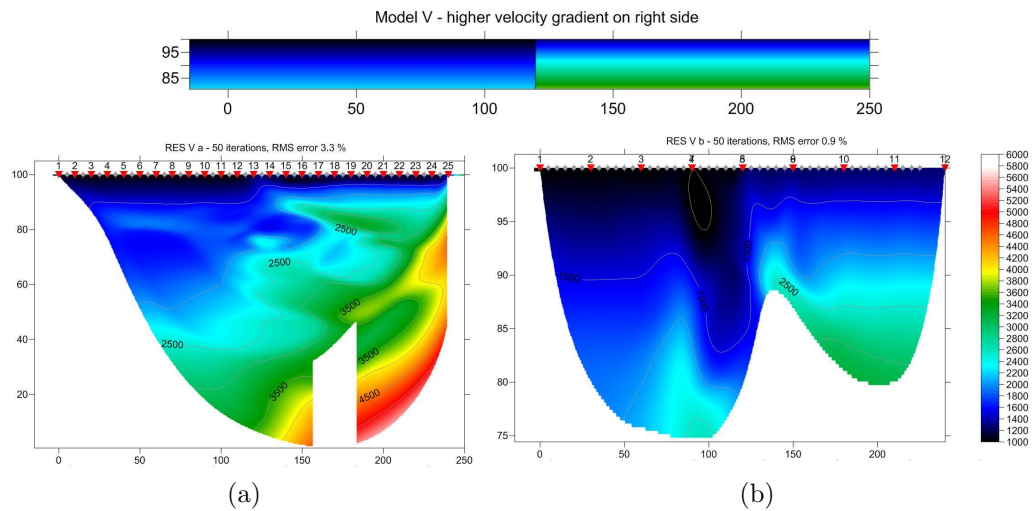


Figure C.16: Model V: Area is divided into two parts with a velocity gradient (as stated in the text above) on the left and a higher velocity gradient on the right. Figure (a): high density data with 48 geophones and 25 shots. Figure (b): low density with 2×24 geophones and 2×6 shots. Both inversions model the larger gradient on the right and only considering the area down to an elevation of 75 m reveals no big difference between the two inversions. The white area in figure (a) is caused by low wavepath coverage. Increase of wavepath width would smooth this image more. Furthermore can the algorithm for determining the wavepath envelope at the bottom of the tomogram cause this as this algorithm is not fail save (Rohdewald, 2010).

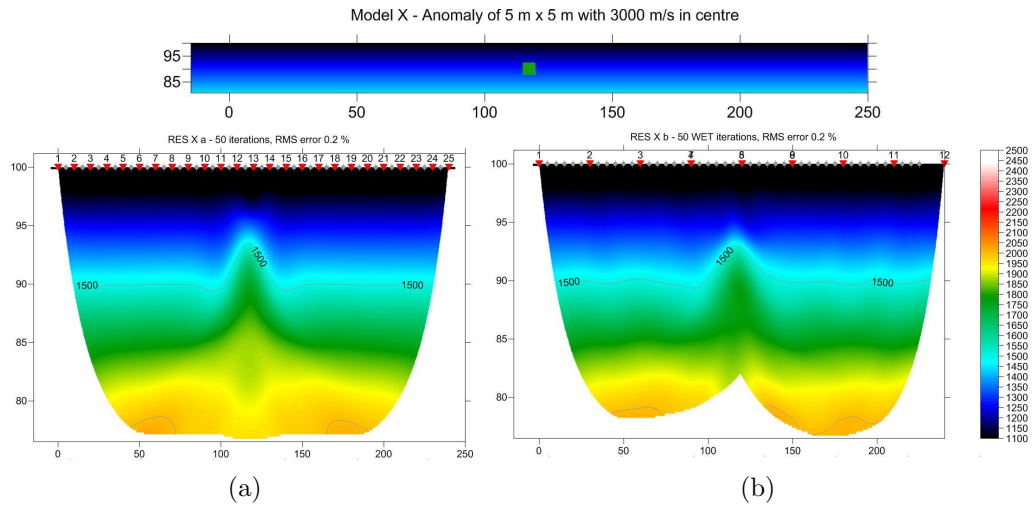


Figure C.17: Model X: The anomaly of the dimension $5\text{ m} \times 5\text{ m}$ and 3000 m/s velocity (contrast of 2) is located in the centre of the area of interest. Figure (a): high density data with 48 geophones and 25 shots. Figure (b): low density with 2×24 geophones and 2×6 shots. Both inversions localize the anomaly and model it with a lower velocity at higher altitude.

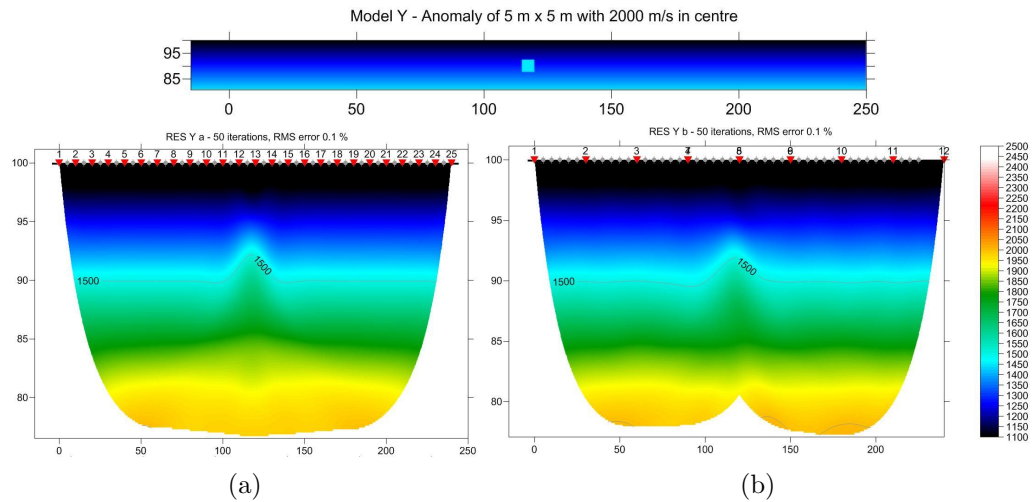


Figure C.18: Model Y: The anomaly of the dimension $5\text{ m} \times 5\text{ m}$ and 2000 m/s velocity (contrast of 1.33) is located in the centre of the area of interest. Figure (a): high density data with 48 geophones and 25 shots. Figure (b): low density with 2×24 geophones and 2×6 shots. Both inversions localize the anomaly and model it at higher altitude.

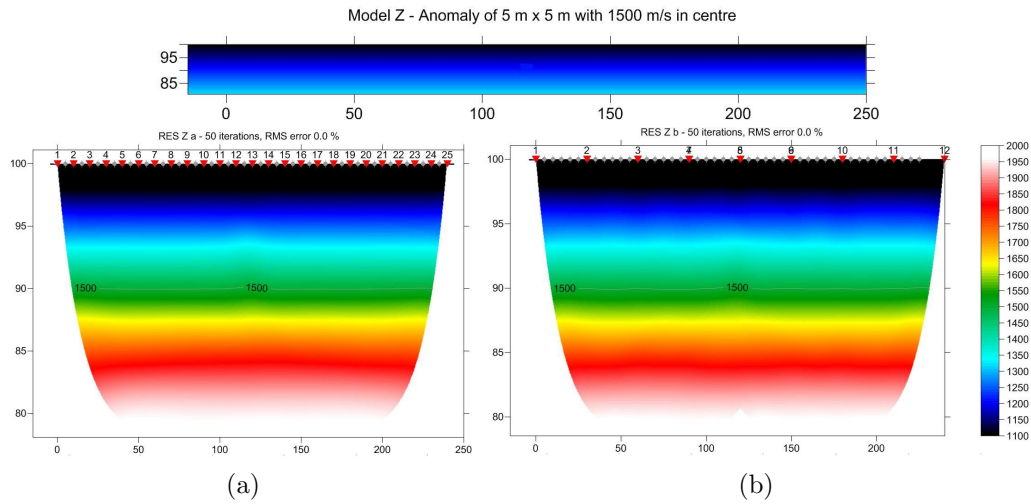


Figure C.19: Model Z: The anomaly of the dimension $5\text{ m} \times 5\text{ m}$ and 1500 m/s velocity (contrast of 1) is located in the centre of the area of interest. Figure (a): high density data with 48 geophones and 25 shots. Figure (b): low density with 2×24 geophones and 2×6 shots. The high density case lets one suspect a weak anomaly but not the low density case.

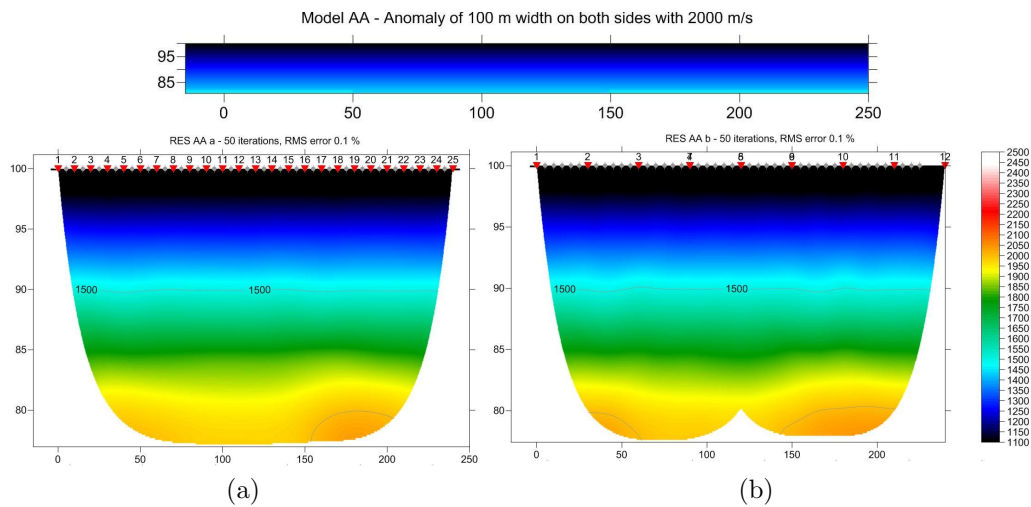


Figure C.20: Model AA: The anomaly with a velocity of 2000 m/s is located on the bottom left and right leaving an opening of 100 m in the centre. Resulting contrast is 1.2. Figure (a): high density data with 48 geophones and 25 shots. Figure (b): low density with 2×24 geophones and 2×6 shots. In both cases only the reddish areas on the left and right bottom of the tomograms reveal this set-up weakly.

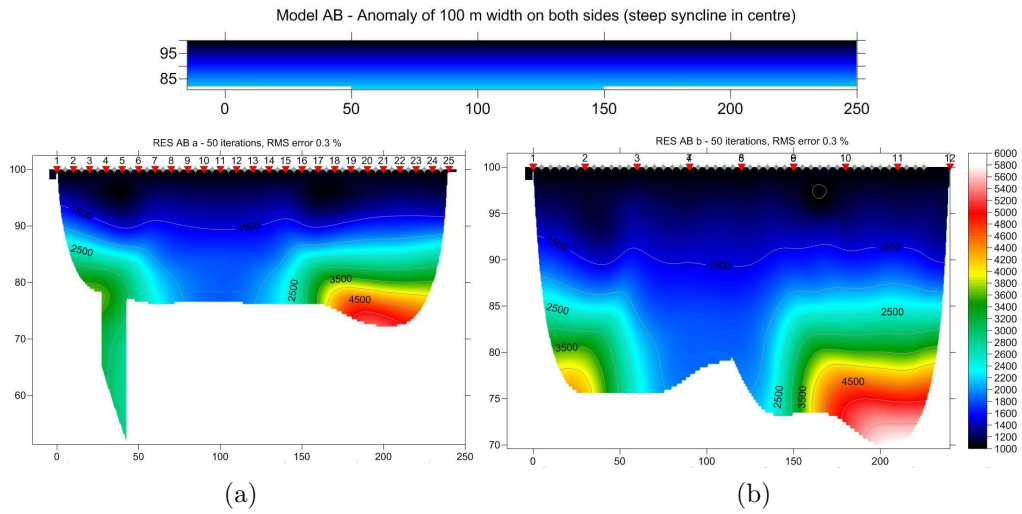


Figure C.21: Model AB: The anomaly with a velocity of 5000 m/s is located on the bottom left and right leaving an opening of 100 m . Resulting contrast is 2.67 . Figure (a): high density data with 48 geophones and 25 shots. Figure (b): low density with 2×24 geophones and 2×6 shots. Both cases recognize this set-up and model the anomaly at the right altitude and opening. The green area in the lower left of figure (a) probably caused by the wavepath envelope algorithm, which might fail, or low wavepath coverage.

C.1.1 Synthetic models with faults

In the following, the results from investigations of models with faults are illustrated. Faults with an opening of 10 m and sloping angles of 15 and 75 degrees have been modelled as well as with 15 degrees slope and an opening of 38 m . All models have a weathering layer of 5 m thickness and refractors with constant velocity as well as gradients are used. Different initial models are considered, too.

Additionally, first arrivals traveltimes are compared. Traveltimes differences of models with faults of 90 , 75 , 15 degrees and a plane refractor (0 degree) are generated and compared to each other by subtracting them from each other.

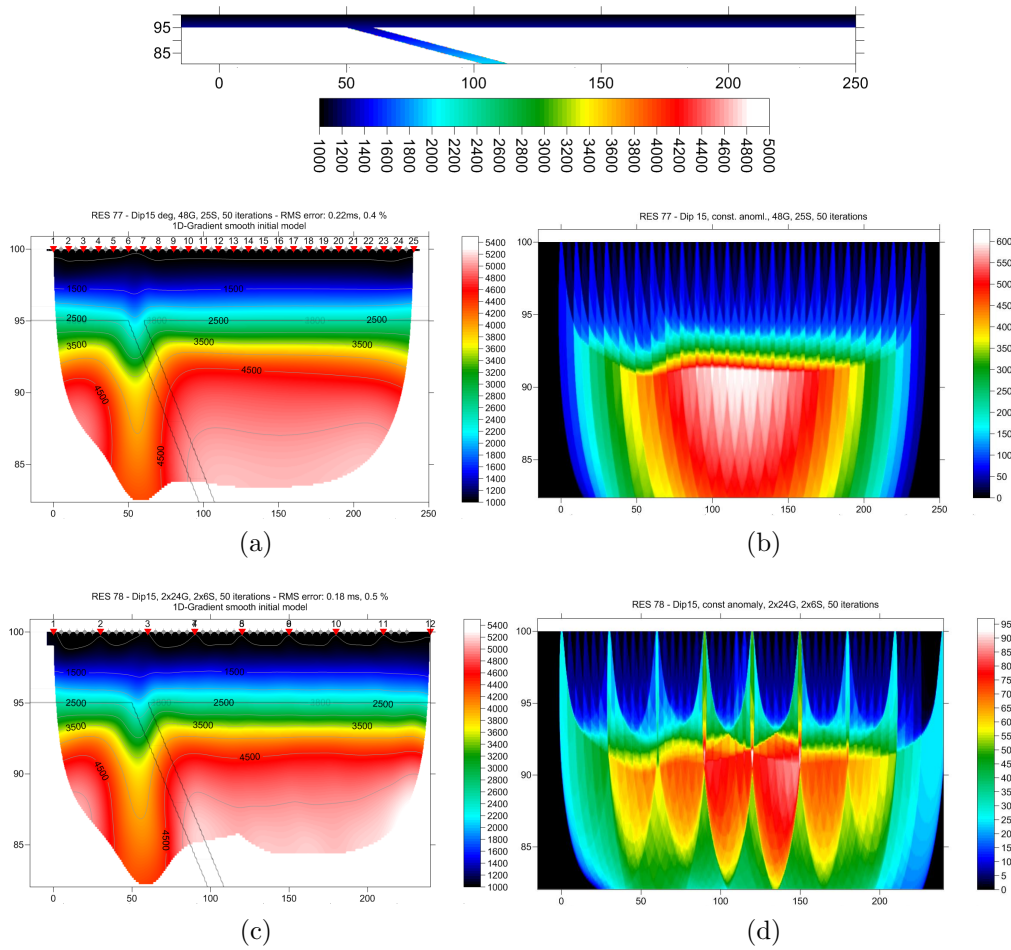
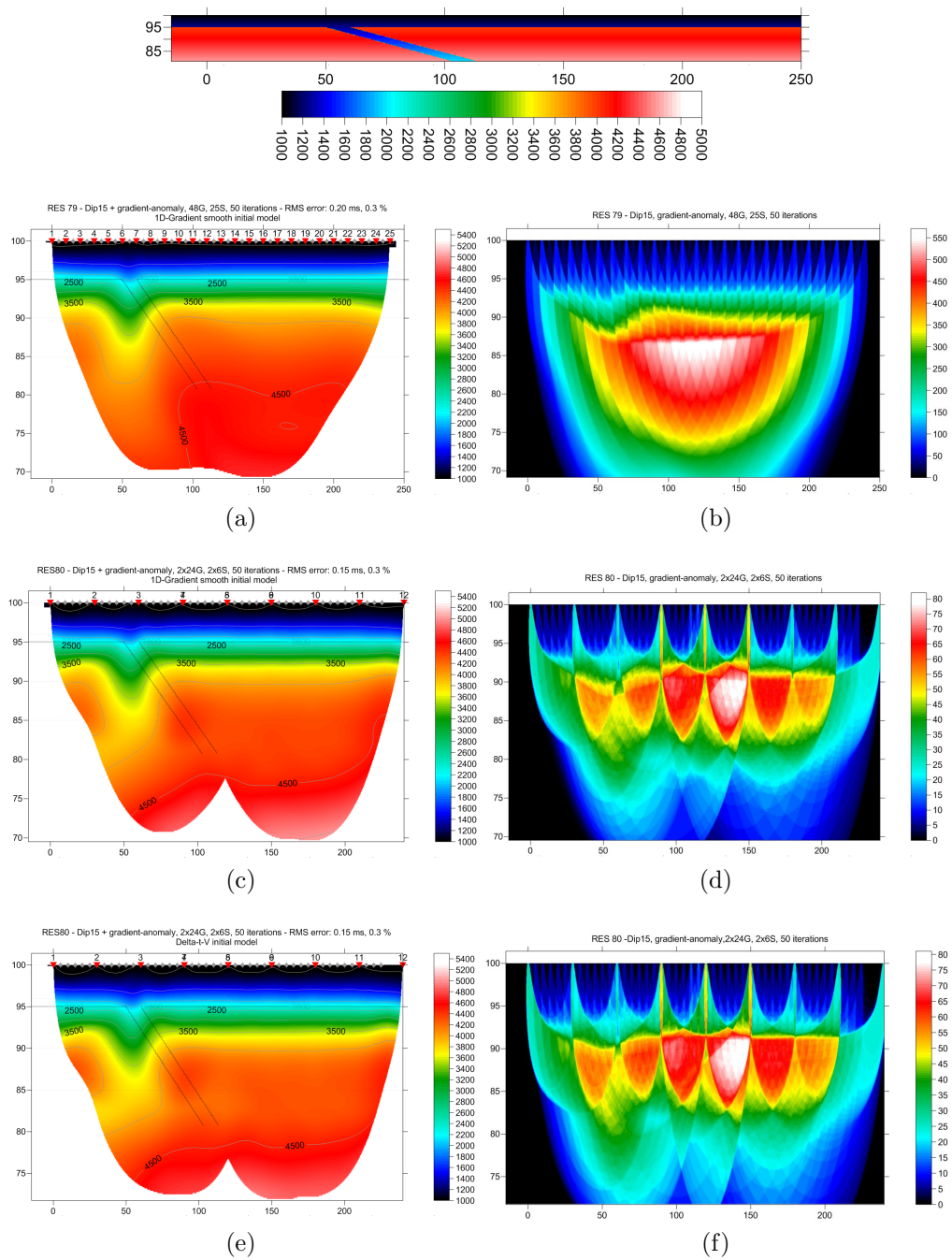


Figure C.22: Model: Weathering layer with velocity gradient and 5 m thickness, constant refractor velocity (5000 m/s). Rift with 10 m opening at top of refractor and 15 degrees dipping angle. (a): tomogram from high density data with 48 geophones and 25 shots. (b): wavepath coverage for (a) in paths/pixel.(c): tomogram from low density with 2×24 geophones and 2×6 shots. (d): wavepath coverage for (c) in paths/pixels. Both cases model the opening but not the slope.



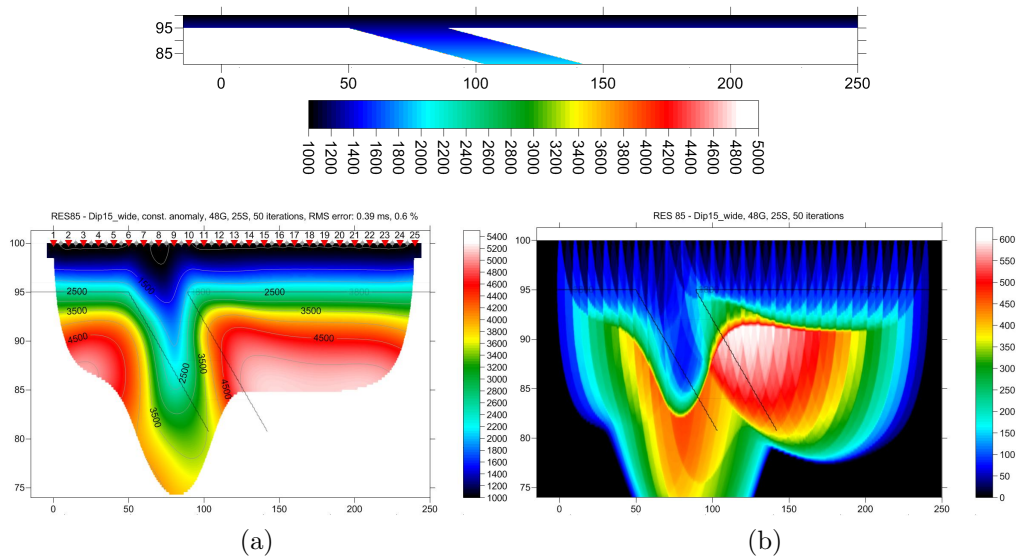


Figure C.24: Model: Weathering layer of 5 m thickness with constant refractor velocity of 5000 m/s. Rift with 38 m opening at top of refractor and 15 degrees dipping angle. (a): tomogram from high density data with 48 geophones and 25 shots. (b): wavepath coverage for (a) in paths/pixel. The opening is well modelled and a slope is recognized as well but with a steeper angle.

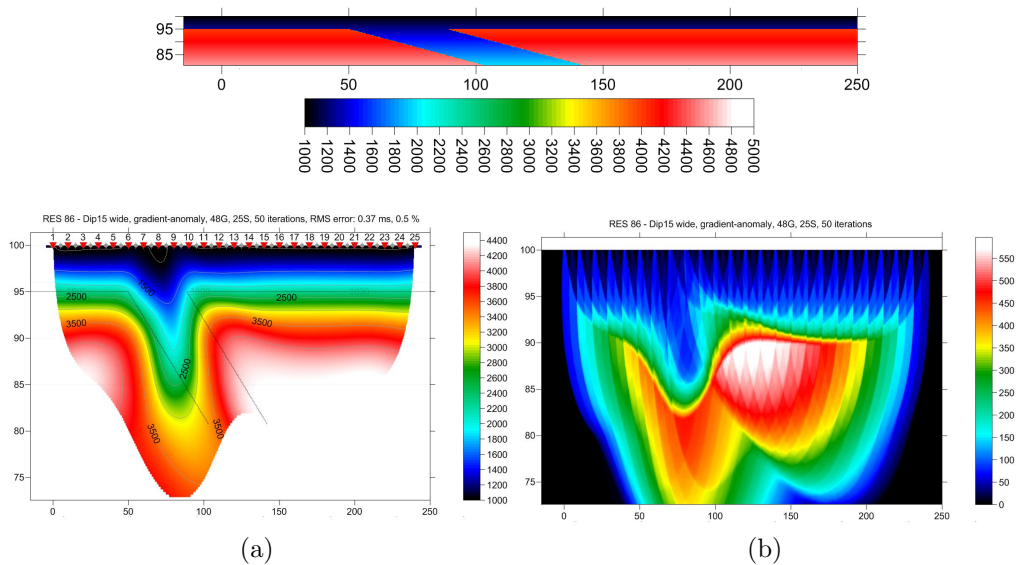


Figure C.25: Model: Weathering layer of 5 m thickness and gradient refractor velocity with 4000 m/s at top and 40 m/s/m increase. Rift with 38 m opening at top of refractor and 15 degrees dipping angle. (a): tomogram from high density data with 48 geophones and 25 shots. (b): wavepath coverage for (a) in paths/pixel. The opening is well modelled and a slope is recognized as well but with a larger angle.

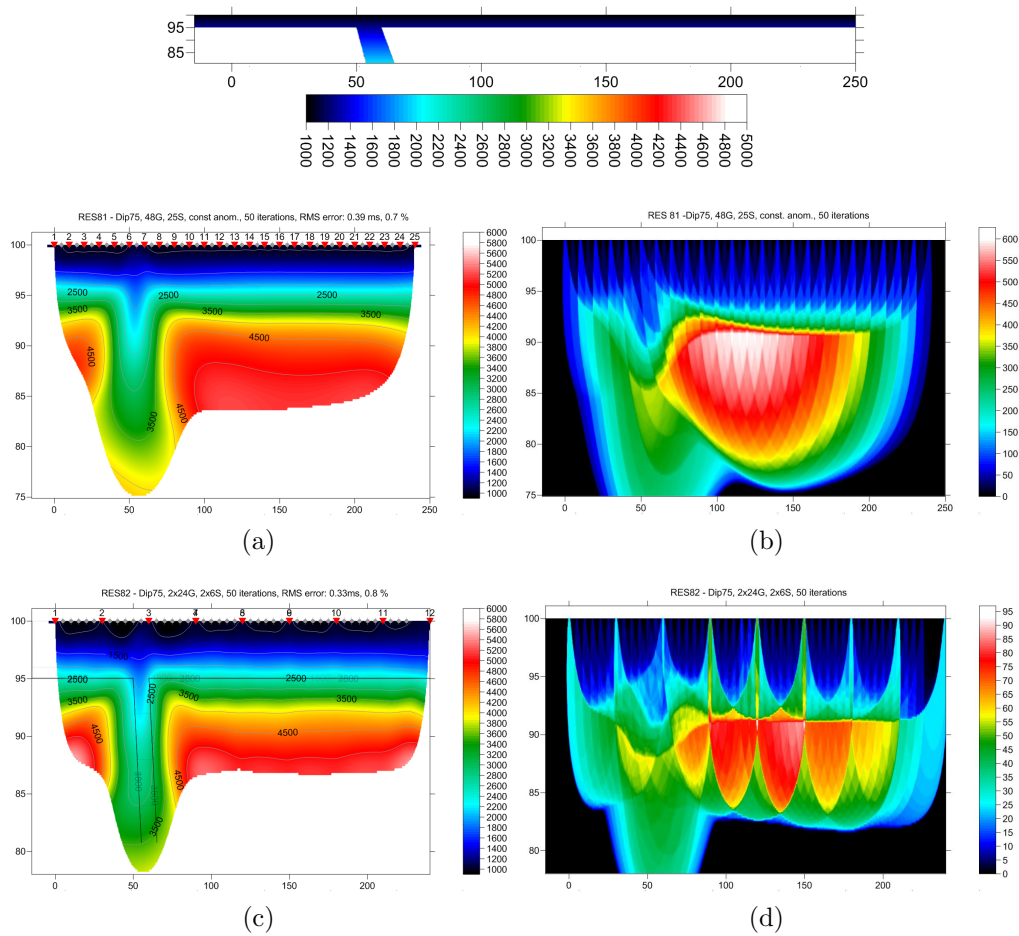


Figure C.26: Model: Weathering layer of 5 m thickness and constant refractor velocity (5000 m/s). Rift with 10 m opening at top of refractor and 75 degrees dipping angle. (a): tomogram from high density data with 48 geophones and 25 shots. (b): wavepath coverage for (a) in paths/pixel. (c): tomogram from low density with 2 x 24 geophones and 2 x 6 shots. (d): wavepath coverage for (c) in paths/pixels. Both cases model the opening, the slope can not really be seen in (a) but (c) shows a tendency.

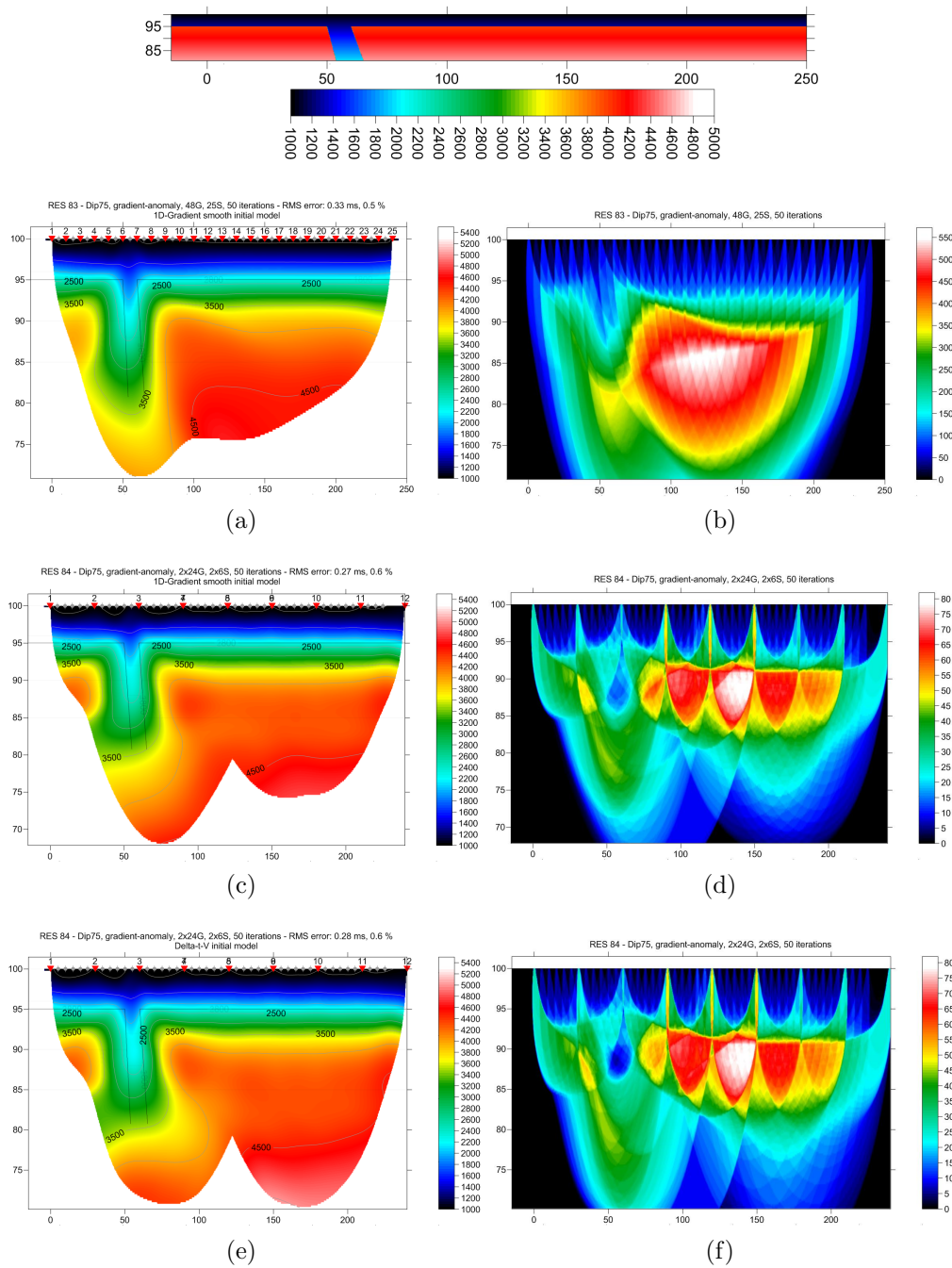


Figure C.27: Model: Weathering layer of 5 m thickness with gradient refractor velocity and 4000 m/s at top and 40 m/s/m increase. Rift with 10 m opening at top of refractor and 75 degrees dipping angle. (a): tomogram from high density data with 48 geophones and 25 shots. (b): wavepath coverage for (a) in paths/pixel. (c): tomogram from low density with 2 × 24 geophones and 2 × 6 shots. (d): wavepath coverage for (c) in paths/pixels. (e): as (c) with Delta-t-V initial model. (f): wavepath coverage for (e) in paths/pixel. Case (a) models the opening but not the slope, cases (c) and (e) reveal some tendency of an angle. Difference between (c) and (e) is the initial model which is generated with Delta-t-V inversion in case (e).

Comparison of First Arrival Traveltimes

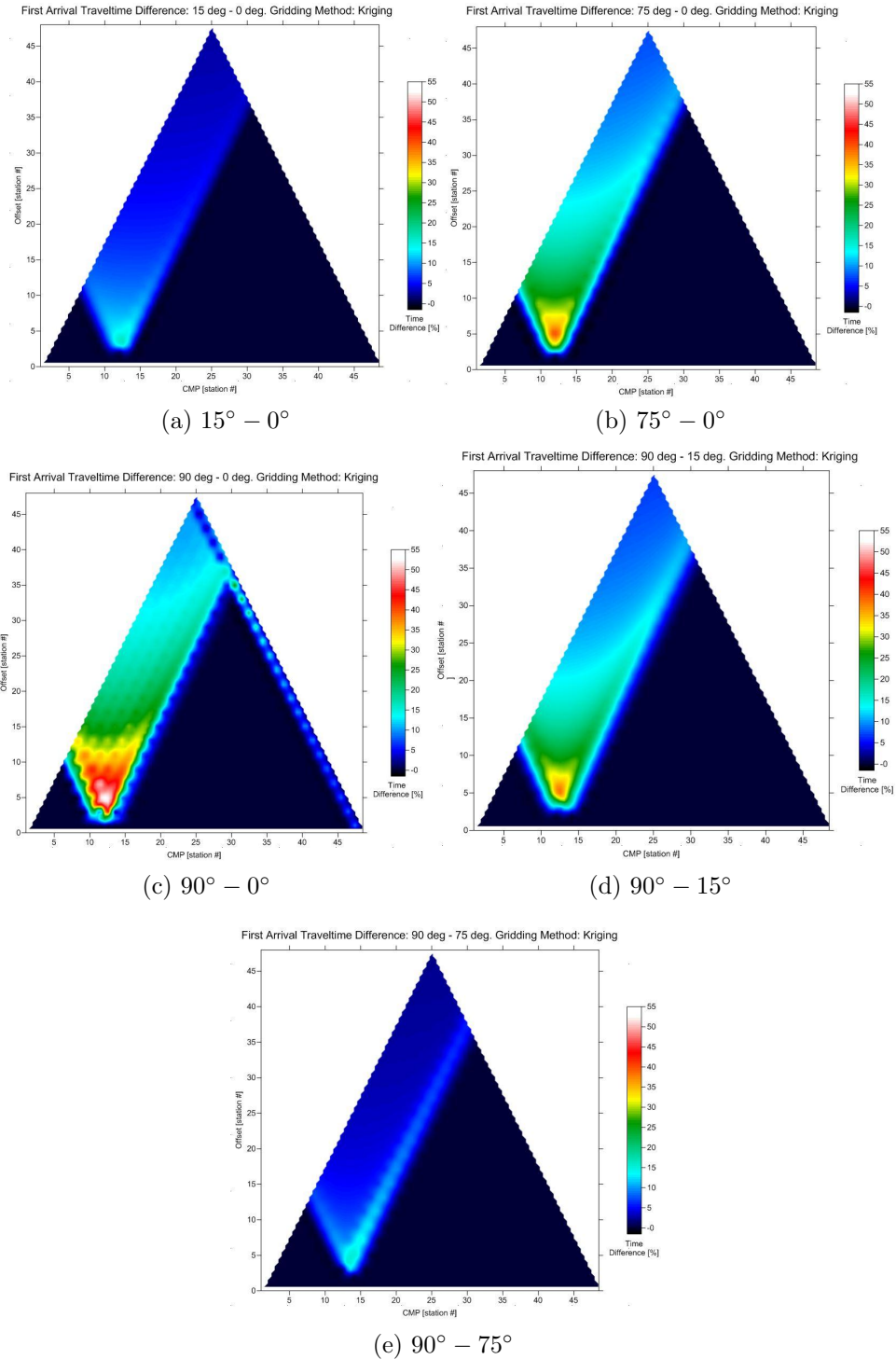


Figure C.28: Comparison of First Arrival Traveltimes for a plane refractor (0 degree) and dipping angles of 15, 75 and 90 degrees. Area not covered by the first arrival time is blanked. An increase of difference can be observed from (a) to (b) to (c) and a decrease from (c) to (d) to (e). Figures (a), (b), (c) and (d) show very symmetric differences, which is synonymous for that different angles are modelled as the same angles. Figure (e) shows some asymmetry, which means, that the different angles can be recognized by the traveltimes.

Appendix D

Results of the Parameter Investigation

D.1 Tomogram of the Reference Model

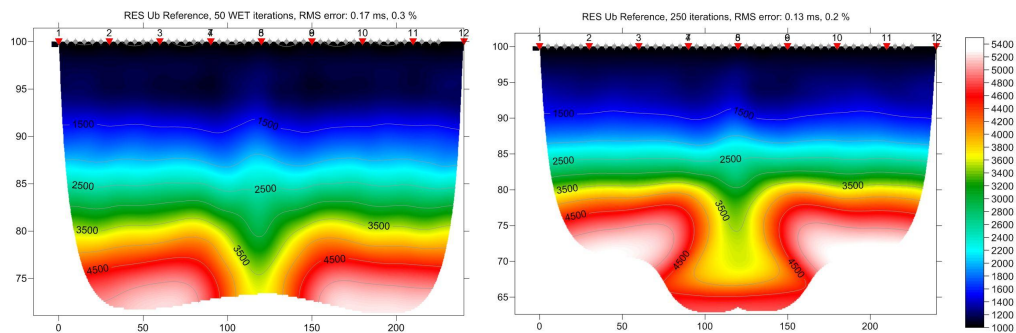


Figure D.1: Tomogram for Model Ub which serves as reference for Parameter Investigations. Default settings have been applied. Left shows the result after 50 iterations and right after 250 iterations.

D.2 Smooth Inversion

D.2.1 Smooth Inversion Settings

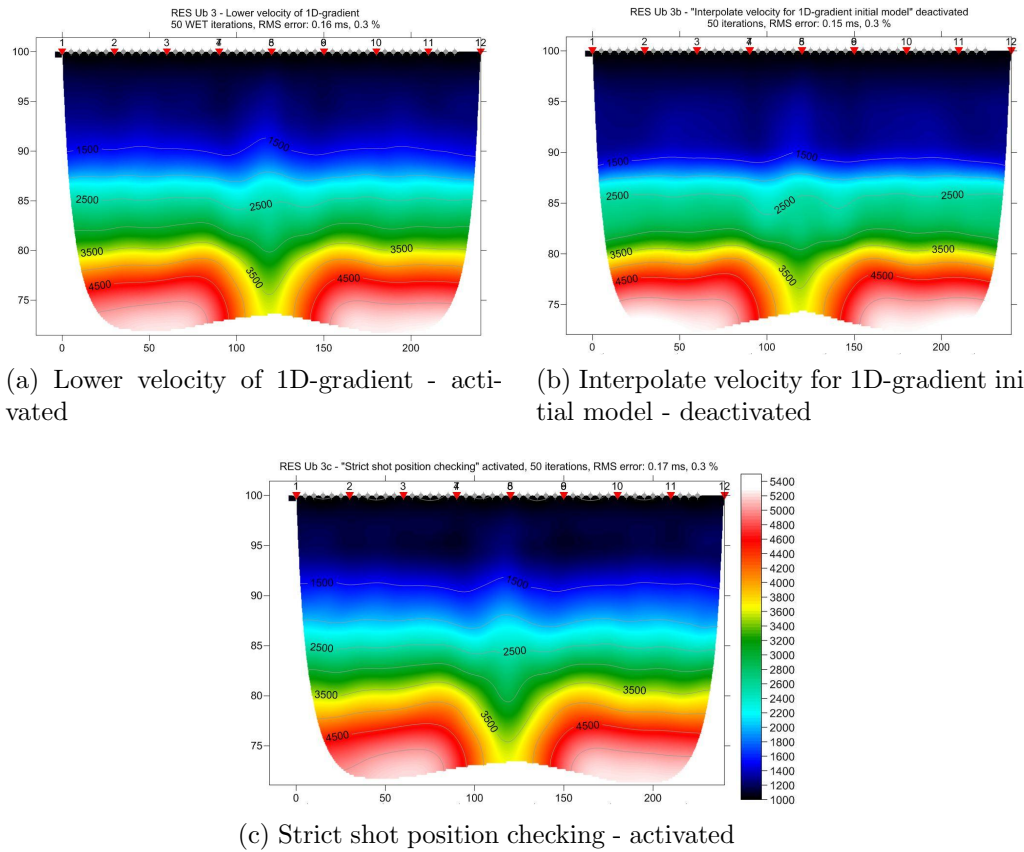
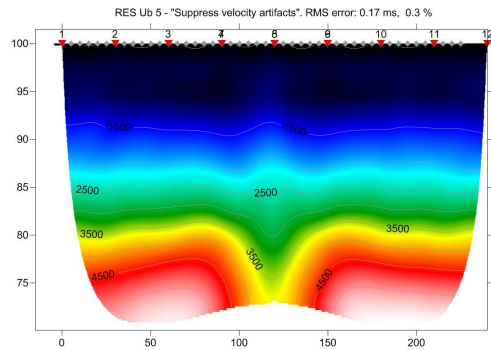
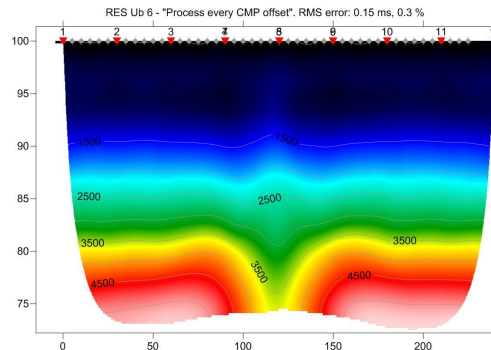


Figure D.2: Tomograms for respective settings within Smooth Inversion. Compared to default settings better RMS-errors are obtained with the settings in (a) and (b). The scale next to figure (c) is valid for all three tomograms.

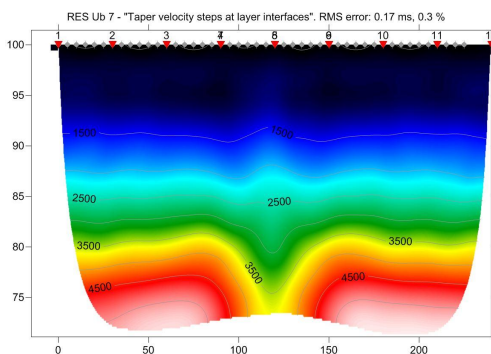
D.2.2 Delta-t-V Inversion Settings



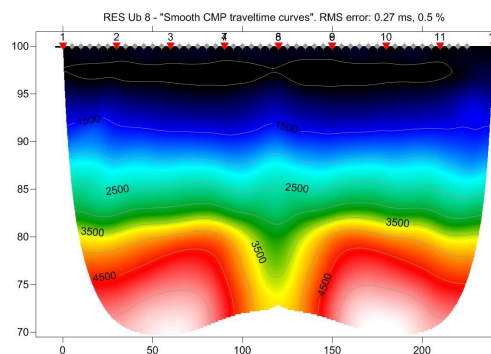
(a) Suppress velocity artefacts - activated



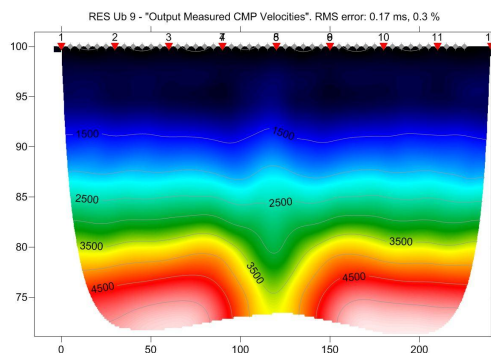
(b) Process every CMP offset - activated



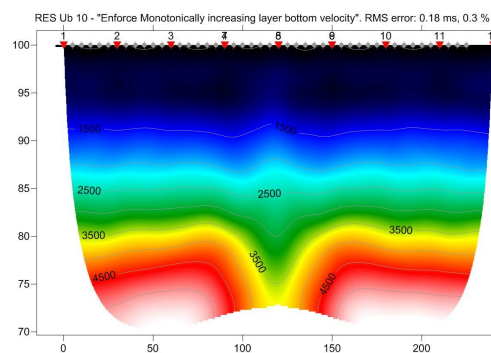
(c) Taper velocity steps at layer interfaces - activated



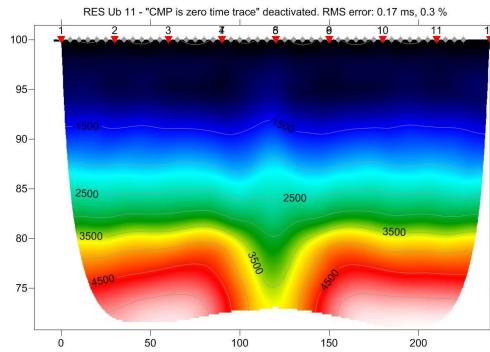
(d) Smooth CMP traveltimes curves - activated



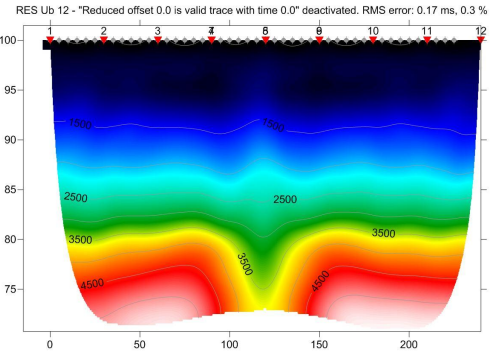
(e) Output Measured CMP velocities - activated



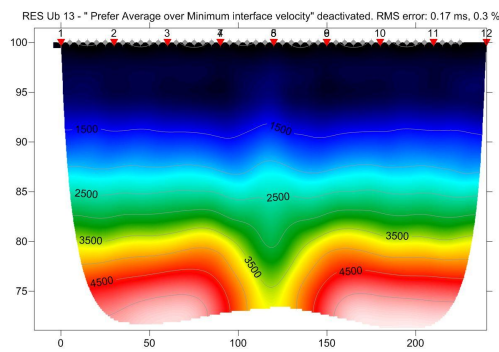
(f) Enforce Monotonically increasing layer bottom velocity - activated



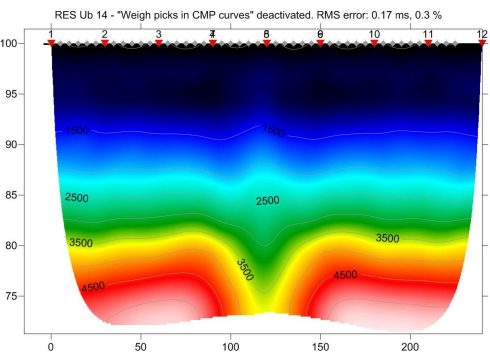
(g) CMP is zero time trace - deactivated



(h) Reduced offset 0.0 is valid trace with time 0.0 - deactivated



(i) Prefer Average over Minimum interface velocity - deactivated



(j) Weigh picks in CMP curves - deactivated

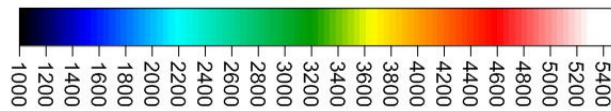


Figure D.3: WET inversion results after 50 iterations with respective Delta-t-V settings as stated beneath each tomogram. Initial model created with Smooth Inversion.

D.2.3 Parameters for Interactive Delta-t-V Inversion

For all inversion results, the RMS-values as well as the tomograms, equal the reference model both after Smooth Inversion and WET tomo. In the table below an overview of all tested parameters and the absolute RMS-errors are stated.

Interactive Delta-t-V Parameter	value	RMS-error
CMP curve stack width	10	0.17 <i>ms</i>
CMP curve stack width	5 (default is 15)	0.17 <i>ms</i>
Linear regression method: least squares		
Regression over offset stations	10	0.17 <i>ms</i>
Linear regression method: least deviations		
Regression over offset stations	10	0.17 <i>ms</i>
No static corrections	weathering crossover = 10	0.17 <i>ms</i>
No static corrections	weathering crossover = 8	0.17 <i>ms</i>
No static corrections	weathering crossover = 6	0.17 <i>ms</i>
No static corrections	weathering crossover = 3 ¹	0.17 <i>ms</i>
Surface consistent corrections	Topography filter = 100	0.17 <i>ms</i>
Surface consistent corrections	Topography filter = 50	0.17 <i>ms</i>
Surface consistent corrections	Topography filter = 25	0.17 <i>ms</i>
CMP gather datum	weathering crossover = 3	0.17 <i>ms</i>
CMP gather datum	weathering crossover = 6	0.17 <i>ms</i>
CMP gather datum	weathering crossover = 8	0.17 <i>ms</i>
CMP gather datum	weathering crossover = 14	0.17 <i>ms</i>
Trace weighting in CMP stack	1 ²	0.17 <i>ms</i>
Trace weighting in CMP stack	0.1	0.17 <i>ms</i>
Trace weighting in CMP stack	0.01 ¹	0.17 <i>ms</i>
Gridding method	Delaunay triangulation	0.17 <i>ms</i>
Gridding method	Minimum curvature	0.17 <i>ms</i>
Gridding method	Natural Neighbor	0.17 <i>ms</i>
Gridding method	Nearest Neighbor	0.17 <i>ms</i>

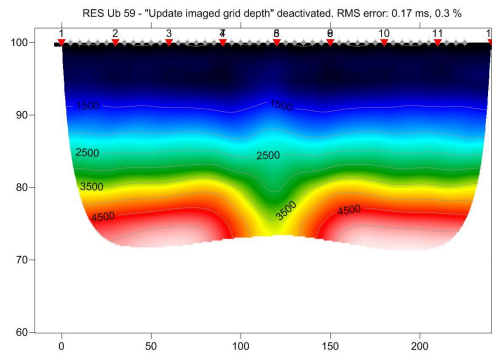
Table D.1: WET Tomography results after 50 iterations with different Interactive Delta-t-V parameters applied. The Interactive Delta-t-V inversion has not been run. All results equal the default result.

¹This is the minimum value.

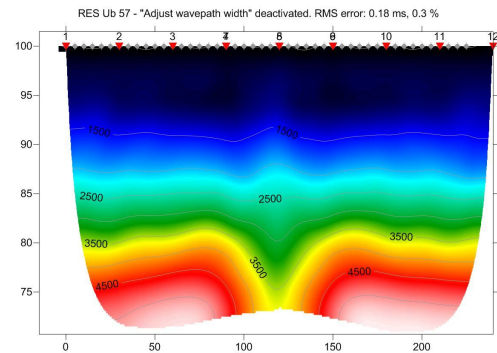
²This is the maximum value.

D.3 WET Tomography

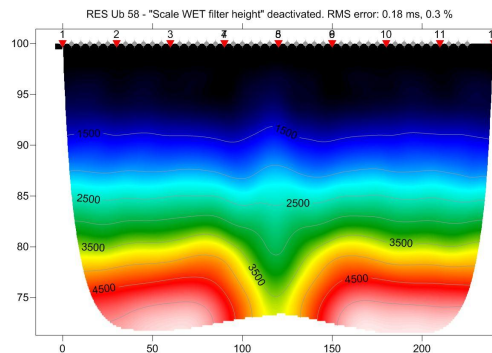
D.3.1 WET Tomography Settings



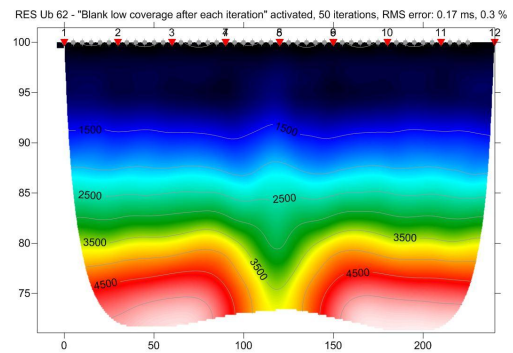
(a) Update imaged grid depth - deactivated



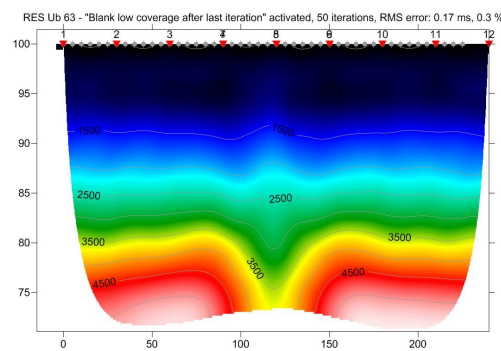
(b) Adjust wavepath width - deactivated



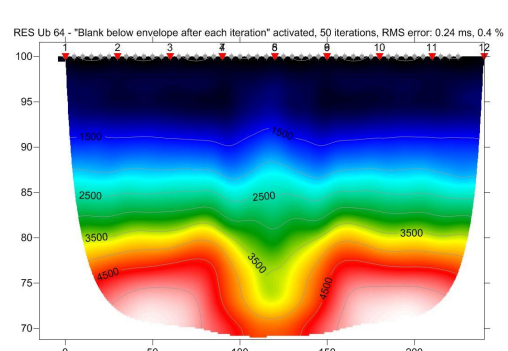
(c) Scale WET filter height - deactivated



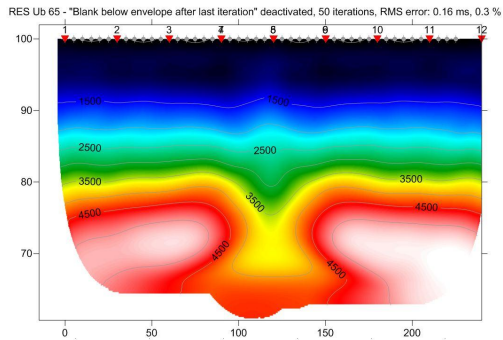
(d) Blank low coverage after each iteration - activated



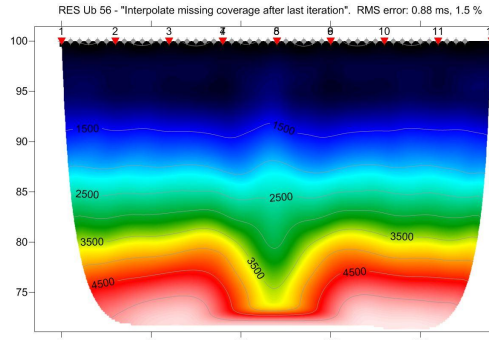
(e) Blank low coverage after last iteration - activated



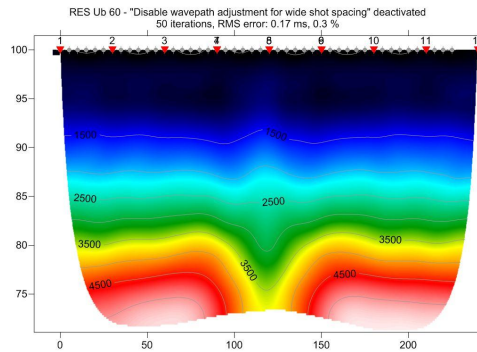
(f) Blank below envelope after each iteration - activated



(g) Blank below envelope after last iteration - deactivated



(h) Interpolate missing coverage after last iteration - activated



(i) Disable wavepath width adjustment for wide shot spacing - deactivated

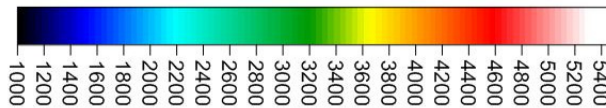


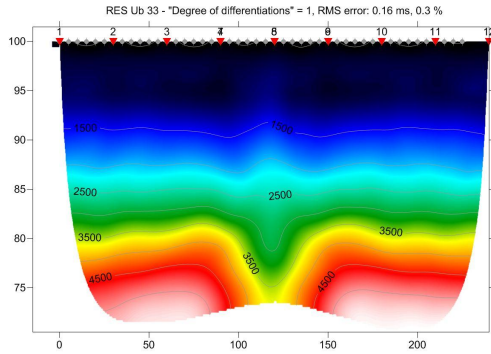
Figure D.4: Tomograms from WET inversions with different WET Tomo settings activated/deactivated. The best result is shown in figure (g) and the worst in figure (h).

D.3.2 Settings for Forward modelling

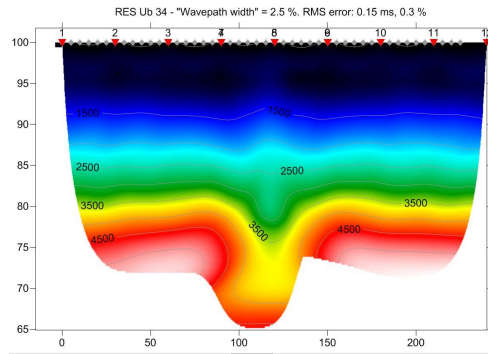
For the settings listed below all inversion results are equal to the reference model (RMS-error: 0.17 *ms*/0.3 %). The following settings have been applied:

- Correct all velocities for Delta-t-V systematic error
- Correct basement velocities for Delta-t-V systematic errors
- Skip every 2nd shot for forward modelling
- Allow gaps in coverage of velocity model grid columns

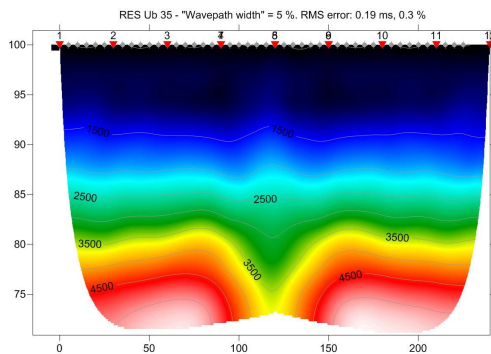
D.3.3 Interactive WET Tomomography Parameters



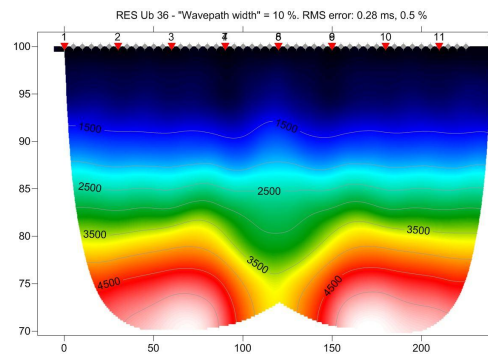
(a) Degree of differentiations: 1



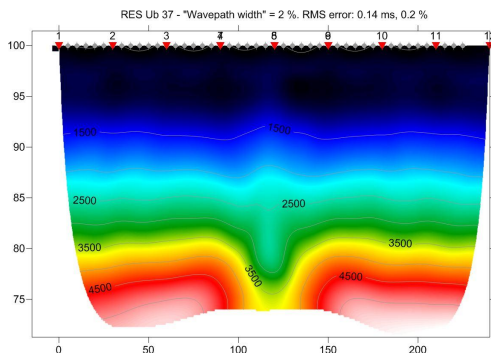
(b) Wavepath width: 2.5 %



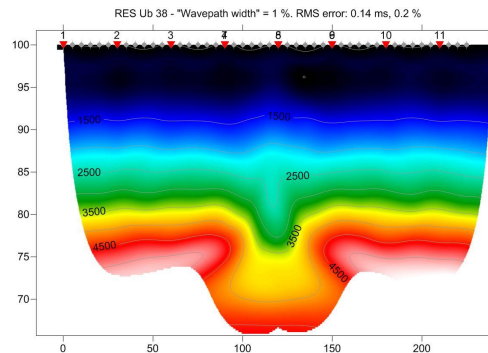
(c) Wavepath width: 5 %



(d) Wavepath width: 10 %



(e) Wavepath width: 2 %



(f) Wavepath width: 1 %

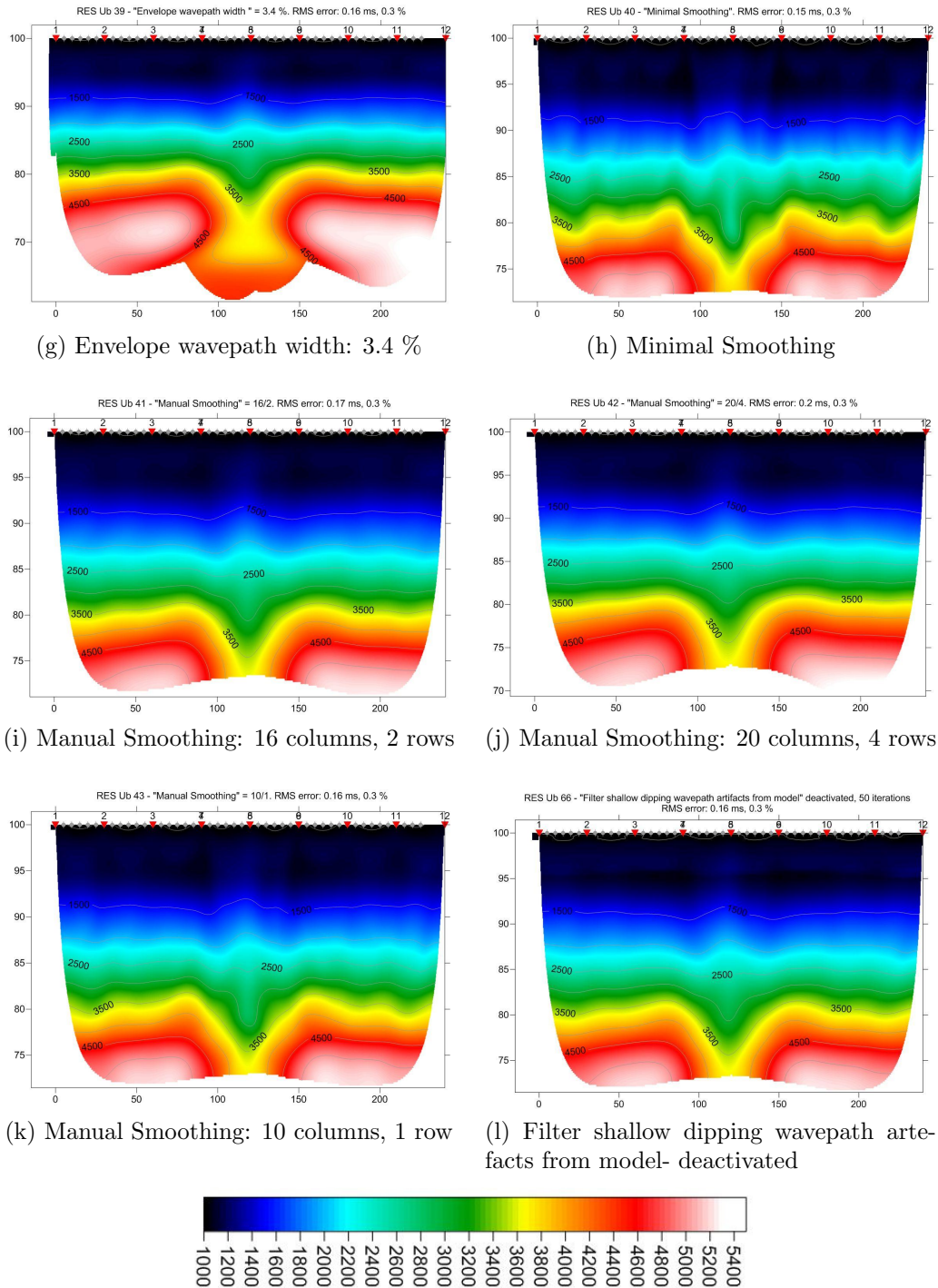


Figure D.5: Tomograms for Interactive WET Tomography parameter investigation after 50 iterations. Respective parameters are stated below each figure; the scale in the bottom is valid for all tomograms.

D.4 Combinations of Settings and Parameters

In table D.2 the settings and parameters yielding a better absolute RMS error than default settings are applied in different combinations. For each combination 50 and 250 iterations were run. The letters in the very right column state the respective sub-figure in figures D.6 and D.7.

Parameter/Setting	value/option	RMS-error		Fig.
		50 it.	250 it.	
PARRES 1				
Lower velocity of 1D-gradient layer	activated	0.13 ms	0.08 ms	a
Process every CMP offset	activated			
Wavepath width	2 %			
Smoothing	Minimal			
PARRES 2				
Lower velocity of 1D-gradient layer	activated	0.15 ms	0.09 ms	b
Process every CMP offset	activated			
Wavepath width	3.5 %			
Smoothing	Minimal			
PARRES 3				
Lower velocity of 1D-gradient layer	activated	0.13 ms	0.08 ms	c
Process every CMP offset	activated			
Interpolate velocity for 1D-gradient initial model	de-activated			
Wavepath width	2 %			
Smoothing	Minimal			
PARRES 4				
Lower velocity of 1D-gradient layer	activated	0.12 ms	0.06 ms	d
Process every CMP offset	activated			
Blank below envelope after last iteration	de-activated			
Wavepath width	2 %			
Smoothing	Minimal			
PARRES 6				
Lower velocity of 1D-gradient layer	activated	0.12 ms	0.06 ms	e
Process every CMP offset	activated			
Blank below envelope after last iteration	de-activated			
Filter shallow dipping wavepath artefacts from model	un-checked			
Wavepath width	2 %			
Smoothing	Minimal			
PARRES 7				
Lower velocity of 1D-gradient layer	activated	0.13 ms	0.07 ms	f
Process every CMP offset	activated			
Filter shallow dipping wavepath artefacts from model	un-checked			
Wavepath width	2 %			
Smoothing	Minimal			

Table D.2: Combinations of options and parameters yielding better RMS-error than the default settings. Each combination was run with 50 and 250 iterations. The column on the right states the respective sub-figure in figures D.6 and D.7.

D.4.1 Tomograms after 50 iterations

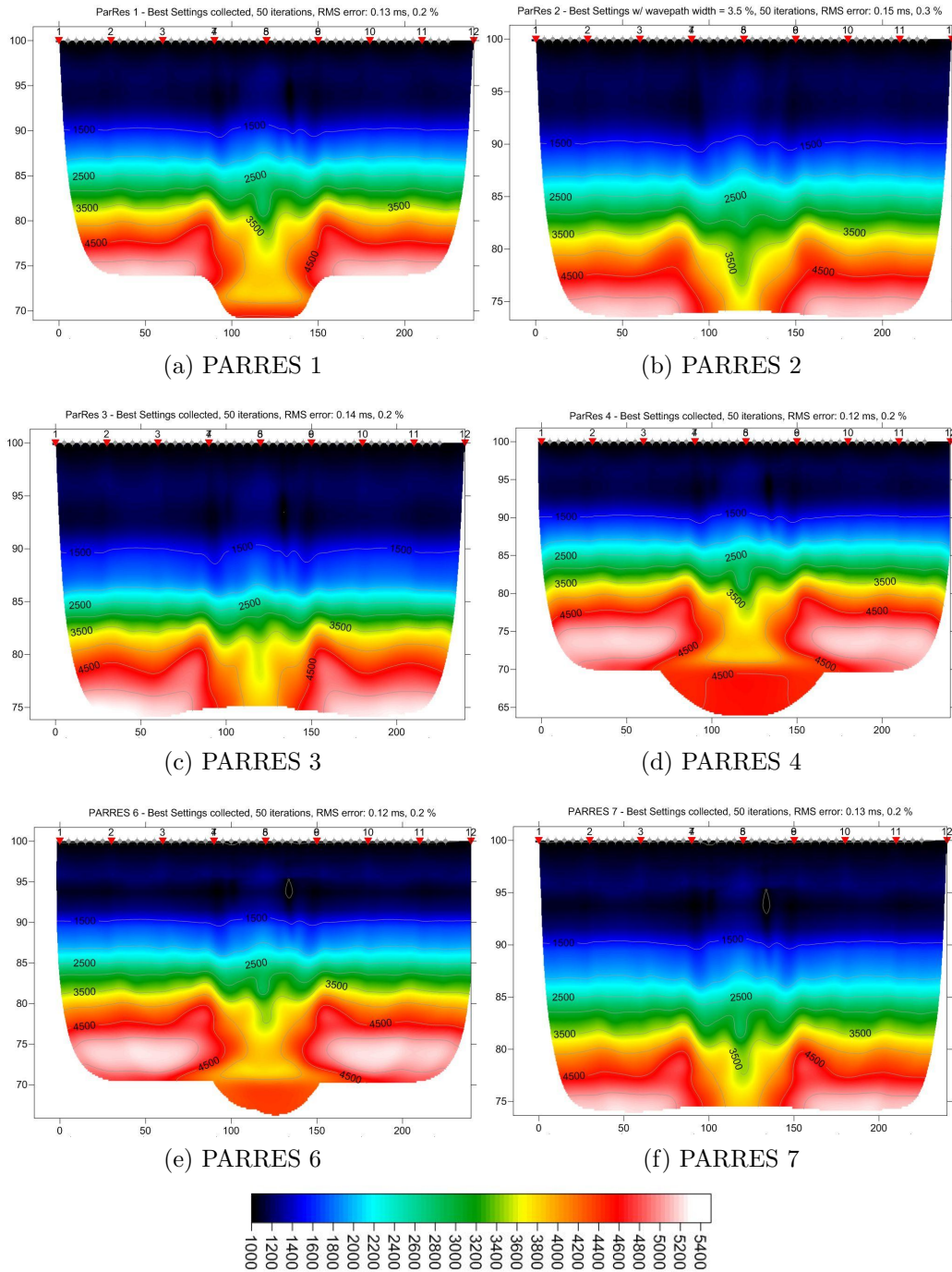


Figure D.6: Tomograms for parameter- and setting-combination as stated beneath each image. The respective combinations are stated in D.2. All inversions have been run with 50 iterations.

D.4.2 Tomograms after 250 iterations

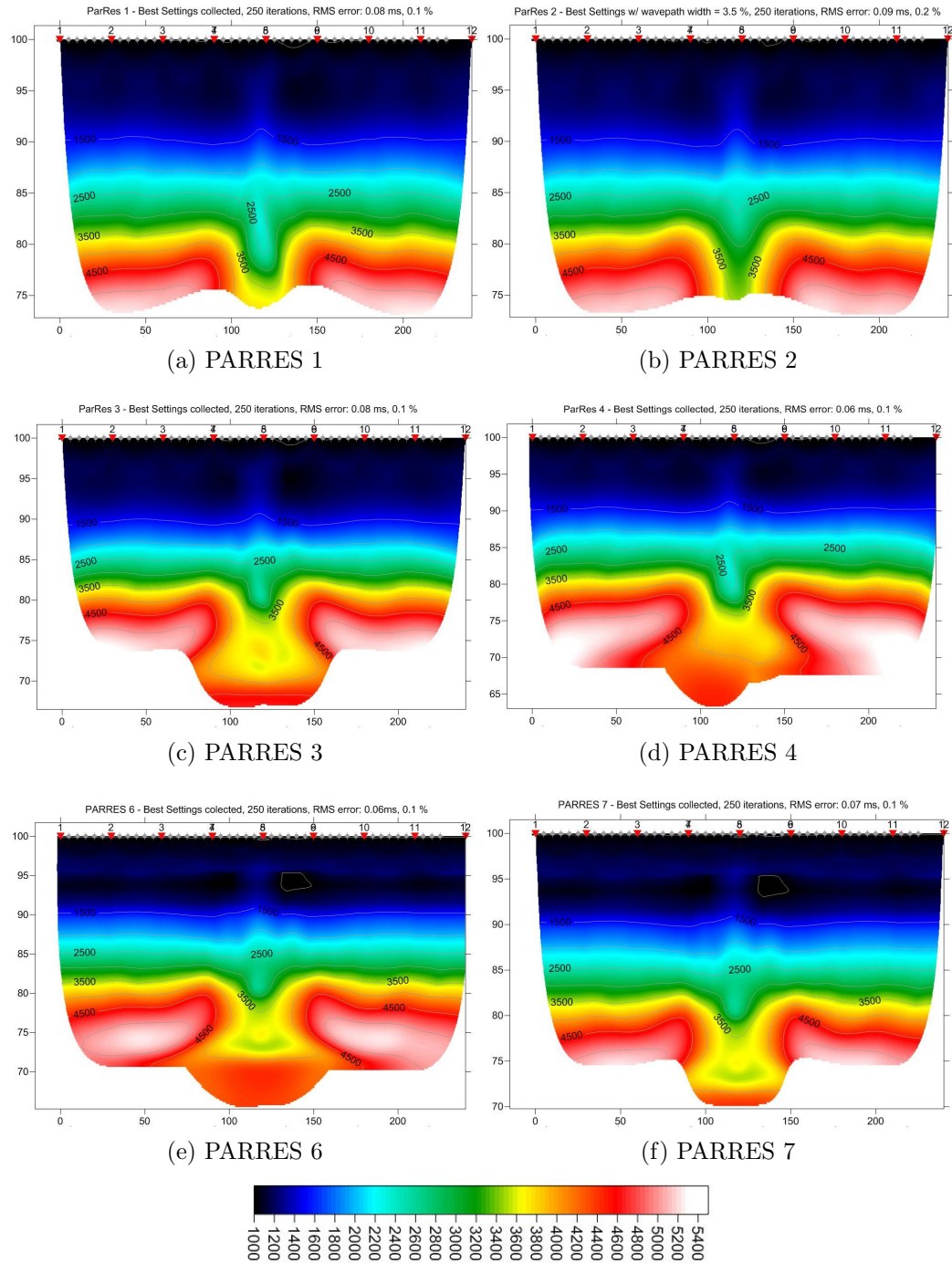


Figure D.7: Tomograms for parameter- and setting-combination as stated beneath each image. The respective combinations are stated in D.2. All inversions have been run with 250 iterations.

Appendix E

Case Ørbekk - Inversion Results

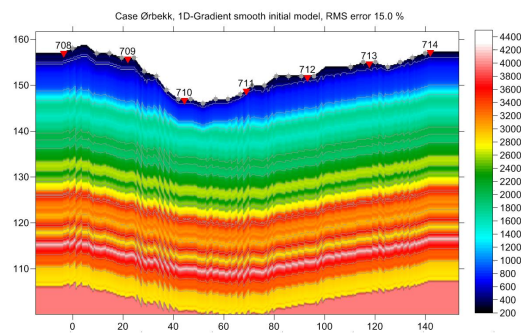
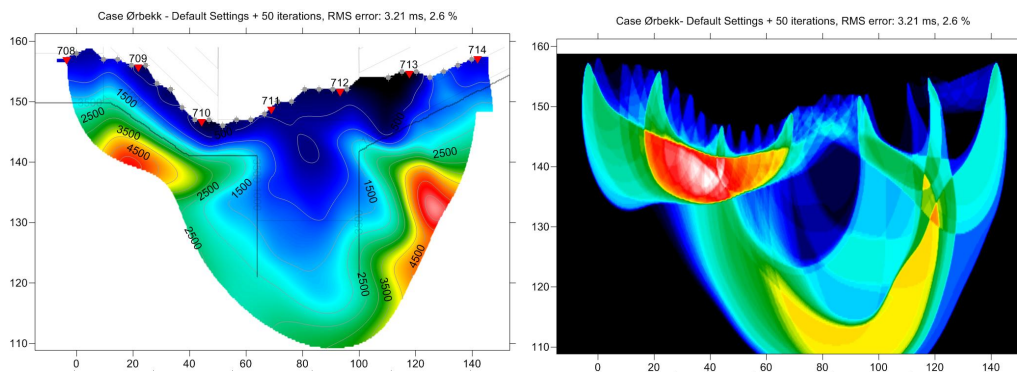
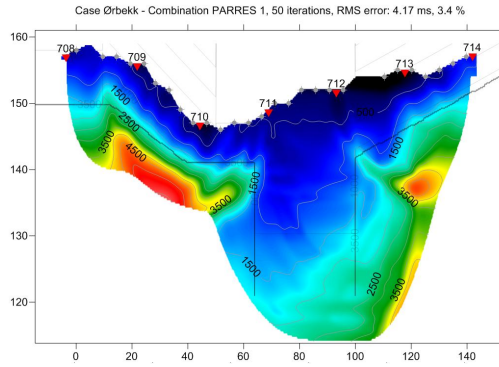


Figure E.1: Initial model for the inversions of the Ørbekk case. The default settings have been applied.

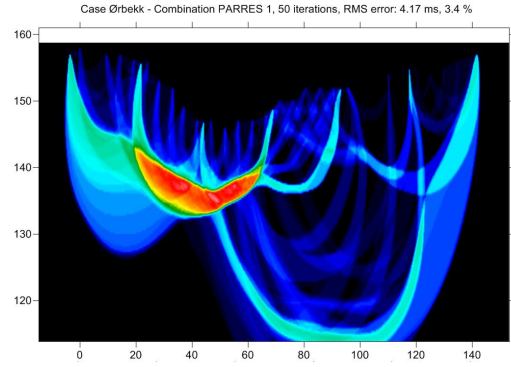


(a) Default Parameters

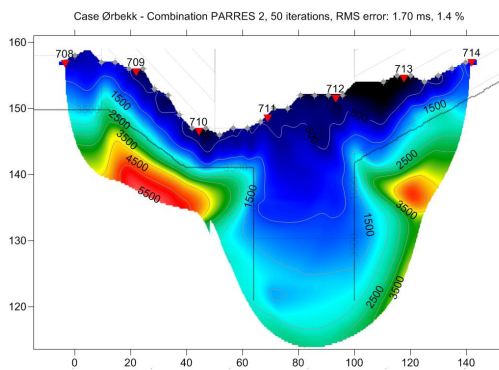
(b) Wavepath coverage for a



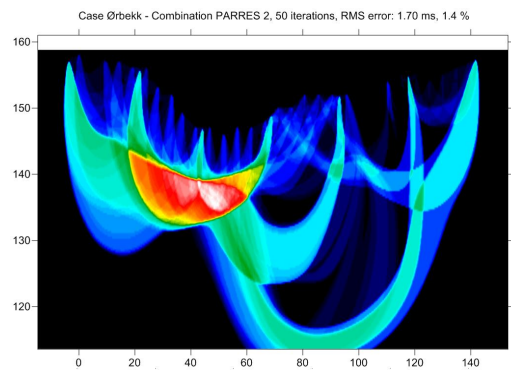
(c) PARRES 1



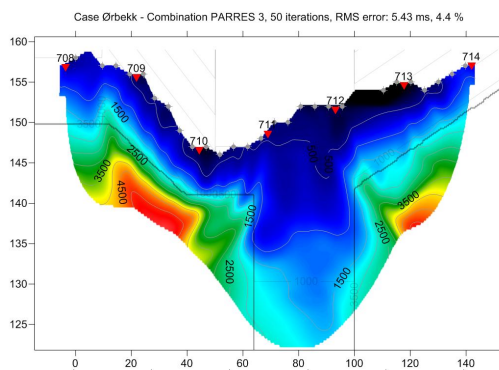
(d) Wavepath coverage for c



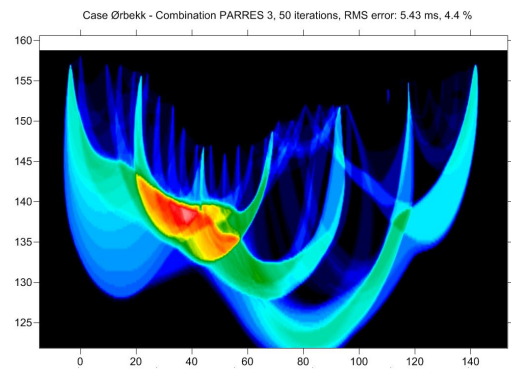
(e) PARRES 2



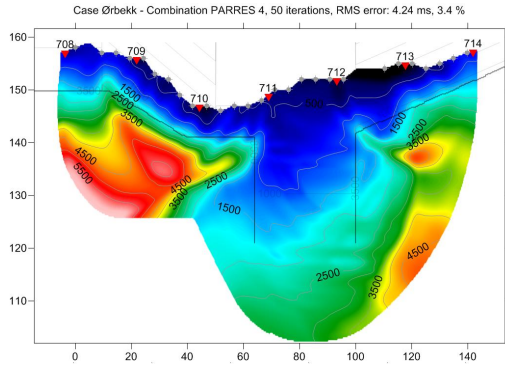
(f) Wavepath coverage for e



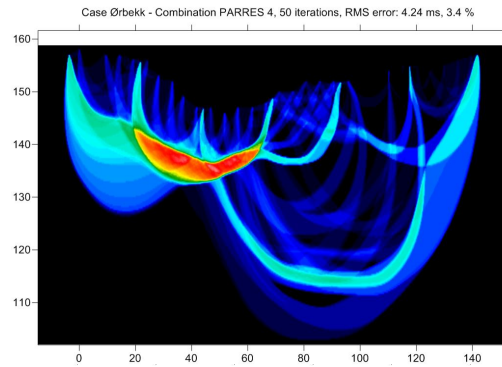
(g) PARRES 3



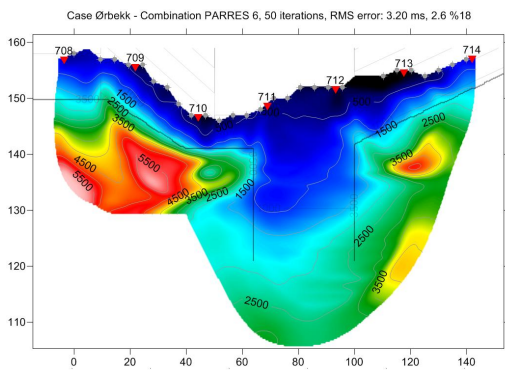
(h) Wavepath coverage for g



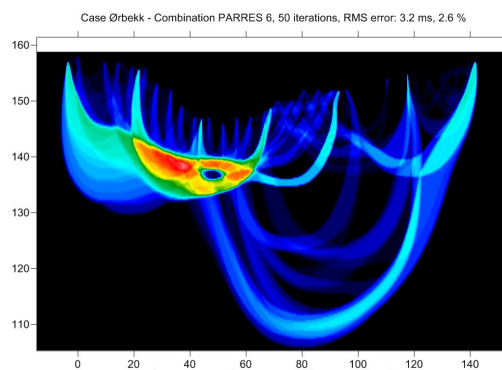
(i) PARRES 4



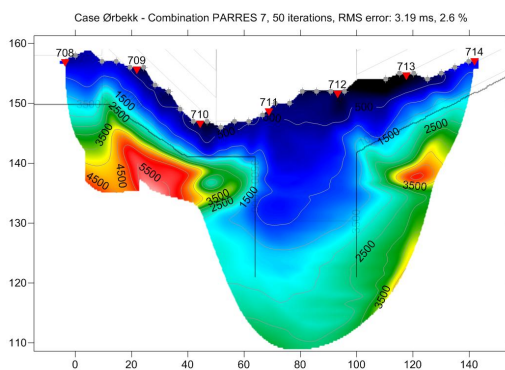
(j) Wavepath coverage for i



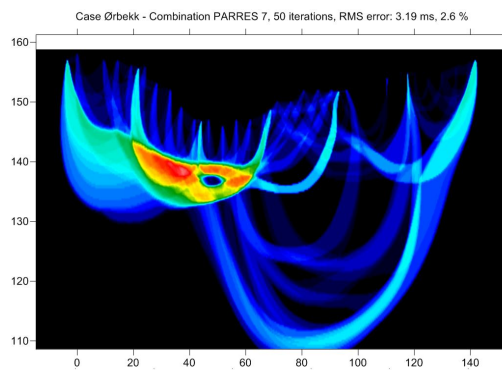
(k) PARRES 6



(l) Wavepath coverage for k



(m) PARRES 7



(n) Wavepath coverage for m

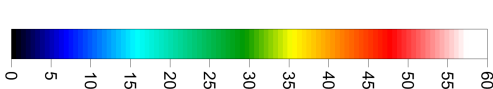
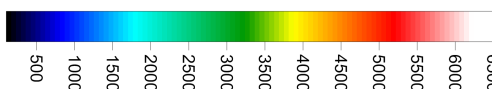


Figure E.2: Case Ørbekk: Tomograms and wavepath-coverages for inversions applying the parameter combinations as stated in table D.2.

Appendix F

Additional Analysis

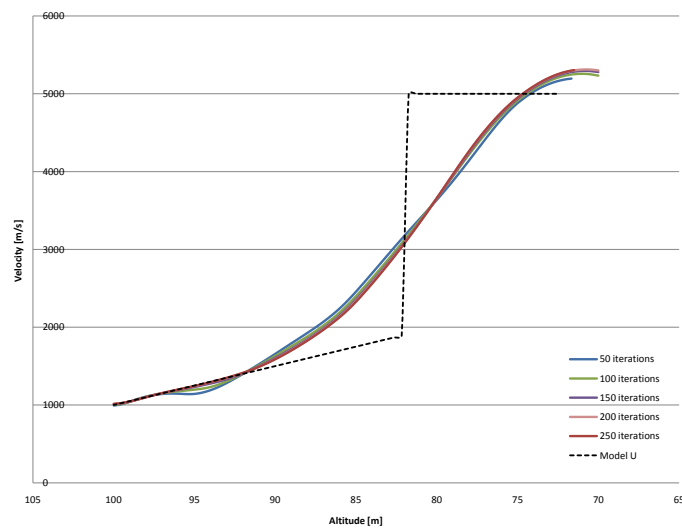


Figure F.1: This diagram shows the development of the velocity contrast at a vertical cut around 50 m offset. The velocities are averaged between 45 and 55 m. Curves for 50, 100, 150, 200 and 250 iterations are shown.

Appendix G

Further Improvements

Model Ub: same result as for PARRES 4 and PARRES 6 for

- 1D-Gradient smooth initial model with default settings
- Wavepath width: 2 %, Minimal Smoothing, Blank below envelope after last iteration and Filter shallow dipping wavepath artefacts from model deactivated

Ørbekk synthetic model: RMS-error 1.70 *ms* to 1.28 *ms* for

- 1D-Gradient smooth initial model with default settings
- Wavepath width: 6.5 % (default is 6 %) and Minimal Smoothing

Ørbekk field data: RMS-error 1.43 *ms* to 1.37 *ms* for

- 1D-Gradient smooth initial model with default settings
- Wavepath width 3.0 or 3.5 % and Minimal Smoothing

Bibliography

- Aldridge, D. F., Oldenburg, D. W., 1992. Refractor imaging using an automated wavefront reconstruction method. *Geophysics* 57, 378–385.
- Cervený, V., Soares, J., 1992. Fresnel volume ray tracing. *Geophysics* 57, 902–915.
- Drijkoningen, G. G., Verschuur, D. J., September 2003. Seismic data processing. Tech. rep., Centre for Technical Geoscience, Delft University of Technology.
- Gebrande, H., 1986. CMP-Refraktionsseismik. In: *Seismik auf neuen Wegen, Expanded abstract*. Lothar Dresen, Jürgen Fertig, Horst Rüter, Wolfgang Budach, pp. 191–205.
- Gebrande, H., Miller, H., 1985. Refraktionsseismik. In: *Angewandte Wissenschaften II*. Ferdinand Enke Verlag, Stuttgart, pp. 226–260.
- Hagedoorn, J. G., 1959. The Plus-Minus Method of Interpreting Seismic Refraction Sections. *Geophysical Prospecting* 7, 158–182.
- Husen, S., Kissling, E., 2001. Local earthquake tomography between rays and waves: fast ray tomography. *Physics of the earth and Planetary Interiors* 123, 129–149.
- Lay, T., Wallace, T. C., 1995. *Modern Global Seismology*. Vol. 58 of *International Geophysics Series*. Academic Press.
- Lecomte, I., Gjøystdal, H., Dahle, A., Pedersen, O. C., 2000. Improving modeling and inversion in refraction seismics with a first-order Eikonal solver. *Geophysical Prospecting* 48, 437–454.

- Olaya, J. C., Romero, R., 2009. Visualization of Inversion Uncertainty in Travel Time Seismic Tomography. Tech. rep., Department of Computer Science, University of Texas at El Paso.
- Palmer, D., 1980. The Generalized Reciprocal Method of Seismic Refraction Interpretation. Society of Exploration Geophysicists, Tulsa.
- Palmer, D., 1981. An introduction to the generalized reciprocal method of seismic refraction interpretation. *Geophysics* 46, 1508–1518.
- Palmer, D., 2009. Exploiting Lateral Resolution of Near-Surface Seismic Refraction Methods. *Journal of Earth Science* 20 (3), 526–545.
- Podvin, P., Lecomte, I., 1991. Finite difference computation of traveltimes in very contrasted velocity models: a massively parallel approach and its associated tools. *Geophysical Journal International* 105, 271–284.
- Qin, F., Luo, Y., Olsen, K., Cai, W., Schuster, G., 1992. Finite difference solution to the eikonal equation. *Geophysics* 57, 478–487.
- Quintus-Bosz, A., 1992. Wavapath eikonal equation traveltime inversion. Master's thesis, University of Utah.
- Rønning, J. S., Dalsegg, E., Heincke, B. H., Tønnesen, J. F., Wisén, R., December 2009. Resistivitetsmålinger og retolkning av seismikk langs E6 og Dovrebanen ved Mjøsa. Tech. rep., Norges geologiske undersøkelse.
- Rohdewald, S. R., 1999. Rayfract manual.
- Rohdewald, S. R., October 2010. E-mail correspondence with S. R. Rohdewald (Rayfract).
- Schuster, G. T., 1991. Wave-equation phase inversion in the frequency domain. 61st Ann. Internat. Mtg., Soc. Expl. Geophys. Expanded Abstract, 909–912.
- Schuster, G. T., Quintus-Bosz, A., 1993. Wavepath eikonal traveltime inversion: Theory. *Geophysics* 58, 1314–1323.
- Sheehan, J. R., Doll, W. E., Mandell, W. A., March 2005. An Evaluation of Methods and Available Software for Seismic Refraction Tomography. *Journal of Environmental and Engineering Geophysics* 10, 21–34.
- Spetzler, J., Snieder, R., May–June 2004. The Fresnel volume and transmitted waves. *Geophysics* 69, 653–663.

-
- Telford, W. M., Geldart, L. P., Sheriff, R. E., 2004. Applied Geophysics, 2nd Edition. Cambridge University Press.
- Vidale, J., 1988. Finite-difference calculation of traveltimes. BSSA 78, 2062–2076.
- Zhang, J., Toksoz, M. N., 1998. Nonlinear refraction travel time tomography. Geophysics 63, 1726–1737.

"Judgement is thus the intelligent use of experience or, more cautiously expressed, it is the recognition of one's limitations of the methods one uses, and of the limitations and uncertainties of the materials one works with; and this brings us back to geology."

Herbert H. Einstein, 1991